

August 2015

Theoretical Study of Magnetoelectric Effects in Noncentrosymmetric and Cuprate Superconductors

Manoj Kumar Kashyap
University of Wisconsin-Milwaukee

Follow this and additional works at: <https://dc.uwm.edu/etd>

 Part of the [Condensed Matter Physics Commons](#)

Recommended Citation

Kashyap, Manoj Kumar, "Theoretical Study of Magnetoelectric Effects in Noncentrosymmetric and Cuprate Superconductors" (2015). *Theses and Dissertations*. 1005.
<https://dc.uwm.edu/etd/1005>

This Dissertation is brought to you for free and open access by UWM Digital Commons. It has been accepted for inclusion in Theses and Dissertations by an authorized administrator of UWM Digital Commons. For more information, please contact open-access@uwm.edu.

**THEORETICAL STUDY OF
MAGNETOELECTRIC EFFECTS IN
NONCENTROSYMMETRIC AND CUPRATE
SUPERCONDUCTORS**

by

Manoj K. Kashyap

A Dissertation Submitted in
Partial Fulfillment of the
Requirements for the Degree of

Doctor of Philosophy
in Physics

at

The University of Wisconsin-Milwaukee

August 2015

ABSTRACT
THEORETICAL STUDY OF
MAGNETOELECTRIC EFFECTS IN
NONCENTROSYMMETRIC AND CUPRATE
SUPERCONDUCTORS

by

Manoj K. Kashyap

The University of Wisconsin-Milwaukee, 2015
Under the Supervision of Professor Daniel F. Agterberg

A century after the discovery of superconductivity at the lab of Kamerlingh Onnes in 1911, it is noticeable that the phenomenon is quite ubiquitous in nature. In addition to a long list of superconducting alloys and compounds, almost half the elements in the periodic table superconduct. By the late seventies, superconductivity was thought to be well understood. This turned out to be a myth, with the discovery of unconventional superconductors that defied Bardeen-Cooper-Schrieffer (BCS) theory. Cuprates have been the most prominent example among them ever since their discovery in 1986 by Bednorz and Müller. Another example of non-compliance with BCS theory lie among noncentrosymmetric superconductors. In this dissertation, magnetoelectric (ME) effects in these two classes of superconductors have been studied from different perspectives, utilizing Ginzburg-Landau (GL) theory. Even though GL theory was proposed before the BCS theory, it was not given much importance due to its phenomenological nature until Gor'kov proved that it is a limiting form of the microscopic BCS theory. However today, in the absence of any complete microscopic theory to explain superconductivity in unconventional superconductors, Ginzburg-Landau theory is an important tool to move ahead and qualitatively understand the behavior of varied superconducting systems.

Noncentrosymmetric superconductors have generated much theoretical interest since 2004 despite been known for long. The absence of inversion symmetry in non-centrosymmetric superconductors allows for extra terms called Lifshitz invariants in the Ginzburg-Landau functional. This leads to magnetoelectric effects that do not exist in centrosymmetric superconductors. One manifestation of this is in the vortex structure in materials with a cubic point group O . In particular, a current is predicted to flow parallel to the applied magnetic field in such a vortex in addition to the usual vortex supercurrents. In this work, we present both analytical and numerical solutions of the Ginzburg-Landau equations that reveal the spatial structure of this current as well as the associated component of the magnetic field for both a single vortex and in the vortex lattice phase near the upper critical field.

The discovery of superconductivity in lanthanum barium copper oxide (LBCO) in 1986, was followed by yttrium barium copper oxide (YBCO) in 1987, commencing the era of high temperature superconductivity. The astonishingly rich phase diagram of cuprates includes the pseudogap phase which was earlier thought to be a precursor to superconductivity. Now signatures of broken symmetries have been seen, indicating a true phase transition. Pair density wave (PDW) order has earlier been proposed to account for superconducting correlations and charge density wave (CDW) order in pseudogap phase. There is evidence that the pseudogap phase in the cuprates also breaks time-reversal symmetry. Here we show that pair density wave (PDW) states give rise to a translational invariant nonsuperconducting order parameter that breaks time-reversal and parity symmetries, but preserves their product. This secondary order parameter has a different origin, but shares the same symmetry properties as a magnetoelectric loop current order that has been proposed earlier in the context of the cuprates to explain the appearance of intracell magnetic order. We further show that, due to fluctuations, this secondary loop current order, which breaks only discrete symmetries, can preempt PDW order, which breaks both

continuous and discrete symmetries. In such a phase, the emergent loop current order coexists with spatial short-range superconducting order and possibly short-range charge density wave (CDW) order. Finally, we propose a PDW phase that accounts for intracell magnetic order and the polar Kerr effect, has CDW order consistent with x-ray scattering and nuclear magnetic resonance observations, and quasiparticle (QP) properties consistent with angle-resolved photoemission spectroscopy. Our work, consistently accommodates all observations of broken symmetries in pseudogap phase in a single theory.

©Copyright by Manoj K. Kashyap, 2015
All Rights Reserved

To my parents

TABLE OF CONTENTS

	Page
LIST OF FIGURES	xi
LIST OF TABLES	xii
ACKNOWLEDGMENTS	xiii
1 Introduction	1
1.1 Noncentrosymmetric Superconductors	11
1.2 Cuprates	16
1.2.1 Structure of Cuprates	18
a) Kinds and Composition of Layers in Cuprates	19
b) Basic structure	21
1.2.2 Phase Diagram and Broken Symmetries	22
1.3 ARPES	25
2 Ginzburg-Landau Theory	29
2.1 Landau Theory of Phase Transitions	30
2.2 Ginzburg Landau Functional	35
2.2.1 Absence of fields and gradients	35
2.2.2 Fields and gradients	38
2.3 Ginzburg-Landau Equations	39
2.4 Type I and Type II Superconductors	41
2.5 Single-vortex solution	44
2.6 Lifshitz Invariants	46
2.6.1 Lifshitz invariants for C_{4v} group	47
3 Vortices in Cubic Noncentrosymmetric Superconductors	49
3.1 Introduction	49
3.2 Ginzburg Landau Free Energy	50
3.3 Single-vortex structure	51
3.3.1 London limit	52
3.3.2 Numerical solution	55
3.4 Transverse field distribution near the upper critical field	60
3.5 Conclusions	63

4	Emergent Loop Current Order from Pair Density Wave Superconductivity	65
4.1	Introduction	65
4.2	PDW induced translational invariant loop current order	68
4.3	GLW Action: tetragonal symmetry	70
4.4	Secondary order parameters	72
4.5	GLW Action: orthorhombic symmetry	73
	4.5.1 Ground states	74
	4.5.2 Emergent loop current order - Orthorhombic symmetry	76
4.6	In-plane loop current order – tetragonal symmetry	78
4.7	Tilted loop current order	85
4.8	Quasiparticle properties of loop current PDW phases	86
4.9	Conclusions	88
	References	91
A	Modified Bessel functions	99
A.1	Some properties of Modified Bessel functions	99
	A.1.1 Limiting forms for small arguments	100
	A.1.2 Asymptotic expansions	100
B	Numerical codes	101
B.1	London limit solution	101
B.2	Full solution	107
C	Tetragonal PDW pairing at high symmetry points	120
C.1	Tetragonal symmetry ($\delta K_y = 0$)	120

LIST OF FIGURES

Figure 1.1:	Predicted behavior of metals before the discovery of superconductivity.	2
Figure 1.2:	Resistance (ohms) versus temperature (kelvin) for mercury showing the superconducting transition at 4.20 K. . .	3
Figure 1.3:	(a) Below T_c , field is excluded from entering a perfect conductor. (b) Flux is trapped inside a perfect conductor when it is cooled, to $T < T_c$, in a magnetic field. (c) Below T_c , field is excluded from entering a superconductor. (d) Field in an originally normal sample is expelled out of a superconductor, when it is cooled to $T < T_c$	4
Figure 1.4:	Temperature dependence of the critical field. Superconducting transition is second order at T_c in zero field whereas it is of the first order in the presence of a field.	5
Figure 1.5:	Upper critical field $B_{c2}(0)$ versus transition temperature T_c for heavy fermion and related superconductors. In particular, red symbols indicate NCS superconductors. The dotted line corresponds to the Pauli limit B_P^{BCS} . It can be seen that for the NCS superconductors shown here, $B_{c2}(0) > B_P^{BCS}$	13
Figure 1.6:	Filled β -Mn type structure of $\text{Mo}_3\text{Al}_2\text{C}$. $\text{Li}_2(\text{Pd}, \text{Pt})_3\text{B}$ also crystallize in the very same structure.	15
Figure 1.7:	Spin relaxation rate versus temperature for $\text{Li}_2\text{Pd}_3\text{B}$	15
Figure 1.8:	Superconducting T_c versus year of discovery for various families of superconductors.	17
Figure 1.9:	Perovskite structure.	18
Figure 1.10:	Crystal structure of YBCO.	20
Figure 1.11:	Phase diagram of hole doped cuprates.	23

Figure 1.12: ARPES geometry.	25
Figure 2.1: Landau functional vs. order parameter, when the cubic term is present. The cubic term leads to first order transition.	33
Figure 2.2: Order parameter minimum vs. temperature, when the cubic term is present in Landau functional. The cubic term leads to first order transition.	34
Figure 2.3: GL free energy versus order parameter.	36
Figure 2.4: Behavior of the order parameter at nucleation field H_{c2}	43
Figure 2.5: Temperature dependence of the critical field in type II superconductors.	43
Figure 3.1: Order parameter (f) vs. radial distance from vortex center (x). Order parameter rises to its maximum value increasingly faster with larger values of κ	57
Figure 3.2: B_z vs. x . $B_z(0) = B_{oz}$ is finite as against the divergence in the London limit.	57
Figure 3.3: Magnetic flux density B_ϕ for $\mu = 0.020$	58
Figure 3.4: Magnetic field H_ϕ for $\mu = 0.020$	58
Figure 3.5: Components of current density \mathbf{J} . Plot of J_z correspond to $\mu = 0.020$	59
Figure 3.6: The plot shows the agreement between full solution and the london limit solution of current density J_z . Current density J_z as a function of radial distance.	59
Figure 3.7: Peak Current (J_{zmax}) varies non-linearly with κ (for fixed μ). The dashed line is cubic spline fit.	60
Figure 3.8: Transverse flux density (B_\perp) distribution near upper critical field, for $eB_o < 0$. The dark circles denote the position of vortex lines. The direction of the field lines is determined by the sign of ϵ	62
Figure 4.1: Qualitative temperature (T) versus hole doping (p) phase diagram. Here LC represents the ME loop current phase, PDW represents the pair density wave phase, AF represents antiferromagnetism, and d-SC represents d -wave superconductivity.	67

Figure 4.2:	The positions of the momenta \mathbf{K}_i about which PDW Cooper pairs are formed for orthorhombic/tetragonal symmetry, when $\delta K_y \neq 0$	70
Figure 4.3:	The ME PDW state for orthorhombic symmetry.	76
Figure 4.4:	The ME PDW state for tetragonal symmetry.	79
Figure 4.5:	PDW state with the same symmetry properties as the tilted loop current state.	85
Figure 4.6:	Quasiparticle spectrum for the ME PDW state with $\delta K_y = 0.1$	87
Figure 4.7:	Spectral weight showing Fermi arcs for ME PDW state.	88
Figure C.1:	The positions of the momenta K_i about which PDW Cooper pairs are formed for tetragonal symmetry, when $\delta K_y = 0$	121

LIST OF TABLES

Table 2.1:	Character table for group C_{4v} with Lifshitz invariants for 1-D representations.	48
Table 4.1:	<p>Properties of PDW Ground States for orthorhombic symmetry in Fig. 4.2. All possible PDW ground states and accompanying CDW and ODW order. The second column shows the parameter regions for which these phases are stable. In the third and fourth columns: $2\mathbf{Q}_x = (2Q, 0)$, $2\mathbf{Q}_y = (0, 2Q)$, other modes can be found by using the relationships $\rho_{\mathbf{Q}} = (\rho_{-\mathbf{Q}})^*$ and $L_{\mathbf{Q}}^z = (L_{-\mathbf{Q}}^z)^*$. The fifth column gives all translational invariant order parameters with $l_x \propto \Delta_{\mathbf{Q}_1} ^2 - \Delta_{-\mathbf{Q}_1} ^2 - \Delta_{\mathbf{Q}_2} ^2 + \Delta_{-\mathbf{Q}_2} ^2$, $l_y \propto \Delta_{\mathbf{Q}_1} ^2 - \Delta_{-\mathbf{Q}_1} ^2 + \Delta_{\mathbf{Q}_2} ^2 - \Delta_{-\mathbf{Q}_2} ^2$, $\Delta_{4e,s} \propto \Delta_{\mathbf{Q}_1}\Delta_{-\mathbf{Q}_1} + \Delta_{\mathbf{Q}_2}\Delta_{-\mathbf{Q}_2}$, $\Delta_{4e,d} \propto \Delta_{\mathbf{Q}_1}\Delta_{-\mathbf{Q}_1} - \Delta_{\mathbf{Q}_2}\Delta_{-\mathbf{Q}_2}$, and $\epsilon_{xy} \propto \Delta_{\mathbf{Q}_1} ^2 + \Delta_{-\mathbf{Q}_1} ^2 - \Delta_{\mathbf{Q}_2} ^2 - \Delta_{-\mathbf{Q}_2} ^2$. The sixth column gives the degeneracy of the ground state.</p>	75
Table C.1:	<p>Properties of PDW Ground States for tetragonal symmetry in Fig. C.1. All possible PDW ground states and accompanying CDW and ODW order. The second column shows the parameter regions for which these phases are stable. In the third and fourth columns: $2\mathbf{Q}_x = (2Q, 0)$, $2\mathbf{Q}_y = (0, 2Q)$, other modes can be found by using the relationships $\rho_{\mathbf{Q}} = (\rho_{-\mathbf{Q}})^*$ and $L_{\mathbf{Q}}^z = (L_{-\mathbf{Q}}^z)^*$. The fifth column gives all translational invariant order parameters with $l_x \propto \Delta_{\mathbf{Q}_2} ^2 - \Delta_{-\mathbf{Q}_2} ^2$, $l_y \propto \Delta_{\mathbf{Q}_1} ^2 - \Delta_{-\mathbf{Q}_1} ^2$, $\Delta_{4e,s} \propto \Delta_{\mathbf{Q}_1}\Delta_{-\mathbf{Q}_1} + \Delta_{\mathbf{Q}_2}\Delta_{-\mathbf{Q}_2}$, $\Delta_{4e,d} \propto \Delta_{\mathbf{Q}_1}\Delta_{-\mathbf{Q}_1} - \Delta_{\mathbf{Q}_2}\Delta_{-\mathbf{Q}_2}$, and $\epsilon_{xx} - \epsilon_{yy} \propto \Delta_{\mathbf{Q}_2} ^2 + \Delta_{-\mathbf{Q}_2} ^2 - \Delta_{\mathbf{Q}_1} ^2 - \Delta_{-\mathbf{Q}_1} ^2$. The sixth column gives the degeneracy of the ground state.</p>	122

ACKNOWLEDGMENTS

I wish to express my sincere gratitude and great appreciation to my doctoral advisor, Professor Daniel Agterberg, for his invaluable guidance, encouragement and especially for his exemplary patience with me during all these years of my PhD. His support has been very extremely critical towards the completion of my doctorate. I also take the opportunity to thank other members of my PhD committee – Professor Bimal Sarma, Professor Dilano Saldin, Professor Michael Weinert and Professor Prasenjit Guptasarma – for their constructive comments that improved upon the style and content of this dissertation.

Drew Melchert, from University of Chicago, deserves a special mention here. He was instrumental in numerically generating quasiparticle spectra that added to the credibility of an important part of the work included in this dissertation. I thank him for this and wish him good luck for his future.

I would also like to thank the members of the physics faculty who imparted to my knowledge and understanding of physics during the coursework of the graduate school. Finally, I extend my thanks to all those people who positively contributed, in whatever way, towards my progress.

‘ ‘Wisdom is not
a product of schooling
but of the lifelong
attempt to acquire it.’ ’

Albert Einstein

(Mar 14, 1879 - Apr 18, 1955)

Chapter 1

Introduction

At the turn of the 20th century, one of the major question in physics was that what would happen to electrical resistance at temperatures close to absolute zero given that resistivity of a metal was known to decrease linearly with temperature [1, 2, 3]. Matthiessen's rule predicted the existence of residual resistivity at low temperatures depending upon the amount of impurities in the metal. According to Lord Kelvin, the electrons would re-condense onto their parent atoms causing decrease in electron mobility. Thereby the resistivity would bottom out and then increase again with further decrease in temperature, reaching infinity at absolute zero with electrons frozen in place. A third proposal was that the resistance would continue to decrease in an orderly fashion, ultimately reaching zero at absolute zero. These three predictions are shown in Fig. 1.1. The latter idea got more credence with the advent of Einstein's theory of quantum oscillators in 1906.

Around the same time, Dutch physicist Heike Kamerlingh Onnes (1853-1926) at Leiden University in the Netherlands was striving to liquefy the helium gas. On the fateful day of 10 July 1908, he succeeded in his persistent attempts and thus widened the horizons of low temperature physics to a few degrees Kelvin. This was followed by the serendipitous discovery of the phenomena of superconductivity [4] in 1911 by

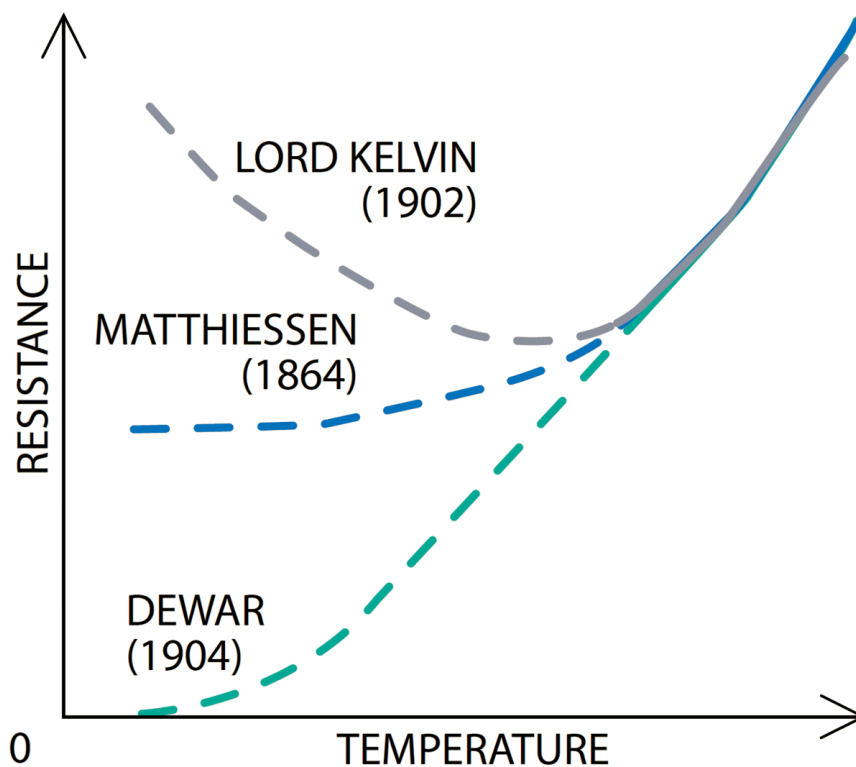


Figure 1.1: Predicted behavior of metals before the discovery of superconductivity. Figure reproduced from Ref. [1].

Onnes and his coworkers. They observed that the resistance of mercury abruptly became practically zero at about 4.2 K as the temperature was lowered and it appeared again at the same temperature when the temperature was increased (see Fig. 1.2). The observed change was too sudden to be explained by Einstein model. The phenomenon was also found to exist in other metals like lead and tin. Later, Onnes established what he called a ‘persistent supercurrent’ in lead coil with imperceptible decay. He observed that magnetic field can quench superconductivity which also implied that the phenomenon was limited by certain critical current. Refs. [1, 2, 3] give wonderful accounts of the events that led to the discovery of superconductivity and what followed.

Ever since the discovery, the phenomena of superconductivity has fascinated the physicists. Apart from the zero d.c. electrical resistance or *perfect conductivity* be-

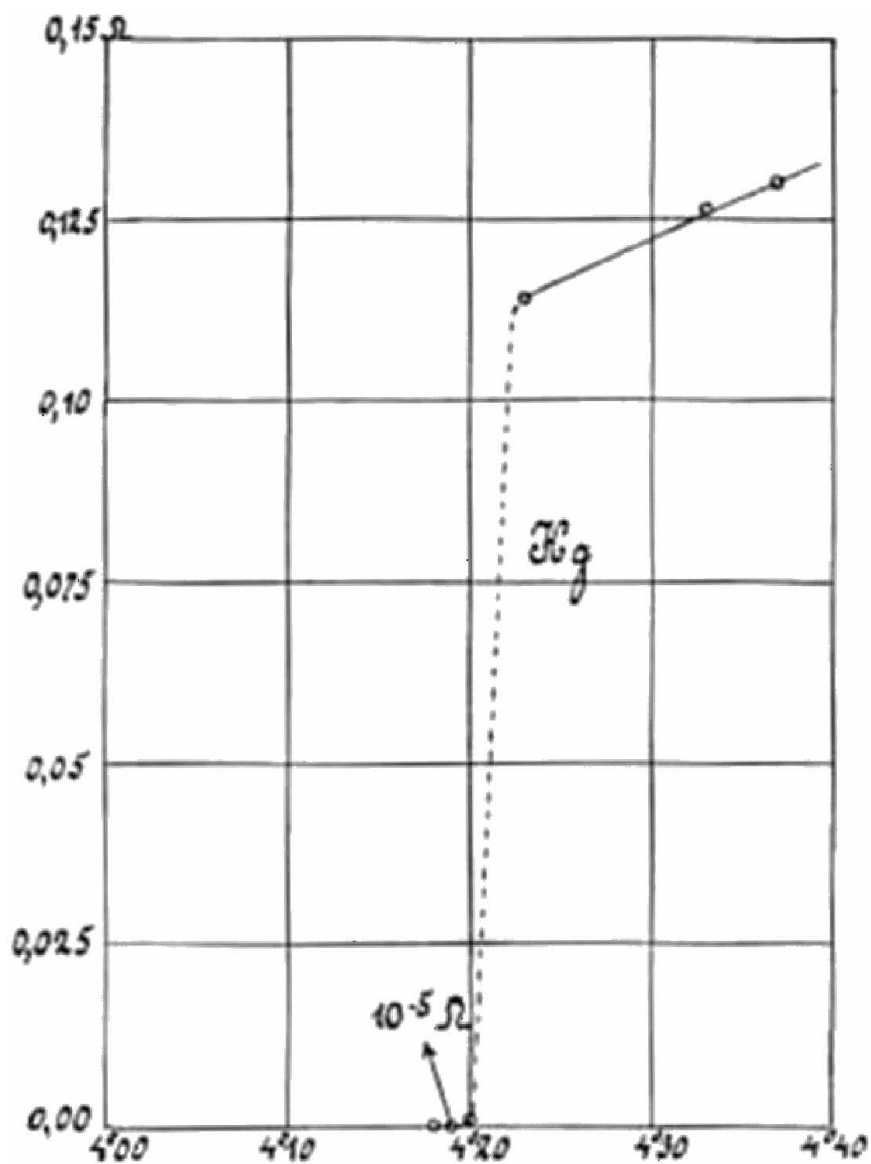


Figure 1.2: Resistance (ohms) versus temperature (kelvin) for mercury showing the superconducting transition at 4.20 K. Figure reproduced from Ref. [2].

low a critical temperature T_c (characteristic of the material), the other hallmark of superconductivity is *perfect diamagnetism*. It was discovered in 1933 (22 years after the original phenomenon) by Meissner and Ochsenfeld [5] and thus given the name *Meissner effect*. They observed that not only a magnetic field is excluded from entering a superconductor (Fig. 1.3(c)), but also that a field in an originally normal sample is expelled as it is cooled to $T < T_c$ (Fig. 1.3(d)).

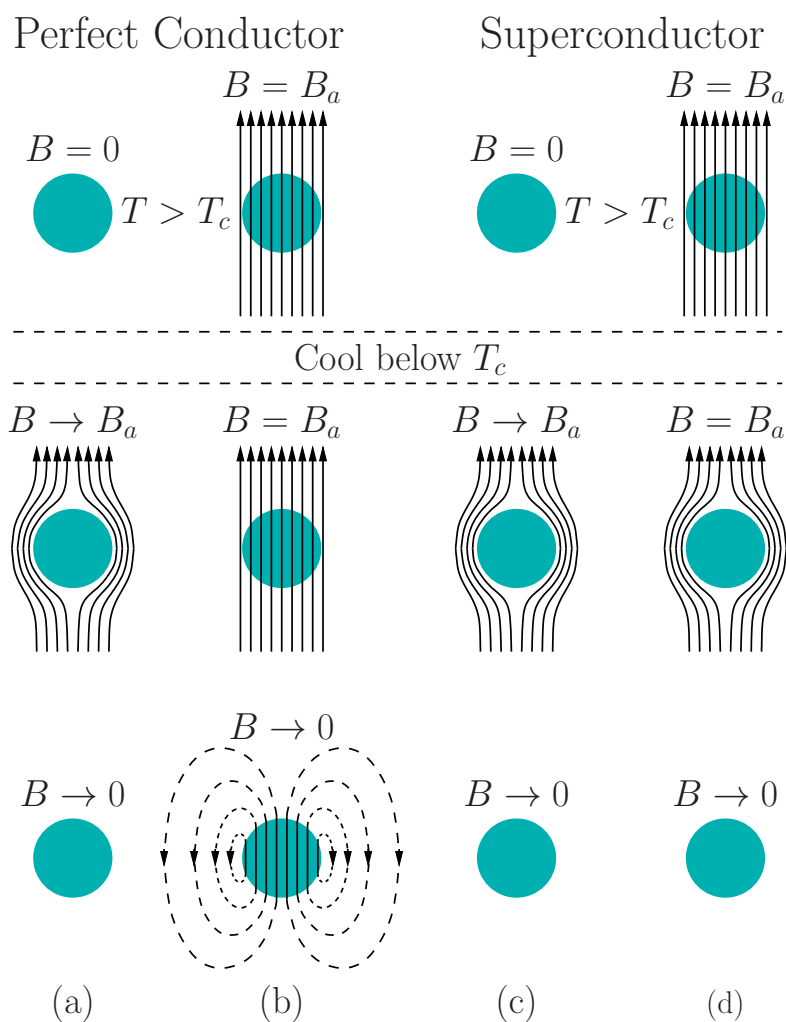


Figure 1.3: (a) Below T_c , field is excluded from entering a perfect conductor. (b) Flux is trapped inside a perfect conductor when it is cooled, to $T < T_c$, in a magnetic field. (c) Below T_c , field is excluded from entering a superconductor. (d) Field in an originally normal sample is expelled out of a superconductor, when it is cooled to $T < T_c$.

The existence of the reversible Meissner effect implies that superconductivity is destroyed by a thermodynamic critical magnetic field H_c , which is related to the so-called ‘*condensation energy*’ of the superconducting state

$$\frac{H_c^2(T)}{8\pi} = f_n(T) - f_s(T), \quad (1.1)$$

where f_n and f_s are the Helmholtz free energies per unit volume in the normal and superconducting states respectively. Empirically, $H_c(T)$ is quite well approximated by a parabolic law

$$H_c(T) = H_c(0)[1 - (T/T_c)^2], \quad (1.2)$$

as illustrated in Fig. 1.4. In the absence of magnetic field, superconducting transition at T_c is of second order. In a magnetic field, first order superconducting transition

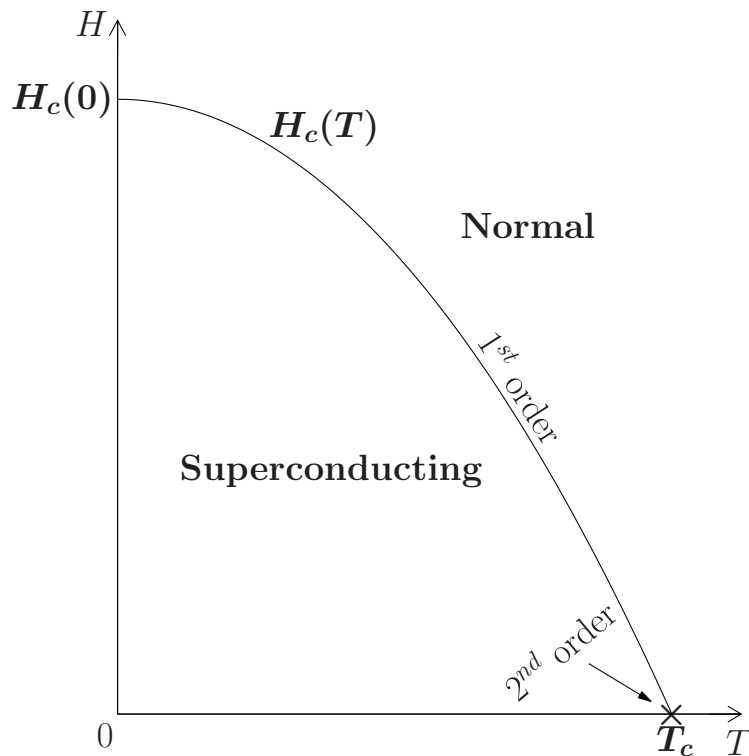


Figure 1.4: Temperature dependence of the critical field. Superconducting transition is second order at T_c in zero field whereas it is of the first order in the presence of a field.

occurs (in type I superconductors*) because of discontinuous change in the thermodynamic state of the system across transition and an associated latent heat.

On the theoretical front, the first notable progress was made by London brothers. In 1935, Fritz London and Heinz London proposed a phenomenological theory [6] based on *two-fluid picture* to explain the electrodynamic properties of superconductors. Such a picture assumed that below T_c , electrons form two kinds of fluids: a fluid of normal electrons with concentration n_n and superfluid of concentration n_s , where $n_n + n_s = n$. This theory led to a characteristic length scale called London penetration depth λ , with a limiting value at $T = 0$ given by

$$\lambda_L(0) = \sqrt{\frac{mc^2}{4\pi ne^2}}, \quad (1.3)$$

where $n_s \approx n$, the total number of conduction electrons. London penetration depth was found to be always smaller than the actual superconducting penetration depths. This was later explained by Alfred Brian Pippard [7] on the basis of nonlocal generalization of London theory in analogy with nonlocal generalization of Ohm's law and thereby introducing the idea of coherence length ξ .

The more serious limitations of London theory are: 1) It treats superfluid density n_s as given without giving any insight about its dependence on, for e.g., temperature or magnetic field. 2) Superfluid density n_s is assumed to be uniform in space. These limitations were taken care of in another phenomenological theory put forward in 1950 by Vitaly Lazarevich Ginzburg and Lev Landau. It is discussed in Chapter 2.

Ginzburg-Landau theory was followed by the first microscopic theory of superconductivity by John Bardeen, Leon Cooper and John Robert Schrieffer in 1957 - the BCS theory [8, 9]. BCS theory relies on the *Cooper theorem* [10] which states that the ground state of a degenerate Fermi sea of electrons is unstable against formation of bound states, namely, electron pairs or *Cooper pairs* in the presence of an arbitrar-

*See Chapter 2 for a description of type I and type II superconductors.

ily small net attractive potential between the electrons. Note that BCS formalism is independent of the origin of pairing interaction. In BCS theory, the electrons at the Fermi surface form Cooper pairs of the form $(\mathbf{k} \uparrow, -\mathbf{k} \downarrow)$. From the symmetry point of view, if the spin part of the pair wavefunction is spin singlet $S = 0$ (the case considered by BCS) which is antisymmetric under parity then Pauli exclusion principle requires that the orbital part must be symmetric with $l = 0, 2, 4, \dots$. Based on this l value, the superconductors are called *s*-wave ($l = 0$), *d*-wave ($l = 2$), *g*-wave ($l = 4$) and so on. BCS choice of the interaction potential, $V_{\mathbf{k}\mathbf{k}'} = -V$, up to k values limited by the cutoff $\pm\hbar\omega_c$ about the Fermi energy and zero elsewhere, implies that the potential is independent of the direction of $\mathbf{k} - \mathbf{k}'$, effectively leads to choosing $l = 0$ for orbital part of the wavefunction. This choice is traditionally, in analogy with atomic physics, called *s*-wave pairing. Pair occupation fraction for the BCS ground state at $T = 0$ closely resembles the normal-metal Fermi function at $T = 0$ [11]. As mentioned in Ref. [11], “In particular, no gap opens up in \mathbf{k} space. Rather, the disorder associated with the partial occupation of these states with *random* phases” — in the normal metal at $T = T_c$ — “is being replaced” — at $T = 0$ — “by a single quantum state of the system, in which more or less the same set of many body states with various one-electron occupancies are now superposed with a fixed phase relation.” Moreover, pairing does lead to an isotropic gap in the energy spectrum.

The energy of a Cooper pair $(\mathbf{k} \uparrow, -\mathbf{k} \downarrow)$ is less than the energy of two independent electrons with momenta \mathbf{k} and $-\mathbf{k}$ by an amount $2\Delta(T)$ where $\Delta(T)$ is the minimum quasiparticle (QP) excitation energy per particle. The quasiparticle energy is given by

$$E_{\mathbf{k}} = \sqrt{\xi_{\mathbf{k}}^2 + \Delta^2}, \quad (1.4)$$

where $\xi_{\mathbf{k}} = \epsilon_{\mathbf{k}} - \mu$ is the kinetic energy w.r.t. Fermi level. At $T = 0$, the minimum excitation energy in the weak coupling limit ($N(0)V \ll 1$, where $N(0)$ is the density

of states at Fermi level) is

$$\Delta(0) = 1.764 k_B T_c \quad (1.5)$$

and at some finite temperature T , $\Delta(T)$ can be computed numerically from the self consistent gap equation

$$\frac{1}{N(0)V} = \int_{-\hbar\omega_c}^{\hbar\omega_c} \frac{\tanh \left[\frac{1}{2} \beta \sqrt{\xi^2 + \Delta^2} \right]}{2\sqrt{\xi^2 + \Delta^2}} d\xi. \quad (1.6)$$

The critical temperature T_c is the temperature at which $\Delta(T) \rightarrow 0$. Using this, the integral in Eq. (1.6) can be evaluated leading to

$$k_B T_c = 1.13 \hbar\omega_c \exp \left(-\frac{1}{N(0)V} \right). \quad (1.7)$$

The condensation energy of the BCS ground state in the weak coupling limit at $T = 0$ is the difference between the internal energies of the superconducting state and the normal state at $T = 0$

$$U_s(0) - U_n(0) = -\frac{1}{2} N(0) \Delta(0)^2 \quad (1.8)$$

which is equal to the condensation energy in Eq. (1.1).

In classic superconductors, the pairing interaction is the electron-electron interaction mediated by lattice vibrations/phonons. An electron moving through a conductor will attract nearby positive charges in the lattice. This deformation of the lattice causes another electron, with opposite spin, to move into the region of higher positive charge density. This indirect attraction overcomes the Coulomb repulsion between them and the two electrons become correlated. Because there are a lot of such electron pairs in a superconductor, these pairs overlap very strongly and form a highly collective condensate. In view of this, a natural choice for cutoff frequency ω_c is Debye frequency ω_D . Experimental validity of Eq. (1.5), with ω_D as cutoff, and the

isotope effect on measured thermodynamic critical field in consonance with Eq. (1.8) validate this picture of pairing mechanism.

Within two decades after the advent of BCS theory, superconductivity seemed to be a closed subject. It was well understood based on the BCS theory and extensions thereof that dealt with strong interactions. The highest T_c then observed was 23.2 K in Nb₃Ge. Then in 1979, superconductivity was observed in *heavy-fermion* metal CeCu₂Si₂ below 0.5 K. In heavy fermion metals the conduction electrons are f-shell electrons with very strong Coulomb repulsions between them leading to high effective mass $m^* \gg m_e$ at the Fermi energy. In the same year organic superconductor (TMTSF)₂PF₂ was discovered with $T_c = 1.1$ K. In 1986, J. G. Bednorz and K. A. Müller observed superconductivity in a ceramic material La_{2-x}Ba_xCuO₄ (layered perovskite cuprate La₂CuO₄ with some Ba substituted for La) with T_c of the order of 35 K. Fullerite K₃C₆₀ was found to be superconducting below 18 K in the year 1991. The latest class of superconductors includes iron based superconductors which are again layered compounds. The first among them, LaFePO was discovered to be superconducting ($T_c \approx 4$ K) in 2006. These discoveries and many others led to explorations of many new classes of superconductors. Today we know of several families of superconductors, namely elemental metals, alloys, classical compounds, organic superconductors, heavy-fermion superconductors, cuprates, noncentrosymmetric superconductors, iron pnictides, metal borides metal carbides, perovskites, fullerites, chalcogenides, high T_c superconductors and the list goes on. These classifications are based on chemical compositions, structures, range of transitions temperatures and other common properties. These classes are not mutually exclusive.

A much broader classification labels the superconductors as ‘*conventional superconductors*’ and ‘*unconventional superconductors*’. Conventional superconductors are largely *s*-wave superconductors which are more or less BCS type superconductors and the rest which do not fall in the conventional category are said to be unconventional

superconductors. In a normal state isotropic system (which is invariant under all spatial rotations i.e. elements of SO_3 group), the irreducible representations are labeled by values of orbital angular momentum, and the set of $2l+1$ spherical harmonics form the basis functions of the irreducible representations [12]. For s -wave superconductivity ($l=0$), only $U(1)$ gauge symmetry is broken and the superconducting phase is still isotropic. The other spherical harmonic channels are unconventional. In crystals, however, the normal state is not isotropic. The crystal symmetry \mathcal{G} consists of crystal point group G , gauge symmetry $U(1)$, and time reversal \mathcal{T} , i.e., $\mathcal{G} = G \times U(1) \times \mathcal{T}$. In this case, again s -wave superconductors break only $U(1)$ gauge symmetry and superconducting phase belong to the identity representation of the crystal point group G . In general, other forms of superconductivity like p -wave or d -wave can occur in crystals only when some other point group symmetry is broken in which case superconducting phase does not belong to identity representation of the point group of normal state crystal. Thus, superconductors that belong to the identity representation of the normal state are said to be conventional superconductors and those which do not follow this norm are called unconventional superconductors. See Ref. [12].

The work included in this dissertation involves the study of magnetoelectric (ME) effects in noncentrosymmetric superconductors and cuprates, so the next two sections provide a background about these two classes of superconductor and then the last section of this chapter provides a quick overview of the angle-resolved photoemission spectroscopy, which is an important tool to study the electronic structure of cuprates. However before that let us look at the pairing symmetry of the Cooper pairs in a little more detail. Within the BCS formalism (here it means zero center of mass momentum), from the spin perspective, two kinds of pairing is allowed – spin singlet and spin triplet. For the singlet pairing the total wavefunction is given by

$$\Psi(\mathbf{k}, -\mathbf{k}, s, s') = \frac{\psi(\mathbf{k}, -\mathbf{k})}{\sqrt{2}}(|\uparrow\downarrow\rangle - |\downarrow\uparrow\rangle), \quad \text{where } \psi(-\mathbf{k}, \mathbf{k}) = \psi(\mathbf{k}, -\mathbf{k}). \quad (1.9)$$

For spin triplet pairing, the total wavefunction is given by

$$\Psi(\mathbf{k}, -\mathbf{k}, s, s') = \begin{cases} [-d_x(\mathbf{k}, -\mathbf{k}) + id_y(\mathbf{k}, -\mathbf{k})] |\uparrow\uparrow\rangle \\ \frac{1}{\sqrt{2}} d_z(\mathbf{k}, -\mathbf{k}) (|\uparrow\downarrow\rangle + |\downarrow\uparrow\rangle) \\ [d_x(\mathbf{k}, -\mathbf{k}) + id_y(\mathbf{k}, -\mathbf{k})] |\uparrow\uparrow\rangle, \end{cases} \quad (1.10)$$

where $\mathbf{d}(-\mathbf{k}, \mathbf{k}) = -\mathbf{d}(\mathbf{k}, -\mathbf{k})$.

Since ψ is an even function and \mathbf{d} an odd function, in a superconducting crystal with inversion symmetry only one of the two channels (singlet or triplet) can exist, depending upon whether the crystal is even under inversion (singlet pairing) or odd under inversion (triplet pairing). However, if inversion symmetry is absent in the crystal structure, mixing between even and odd parity is allowed.

The singlet channel involves pairing between two electrons $|k, \uparrow\rangle$ and $|-k, \downarrow\rangle$. In 1959, Anderson showed that this pairing is possible only if the two states are degenerate [13]. Since these states are related by time reversal symmetry (\mathcal{T})

$$\mathcal{T}|k, \uparrow\rangle = |-k, \downarrow\rangle, \quad (1.11)$$

the symmetry of the system necessary to form Cooper pairs in this channel is time reversal symmetry. By the same type of analysis, Anderson, in 1984, showed that in addition to time reversal \mathcal{T} , inversion symmetry \mathcal{I} is necessary, so that the four states, $|k, \uparrow\rangle, |-k, \uparrow\rangle, |k, \downarrow\rangle, |-k, \downarrow\rangle$, involved in triplet pairing are degenerate [14].

1.1 Noncentrosymmetric Superconductors

Noncentrosymmetric superconductors (NCS) have generated much theoretical interest [15]. At microscopic level, the primary impetus for this interest is the existence of a single particle antisymmetric spin-orbit coupling, for e.g., Rashba coupling and

Dresselhaus coupling, that exists when inversion symmetry is broken [15, 16, 17, 18]. Such an antisymmetric coupling can be represented as

$$H_{ASOC} = \alpha \sum_{\mathbf{k}, s, s'} \boldsymbol{\lambda}_{\mathbf{k}} \cdot \boldsymbol{\sigma}_{s, s'} c_{\mathbf{k}s}^\dagger c_{\mathbf{k}, s'}. \quad (1.12)$$

Symmetry under time reversal requires, $\boldsymbol{\lambda}_{\mathbf{k}} = -\boldsymbol{\lambda}_{-\mathbf{k}}$, whereas symmetry under inversion requires, $\boldsymbol{\lambda}_{\mathbf{k}} = \boldsymbol{\lambda}_{-\mathbf{k}}$. Hence, if a system possesses both of them (\mathcal{T} and \mathcal{I}), then this form of spin-orbit coupling is not allowed. However, if any of them is missing, then $\boldsymbol{\lambda} \neq 0$. NCS lack inversion symmetry and therefore $\boldsymbol{\lambda}_{-\mathbf{k}} = -\boldsymbol{\lambda}_{\mathbf{k}}$, which is an antisymmetric function and hence the name antisymmetric spin-orbit coupling.

This spin-orbit coupling is often a large energy scale with respect to the superconducting gap and leads to a variety of important consequences in the superconducting state. It has been predicted that this spin-orbit coupling leads to the mixing of spin-singlet and spin-triplet pairing states and that this mixing leads to: two-gap physics [15, 16, 19]; possible nodes in an *s*-wave superconductor [20, 21]; and topological superconductivity [22]. Furthermore, strong spin-orbit coupling implies that the spin susceptibility has the same temperature dependence for superconducting states that are predominantly spin-singlet and predominantly spin-triplet, indicating that spin susceptibility can no longer distinguish between these two possibilities [23, 24, 25, 26]. The behavior of NCS in magnetic fields also differs from that expected for centrosymmetric materials. In many cases, the upper critical field is larger than the Pauli limit [27, 28] as seen in Fig. 1.5 [29]. Fulde Ferrell Larkin Ovchinnikov (FFLO) like phases can appear [30, 31, 32, 33], and magnetoelectric (ME) effects associated with broken inversion symmetry are predicted [24, 28, 34, 35, 36, 37, 38, 39].

Despite being known since 1979 (CeCu₂Si₂), noncentrosymmetric superconductors have got prominent attention from researchers only since 2004 with the discovery of CePt₃Si followed by CeRhSi₃ and CeIrSi₃. These three and some others like CeCoGe₃,

UIr belong to the heavy fermion family. Many other superconductors, outside the heavy fermion family are also noncentrosymmetric superconductors. These include sesquicarbides R_2C_{3-y} ($R =$ rare earth), complex metallic alloy β' - Mg_2Al_3 , $BaPtS_3$, $Li_2(Pd, Pt)_3B$, Mo_3Al_2C , pyrochlores ($A_2B_2O_7$, AB_2O_6), T_2Ga_9 ($T = Rh, Ir$), $LaNiC_2$ etc. One major difference between heavy fermion NCS and others is the presence of f or d electronic configurations, which involve strong electronic correlations, in heavy fermion NCS. Such configurations are absent in those NCS which are outside the heavy fermion family. This makes it all the more important to study all classes of NCS so as to disentangle the effects of antisymmetric spin-orbit coupling owing to absence of inversion center, from those due to electronic correlations.

In Chapter 3, we present our phenomenological study of cubic NCS. At the phenomenological level, absence of inversion symmetry allows terms called ‘Lifshitz invariants’ that are linear in order parameter gradients, to enter the Ginzburg-Landau functional. Both Ginzburg-Landau theory and Lifshitz invariants are discussed in Chapter 2. Three of the materials among the cubic NCS category are $Li_2(Pd, Pt)_3B$, Mo_3Al_2C . All the three have filled β -Mn type structure, shown in Fig. 1.6, which lacks inversion symmetry along all principal axes. $Li_2(Pd, Pt)_3B$ belong to space group $P4_332$ whereas Mo_3Al_2C belongs to space group $P4_132$.

Li_2Pt_3B and Li_2Pd_3B show superconductivity at 2.7 and 7 K respectively [40, 41, 42, 43]. Mo_3Al_2C shows superconductivity at 9.2 K [44, 45, 46]. Li_2Pt_3B , has been proposed to be a s -wave superconductor with nodes due to the mixing of spin-singlet and spin-triplet superconductivity [21]. Li_2Pd_3B shows a Hebel-Slichter peak at $T \approx T_c$ in nuclear magnetic resonance (NMR) spectrum (see Fig. 1.7) and is also proposed to be a s -wave superconductor [47, 48]. Mo_3Al_2C [45, 46], shows hall marks of strong spin-orbit coupling relative to the superconducting gap. This is evidenced by the high critical fields [45, 46] and the temperature dependence of the spin susceptibility in the superconducting phase [49]. Specifically, it has been observed

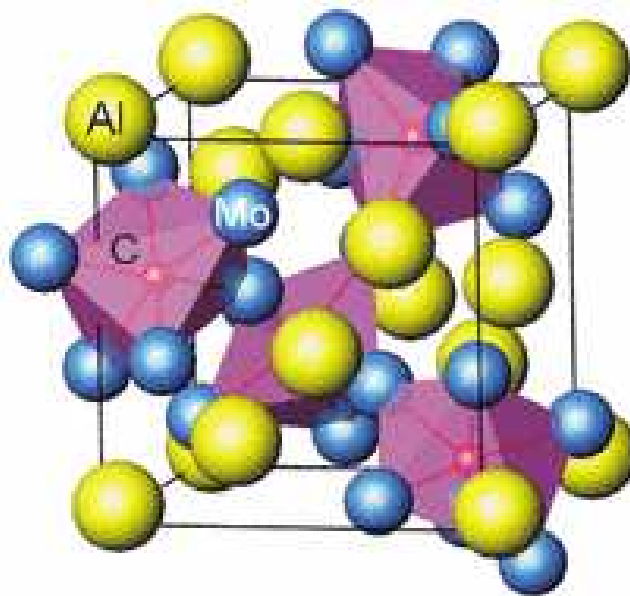


Figure 1.6: Filled β -Mn type structure of $\text{Mo}_3\text{Al}_2\text{C}$. Each cubic cell consists of four distorted octahedra of CMo_6 . $\text{Li}_2(\text{Pd, Pt})_3\text{B}$ share the same structure with C replaced by B, Al replaced by Li and Mo replaced by Pd(Pt). Figure reproduced from Ref. [46].

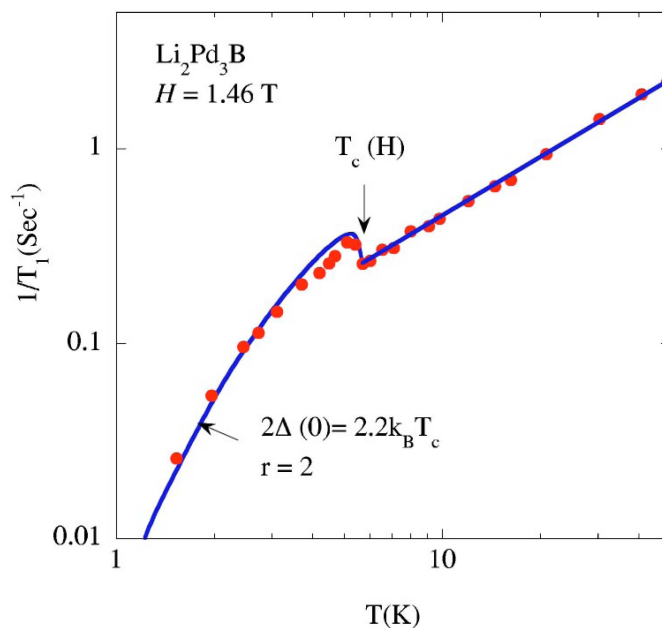


Figure 1.7: Solid dots correspond to NMR data representing spin lattice relaxation rate $1/T_1$ versus temperature T in a magnetic field $H = 1.4629$ T for $\text{Li}_2\text{Pd}_3\text{B}$. Above T_c the data is compatible with the relation $T_1T = \text{constant}$. At T_c the increase in relaxation rate (Hebel-Slichter) is clearly visible. Figure reproduced from Ref. [47].

that as the temperature approaches zero, the superconducting spin susceptibility is approximately $2/3$ the normal state spin-susceptibility [49]. This is what is predicted for a NCS cubic s -wave superconductor with strong spin-orbit coupling [26].

1.2 Cuprates

According to the BCS mechanism, weak attraction between electrons via electron-phonon coupling bind electrons into Cooper pairs, despite strong direct Coulomb repulsion, at energies smaller than the typical phonon energy. This, combined with the remarkable success of the BCS theory in understanding conventional superconductors, led to conclude that 30 K would be the upper limit of superconducting T_c . This limit for conventional superconductors has been revised in the previous decade by the discovery in 2001 of superconductivity in the simple metal MgB_2 at $T_c = 39$ K [50]. In this case, the increased T_c is due to strong coupling and two gap physics [51] that can still be described within the BCS realm. However, it was the discovery of the first copper oxide superconductor (barium doped lanthanum copper oxide LBCO) by Bednorz and Müller in 1986 that commenced the era of high temperature superconductivity. Apart from high T_c , superconductivity in cuprates was a surprise for two reasons: 1) Cuprates being ceramics are such poor conductors that they cannot be classified as metals at room temperature and 2) With the slight change in their chemical composition, they become highly insulating antiferromagnets. Magnetism arises from strong repulsive interactions between electrons whereas superconductivity arises from induced attractive interactions between electrons. Hence the two phenomena seem to be incompatible [52]. The 1986 discovery was followed by another big jump in $T_c \sim 90$ K with the discovery of $\text{YBa}_2\text{Cu}_3\text{O}_{7-\delta}$ (YBCO) [53, 54, 55]. Apart from YBCO, other systems in copper oxides that are known to have high transition temperatures are BSCCO (mixed oxides of bismuth, strontium, calcium and copper),

TBCCO (mixed oxides of thallium, barium, calcium and copper), HBCCO (mixed oxides of mercury, barium, calcium and copper). In YBCO, Y (yttrium) can be replaced by many other rare earth elements, for e.g., La, Nd, Sm, Eu, Gd, Ho, Er and Lu, with similarly high T_c . The highest T_c reported as of now is $134 \sim 135$ K under ambient pressure [56] and $164 \sim 165$ K under high pressure [57] in ‘mercury’ copper oxides. Fig. 1.8 shows superconducting transition versus year of discovery for various classes of superconductors. For long, the term ‘high temperature superconductors’ has been used interchangeably with ‘cuprates’. This monopoly of cuprates is being challenged by the discovery of MgB_2 , fullerides like Cs_3C_{60} and specifically iron based superconductors where the T_c values approach 60 K which is well above the classical limit of 30 K. There is a theoretical prediction, yet to be verified, by Neil W. Ashcroft about solid metallic hydrogen to exhibit superconductivity at room temperature under extremely high pressure [58]. From the theoretical perspective, superconductors

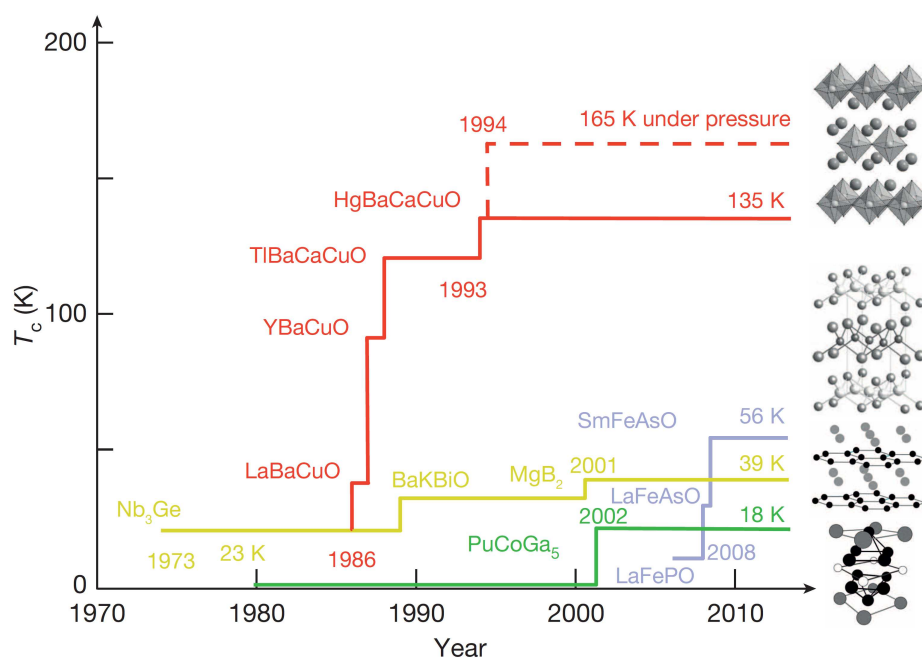


Figure 1.8: Superconducting T_c versus year of discovery for various families of superconductors. Crystal structures of representative materials are shown on the right. Lines of progression, for conventional superconductors (yellow), heavy fermion superconductors (green), cuprates (red), and recently discovered ‘iron superconductors’ (purple), end with an indication of highest known T_c in respective families. Figure reproduced from Ref. [52].

with small Fermi energies, such that their T_c is larger fraction of their Fermi temperature compared to that in case of conventional superconductors are considered as high temperature superconductors, despite the fact that the absolute value of their T_c is smaller than that for conventional superconductors. Such superconductors include some organic and heavy fermion superconductors. Very recently, there is a report of conventional superconductivity at up to 190 K under high pressures in hydrogen sulphide (H_2S) [59]. Despite all this cuprates preserve their technological importance for their known high T_c values (much larger than others for which T_c crosses BCS limit) at ambient pressure and also that they are known to have very high upper critical fields. At the same time, the astonishing complexity of the cuprate phase diagram continue to attract a huge amount of research interest.

1.2.1 Structure of Cuprates

The structure of cuprates is related to perovskite structure shown in Fig. 1.9.

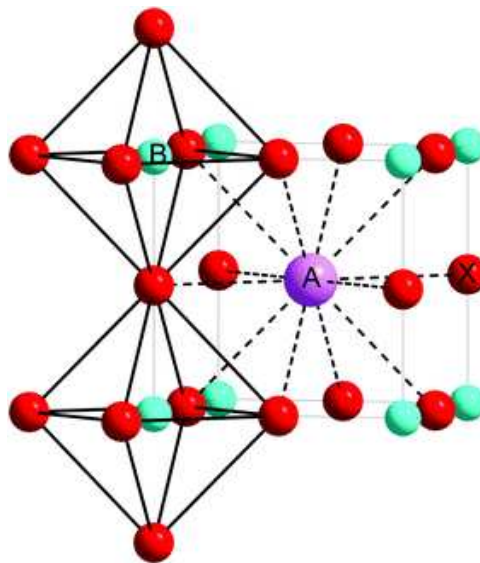


Figure 1.9: Perovskite structure[†]. A larger metal atom ‘A’ occupies the center of a cube. The smaller metal atom ‘B’ is present at the corners of the cube, and oxygen atoms are present at the edges of the cube forming an octahedral cage around the smaller metal atom.

[†]Source: <http://pubs.rsc.org/services/images/RSCpubs.ePlatform.Service.FreeContent.ImageService.svc/ImageService/Articleimage/2006/CP/b512271f/b512271f-f1.gif>

Cuprates have essentially a layered structure [60], in which each unit cell consists of four different types of layers. Fig. 1.10 shows the structure of YBCO.

a) Kinds and Composition of Layers in Cuprates

Conducting layers (DO_2) ‘D’. The superconductivity in cuprates occur in these layers. A conduction layer is formed of CuO_2 planes in which Cu atoms form a square mesh and O atoms are present at the center of edges of squares. A DO_2 layer can have as its closest neighbor either two BO layers (described below) so that each Cu atom is surrounded by six oxygen atoms or one BO and one C layer (described below) so that each Cu atom is surrounded by 5 oxygen atoms forming a square pyramid or two C layers such that each Cu atom is surrounded by four oxygen atom belonging to DO_2 layer itself. Copper may also be partly replaced by 3d-transition metals.

Separating layers (C) ‘C’. Separating layers are aptly name as they are inserted between two DO_2 layers and hence split the octahedron (in perovskites) into two square pyramids. A separating layer is either surrounded by two DO_2 layers or consecutive C layers (all sandwiched together between two DO_2 layers) are intercalated by O_2 layers just like the oxygen atom in the DO_2 layers. Separating layers are formed of a square mesh of metal atoms, usually Y or Ca atoms and sometimes La and other rare-earth metal atoms. These layers are not present in perovskite structure.

Bridging layers (BO) ‘B’. Bridging layers are located next to DO_2 layers and contain the apical oxygen atom of the octahedron or square pyramid of a DO_2 layer. These are present in perovskite structure. They consist of square mesh of metal atoms with oxygen atoms centering the squares. The metal atoms are usually Sr, Ba or La.

Additional layers (AO) ‘A’. These are metal-oxide layers. Typical metal are Th, Bi, Pb, C, Hg and even Cu sometimes (as in YBCO). These are never in direct contact with DO_2 layers instead separated from DO_2 layers by a bridging layer. The

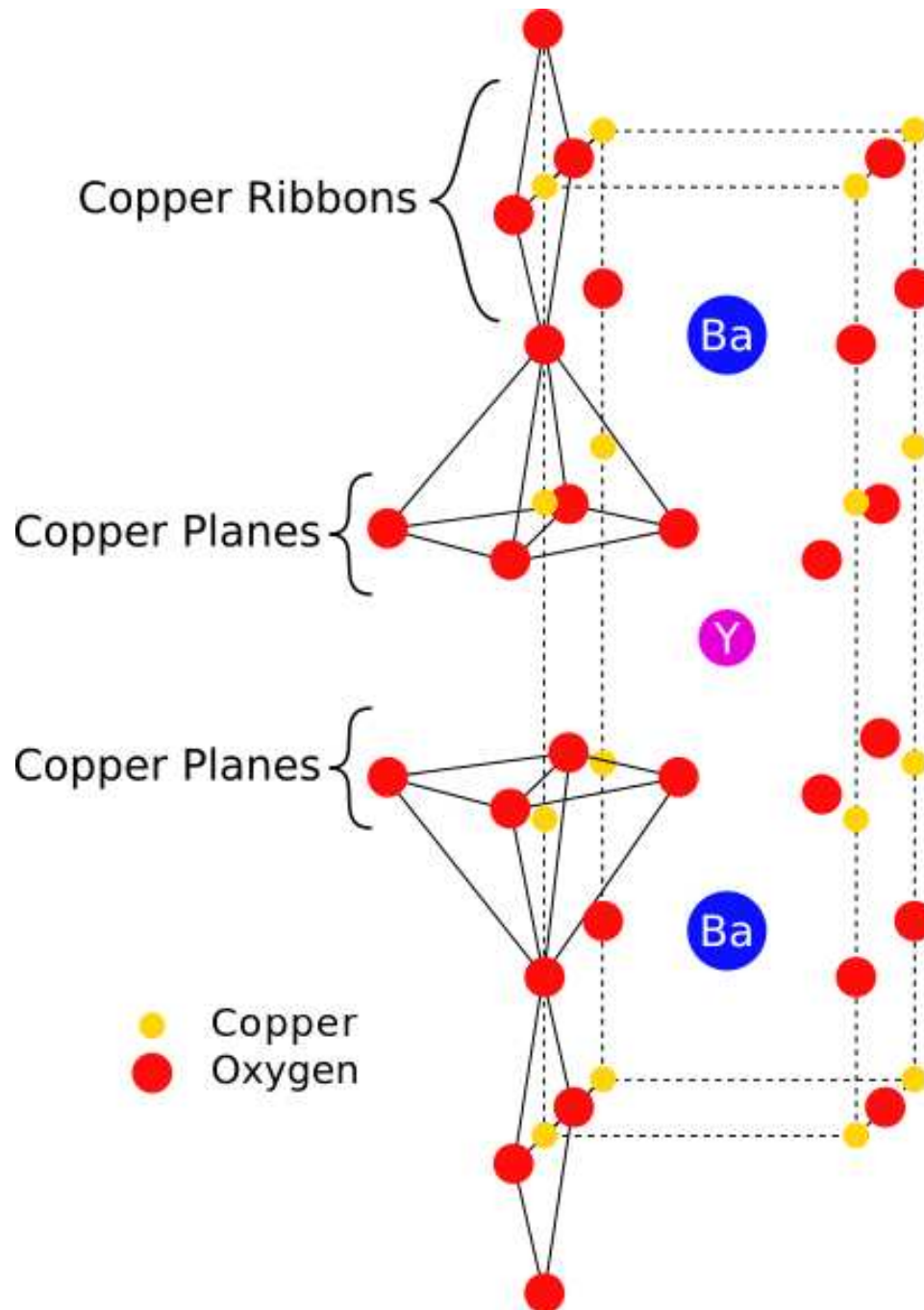


Figure 1.10: Crystal structure of YBCO (YBa₂Cu₃O_{7-x}). When $x = 1$ the oxygen sites in the additional layer are vacant and the structure is tetragonal. The tetragonal structure of YBCO does not superconduct. Superconductivity occurs when $0 \leq x \leq 0.65$. In this range CuO chains in the additional layers are formed in one direction, distorting the structure to orthorhombic. At $x \sim 0.07$ almost all the oxygen sites in CuO chains (in one direction) are filled, with only a few vacancies. This is when YBCO shows superconductivity at highest T_c of 95 K or at highest magnetic fields: 120 T for \mathbf{B} perpendicular and 250 T for \mathbf{B} parallel to CuO₂ planes. Figure reproduced from Ref. [61].

composition of additional layers can vary from A to AO₂. Metal cations ‘A’ are arranged in a regular square mesh and oxygen atoms may occupy different positions: A – contains no oxygen atoms; AO – oxygen atoms at the center of the squares; AO’ – oxygen atoms at the center of the square edges in one direction; AO₂ – oxygen atoms at the center of the square edges in both directions; AO’’ – partial occupancy at square edges. Additional layers can be stacked on each other to form slabs that are surrounded by a bridging layer on each side.

The layers defined above are generally stacked on top of each other such that the cation sites in neighboring layers are shifted by $\frac{1}{2}, \frac{1}{2}$ (barring a few exceptions in the YBCO family). This implies that the translation period in stacking direction must contain an even number of layers (excluding the O₂ layers between consecutive C layers) in a stacking unit. If the number of layers in a stacking unit is odd then the translational period in stacking direction must be doubled.

b) Basic structure

The general formula for a basic structure is

$$A_k B_l C_m D_n O_{k'+l+2m+2}, \quad (1.13)$$

where k' may or may not be equal to k (depending upon oxygen content in additional layers); $n \geq 1$; $m + l \geq n$; $m = p(n - 1)$ [p is number of consecutive C layers]; $l = 1$ or 2 ($k \neq 0$ then $l = 2$). When $N = k + l + m + n$ is even, the conventional cell of the undistorted structure contains one stacking unit, whereas if N is odd conventional cell contains two stacking units.

If there are no BO layers and consequently no AO layers, the structure ($C_p D O_{2p}$) is called ‘*limiting structure*’. In addition to this, if $p = 1$, then the structure corresponds to the so-called ‘*infinite layer compounds*’, for e.g., (Sr, La)CuO₂.

Basic structures are commonly denoted by a four digit code. For e.g LaCuO_{2.95} ($A_0B_1C_0D_1$) is denoted as 0101 and Tl_{1.64}Ba₂Ca₃Cu₄O₁₂ ($A_2B_2C_3D_4O_{12}$) is denoted as 2234. This code generally reflects the cation ratios in the compound, ignoring partial vacancies. Different chemical families are distinguished by preceding the four digit code by the chemical symbol of the cations in the additional layers for e.g. YBCO (Ba₂YCu₃O₇), often abbreviated as 123 or Y-123, is more properly denoted as 1212 or Cu-1212 (CuBa₂YCu₂O₇).

1.2.2 Phase Diagram and Broken Symmetries

Copper oxides are highly correlated electron systems. Ref. [52] provides an updated review on cuprate superconductors. Doped cuprates, in particular the hole doped cuprates, have an astonishingly rich phase diagram as evident from Fig. 1.11. The undoped parent compounds are Mott insulators at room temperature. At lower temperature an antiferromagnetic (AF) phase appears at the Néel temperature T_N that decreases with increase in doping concentration. A superconducting phase appears at a doping concentration p_{\min} . Superconducting order in cuprates is known to be d -wave order. The transition temperature T_c increases with doping until a critical value called ‘*optimal*’ doping p_{opt} is reached after which it starts decreasing. Beyond another characteristic doping concentration p_{\max} , superconductivity vanishes and a Fermi liquid phase, which is consistent with one-electron band theory, appears at low temperatures. For $p < p_{\text{opt}}$, the system is said to be ‘*underdoped*’ and a system with $p > p_{\text{opt}}$ is referred to as ‘*overdoped*’. In overdoped regime, a normal (non-superconducting) phase called ‘*strange metal*’ phase appears at higher temperatures. This phase is termed as strange metal because it does not conform to Fermi liquid theory obeyed by normal metals. In normal metals the resistivity goes as T^2 at low temperatures whereas in strange metal phase the resistivity is linear in T at low temperatures. On the other hand, resistivity in normal metals saturates at high temperatures whereas

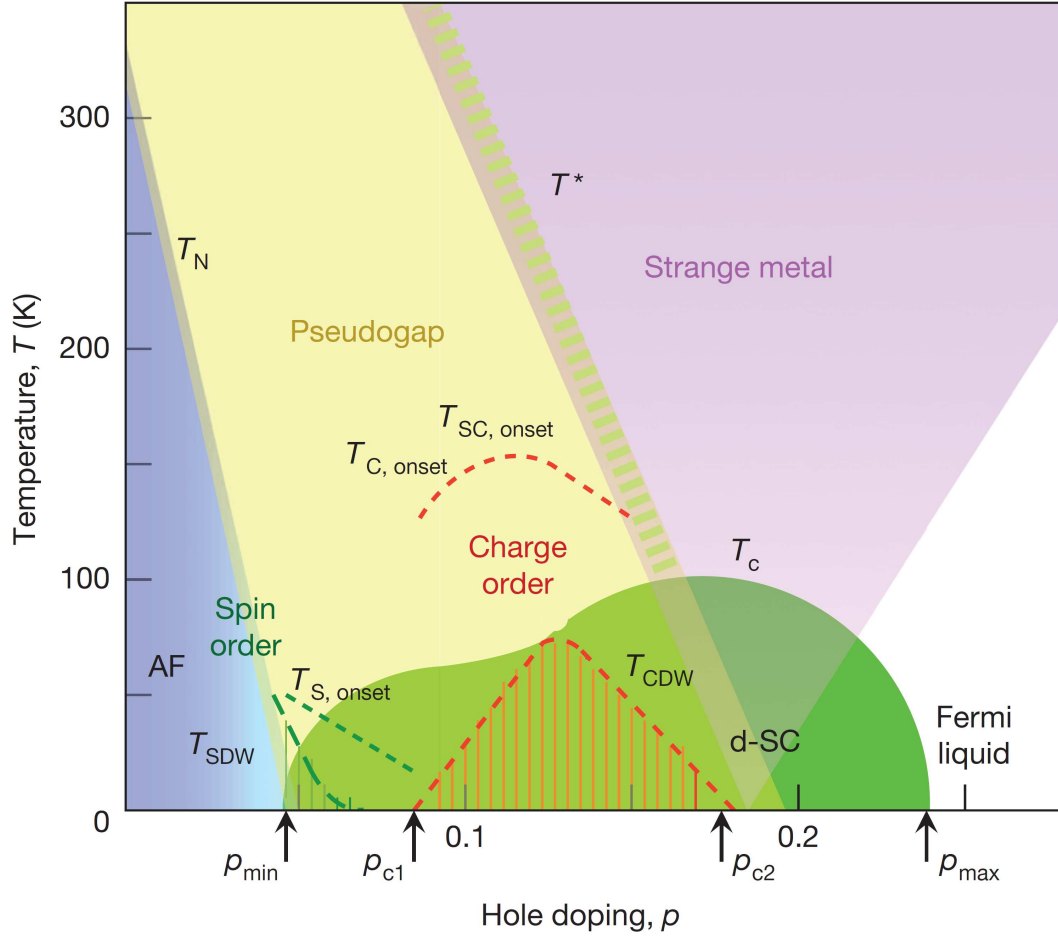


Figure 1.11: Phase diagram of hole doped cuprates. On the left, at low doping fully developed antiferromagnetic (AF) phase (blue region) sets in at Neél temperature T_N . Fully developed superconducting phase (green region), characterized by d -wave superconducting order, sets in at transition temperature T_c . At $T = 0$, superconducting region is bounded by two critical doping concentrations, namely p_{min} and p_{max} . Above p_{max} , Fermi liquid behavior emerges at low temperatures. At T_{CDW} , fully developed charge order (red striped region) sets in. T_{SDW} represents fully developed incommensurate spin density wave order. Pseudogap temperature T^* marks the crossover from strange metal phase (wedge shaped purple region) to pseudogap phase (yellow region) in the underdoped regime (see text). $T_{S, onset}$ (dotted green line), $T_{C, onset}$ and $T_{SC, onset}$ (dotted red line for both, in the pseudogap region) mark the temperatures at which precursor/incipient order or fluctuations, corresponding to spin, charge and superconductivity respectively, become apparent. Strange metal wedge is believed to be originating from quantum critical point (QCP) hidden in the superconducting region near optimal doping (see text) at $T = 0$. The arrows indicate the quantum critical points for superconductivity and charge order. Figure reproduced from Ref. [52]

in strange metal phase it can remain linear in T up to very high temperatures. Also, the Hall resistivity has a deviant temperature dependence in strange metals. These anomalies are attributed to the absence of quasiparticles in the strange metal phase [62, 63]. Some aspects of the strange behavior exhibited by strange metals could be explained within the so-called “marginal-Fermi-liquid phenomenology” [64], though with limited success [65]. Another idea being explored towards this goal is the existence of a quantum critical point (QCP) at $T = 0$, hidden inside the superconducting dome near optimal doping. This picture envisages that a quantum critical wedge opens up from QCP with increase in temperature [52], leading to the strange metal phase, above the superconducting dome, flanked by the so-called ‘*pseudogap*’ phase in the underdoped regime and Fermi liquid phase in the overdoped regime.

The strange metal behavior seems to be a general property of the strongly correlated electron systems and thus unlikely to be directly responsible for high- T_c superconductivity [52]. As opposed to this, the pseudogap phase is more unique to copper oxides. Therefore, even though strange metal problem in itself is quite important towards understanding the physics of quantum materials, it is understanding the origin of the pseudogap phase that is believed to be the central problem towards unraveling the mystery of high- T_c copper-oxide superconductors. The pseudogap phase appears at the pseudogap temperature T^* in the underdoped regime, as seen in the Fig. 1.11. This phase was originally thought to be a precursor phase to superconductivity with spin-singlet pairs, no phase coherence, and no broken symmetries [66, 67]. However, more recent measurements suggest the presence of broken symmetries. Specifically, polarized elastic neutron scattering observe intraunit cell magnetic order [68] at a temperature close to the onset of a polar Kerr effect [69, 70]. This suggests broken time-reversal symmetry [71, 72]. Also, static quasi-long-range charge density wave (CDW) order has been observed through x-ray scattering [73, 74, 75] and through nuclear magnetic resonance [76]. This order appears at the incommensurate wavevec-

tors $2\mathbf{Q}_x = (2Q, 0)$ and $2\mathbf{Q}_y = (0, 2Q)$ [74]. In addition, there exists evidence for superconducting (SC) correlations in the pseudogap phase. Diamagnetism is observed much above T_c [77] and also at fields that far exceed the estimated mean-field SC upper critical field [78]. The work presented in Chapter 4 of this dissertation provides a single framework to account for all observations of broken symmetries in the pseudogap phase of cuprates.

1.3 ARPES

Angle-resolved photoemission spectroscopy (ARPES) is a powerful technique to study electronic structure of solids. It is based on the photoelectric effect observed by Hertz (1887) and later explained by Einstein (1905) as a manifestation of dual nature of light (a light wave of frequency ν is composed of light quanta called photons, with each photon carrying the energy $h\nu$). Fig. 1.12 shows geometry of an ARPES experiment.

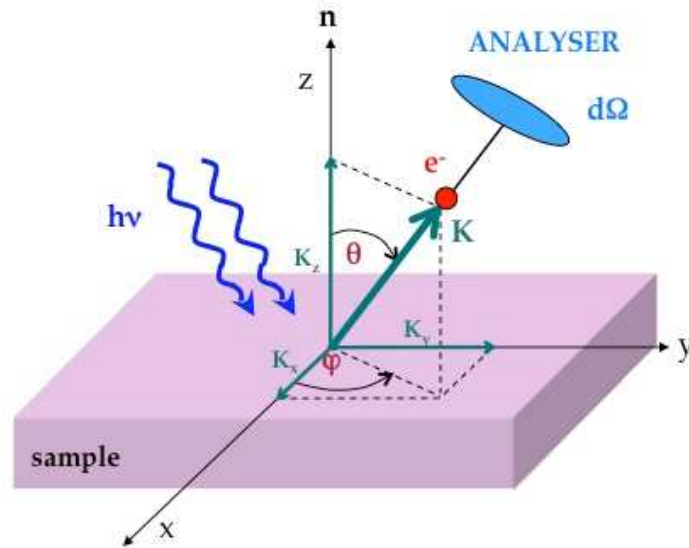


Figure 1.12: ARPES geometry[‡].

[‡]Source: <http://www.uj.ac.za/EN/Faculties/science/departments/physics/research/CondensedMatter/ElectronicStructurestudiesUJPhysics/PublishingImages/ARPES.jpg>

When a beam of monochromatic light with sufficient photon energy $h\nu$ is incident on a sample, electrons are emitted in all directions. Note that monochromatic light is not a precondition for photoemission process itself but perhaps required for analytic feasibility. The emitted photoelectrons are collected with an electron energy analyzer to measure their kinetic E_{kin} energy for a given emission angle. Kinetic energy is related to photoelectron momentum \mathbf{p} by: $p = \hbar K = \sqrt{2mE_{\text{kin}}}$, where K is the magnitude of the photoelectron wavevector.

By the law of conservation of energy (in the noninteracting electron limit)

$$E_{\text{kin}} = h\nu - \Phi - |E_{\text{B}}|, \quad (1.14)$$

where Φ is the work function (energy required by an electron to cross the surface into vacuum) and E_{B} is the Binding energy of the electron. Further, by the law of conservation of momentum (again in noninteracting electron limit)

$$\mathbf{k}_{\parallel} \approx \mathbf{K}_{\parallel} = \frac{1}{\hbar} \sqrt{2mE_{\text{kin}}} \sin \theta, \quad (1.15)$$

where $\hbar\mathbf{k}_{\parallel}$ is the component of the electron crystal momentum parallel to the surface ($x - y$ plane), in the *extended*-zone scheme. Here, we ignore the photon momentum because at the low photon energies used in ARPES, $p_{\text{photon}} = h/\lambda \ll 2\pi/a$, where ‘ a ’ is lattice parameter. ARPES is usually done with the ultraviolet light. Such low photon energies are used to achieve higher energy and momentum resolution [79]. The perpendicular component \mathbf{k}_{\perp} is not conserved due to the abrupt potential change across the surface and therefore $\mathbf{k}_{\perp} \neq \mathbf{K}_{\perp}$. One of the ways to determine \mathbf{k}_{\perp} is to repeat the measurements along surface normal over a range of incident photon energies [80]. However, \mathbf{k}_{\perp} is not very crucial for low dimensional system with negligible dispersion along the z -direction. This is the case with cuprates in which superconductivity lies in the CuO_2 planes and hence the electronic structure of

the CuO₂ bands is two-dimensional for all practical purposes. In such systems, only \mathbf{k}_{\parallel} is required to completely determine the electronic dispersion. Ref. [79] provides a detailed review of ARPES studies on cuprate superconductors.

For systems like cuprates, where the conventional methods fail to describe the electronic structure, ARPES is an important tool to provide insights into the many body physics involved. ARPES data yields direct information about the single particle spectral function and the associated Green's function. Often, photoemission spectra is treated under the so-called '*sudden approximation*', in which electron emission is assumed to be instantaneous, barring any interaction between an emitted electron and the system left behind so that the effective potential of the system changes abruptly.

Ignoring the effects of finite energy and momentum resolution and temperature effects, the ARPES intensity measured for a 2D single-band system (within the *sudden approximation* and taking $\hbar = 1$) is directly proportional to the product of the one-particle spectral function $A(\mathbf{k}, \omega)$ and the probability of transition an electron from an initial state to a final state (allowed by energy and momentum conservation), via photon absorption. The transition probability is given by $|\langle \phi_f^{\mathbf{k}} | H_{\text{int}} | \phi_i^{\mathbf{k}} \rangle|^2 \equiv |M_{f,i}^{\mathbf{k}}|^2$. In the dipole approximation, so that vector potential \mathbf{A} is constant over atomic dimensions and therefore consistent with the Coulomb gauge ($\nabla \cdot \mathbf{A} = 0$), the interaction Hamiltonian (for interaction between a photon and an electron) is given by $H_{\text{int}} = -(e/2mc)\mathbf{A} \cdot \mathbf{p}$.

In the absence of electron-electron correlations, spectral function consist of delta-function peak at band energy $\epsilon_{\mathbf{k}}$ i.e. $A(\mathbf{k}, \omega) = \delta(\omega - \epsilon_{\mathbf{k}})$. Effects of electronic correlations can be included in terms of the electron *proper self-energy* $\Sigma(\mathbf{k}, \omega) = \Sigma'(\mathbf{k}, \omega) + i\Sigma''(\mathbf{k}, \omega)$. In this case, Green's and spectral functions are given by

$$G(\mathbf{k}, \omega) = \frac{1}{\omega - \epsilon_{\mathbf{k}} - \Sigma(\mathbf{k}, \omega)}, \quad (1.16)$$

$$A(\mathbf{k}, \omega) = -\frac{1}{\pi} \text{Im} G(\mathbf{k}, \omega) = -\frac{1}{\pi} \frac{\Sigma''(\mathbf{k}, \omega)}{[\omega - \epsilon_{\mathbf{k}} - \Sigma'(\mathbf{k}, \omega)]^2 + [\Sigma''(\mathbf{k}, \omega)]^2}. \quad (1.17)$$

A correlated system can be described in terms of quasiparticles with renormalized energy and mass. This leads to separation of $G(\mathbf{k}, \omega)$ and $A(\mathbf{k}, \omega)$ into a coherent part with a single pole and an incoherent smooth part [79, 80]. The coherent part represent the main line which has a finite width, and therefore a finite life-time, due to imaginary part of self-energy Σ'' . Also the main peak is shifted with respect to bare band energy $\epsilon_{\mathbf{k}}$ due to the real part of self energy Σ' . Thus, electron self energy (real and imaginary parts) can be extracted from the ARPES spectra to study many body correlations in solids. For a detailed description of ARPES one can refer to several texts and articles available on the subject, say Ref. [81, 82].

Chapter 2

Ginzburg-Landau Theory

The BCS microscopic theory is well suited to situations where the energy gap Δ is spatially uniform. However in situations, like intermediate state in type I superconductors* and mixed state (Shubnikov phase) in type II superconductors*, that inevitably involve spatial inhomogeneity, a fully microscopic theory like BCS becomes too cumbersome. In such situations macroscopic Ginzburg-Landau (GL) theory is quite useful.

Even though GL theory (1950) [83] of superconductivity preceded the BCS theory (1957), it was not given much significance until 1959, due to its phenomenological nature, when Gor'kov [84] showed that the GL theory was derivable as a rigorous limiting case of the BCS theory, suitably reformulated in terms of Green's functions to deal with spatially inhomogeneous regime. The limiting conditions include – 1) Temperature is restricted to the neighborhood of T_c . 2) Variations in ‘*order parameter*’ (introduced in Section 2.1) and vector potential \mathbf{A} are slow enough. GL theory is based on previously established Landau theory of continuous (second order) phase transitions [85] introduced by Lev Davidovich Landau, one of the great physicists of 20th century, in the year 1937. Landau argues that phase transitions are effected by the sudden change of symmetry of the system. However, in contrast to first order

*Type I and type II described in Section 2.4

transition in which the thermodynamic state of the system changes discontinuously, in second order transitions the state of the system (specifically the energy) changes continuously. Therefore, at transition point the states of the two phases are the same in second order transitions and the symmetry of the system contains all the elements of symmetry of both the phases. This implies that the symmetry at transition point is the same as the symmetry everywhere on one side of that point and symmetry group of lower symmetry phase is a subgroup of that of the higher symmetry phase. In first order phase transitions, there is no such restriction and the symmetry of the two phases can be completely unrelated. General observation is that in great majority of cases the transition from more symmetrical phase to less symmetrical phase happens with decreasing temperature. In Section 2.1 we will look at the more general Landau theory. Later sections deal with the GL theory.

2.1 Landau Theory of Phase Transitions

Landau theory of 2nd order phase transitions is one of the several important contributions of Lev Landau. It plays an important role in many areas of condensed matter physics including structural and magnetic phase transitions. The central idea of the theory is the existence of a thermodynamic variable called *order parameter* which is zero in more symmetrical phase and takes non-zero values (positive or negative) in less symmetrical phase. The thermodynamic potential (free energy) of the system can be expressed as a functional of the order parameter η and other thermodynamic quantities such as temperature T , pressure P or volume V , magnetic field, etc. However the functional $\mathcal{F}(P, T, \eta)$ achieves a minimum at a given P and T (specified arbitrarily) and the value of η is determined from this condition of thermal equilibrium. In this sense η is not at the same footing as other variables. Note that the stability condition fixes the value of the order parameter which means that the fluctuations in order

parameter are neglected and therefore Landau theory is a mean-field theory. The continuity of the state of the system across transition requires η to take arbitrarily small values near transition point. Thus we can expand $\mathcal{F}(P, T, \eta)$ in a power series

$$\mathcal{F}(P, T, \eta) = \mathcal{F}_0 + \alpha\eta + A\eta^2 + C\eta^3 + B\eta^4 + \mathcal{O}(\eta^5), \quad (2.1)$$

where η , α , A , B , C , \dots are functions of P and T and \mathcal{F}_0 is the free energy of the normal phase (an inconsequential constant). We neglect the 5th and higher order terms

The functional $\mathcal{F}(P, T, \eta)$ must be invariant by all elements of the high symmetry group, and so must be each term of the expansion. Since the states with $\eta = 0$ and $\eta \neq 0$ are of different symmetry and $\mathcal{F}(P, T, \eta)$ must be invariant at transition point, therefore the coefficient of the linear term must be identically zero otherwise symmetry breaking transition is not possible. In other words *order parameter* η cannot be invariant under all operations of the high symmetry group. The linear term is allowed only in the presence of external field if the order parameter couples with it and the coupling term ηh (where h is generalized external field) is invariant under the elements of the high symmetry group. In such a case, at a given temperature $T < T_c$, if field is varied, a phase transition of first kind occurs at $h = 0$ [86]. Here, we shall not bother about the first order term. The coefficient $A(P, T)$ of the quadratic term vanishes at transition point. This is so because for $T > T_c$, the value of $\eta = 0$ must correspond to minimum of $\mathcal{F}(P, T, \eta)$ so in this phase $A > 0$ is necessary (second derivative must be positive), whereas for $T < T_c$, the minimum of $\mathcal{F}(P, T, \eta)$ must be at some non-zero value of η and it must be less than \mathcal{F}_0 , which is possible only if $A < 0$. Hence A must vanish at the transition point.

The expansion cannot terminate at an odd order term because that would cause the free energy to be unbound from below. Thus it must terminate at an even order

term. However, in many cases cubic or other odd order terms are not allowed by the symmetry of the system itself, say if some transformation leads to $\eta \rightarrow -\eta$. Nonetheless, when the cubic term is present continuous phase transition can possibly occur only at isolated points in the P-T diagram determined by the solution of the equations $A(P, T) = 0$ and $C(P, T) = 0$. In general, the cubic term causes discontinuity in the free energy minima and order parameter corresponding to free energy minima (η_0) across the transition, leading to first order transition. This behavior is illustrated in Figs. 2.1 and 2.2.

Going to quartic term, it must be positive at the transition and thereby in its neighborhood, i.e., $B(P_c, T_c) > 0$ so as to keep the free energy bounded from below. $B > 0$ is as such not guaranteed by symmetry and in case this is not true then we must include terms up to the next even order term whose coefficient is positive. It is worth mentioning here that inclusion of higher order terms in case $B < 0$, will lead to first order transition. Usually it is sufficient to go up to the quartic term.

We can Taylor expand the coefficients about T_c . Keeping terms up to the lowest allowed order and assuming constant pressure:

$$A(T) = a(T - T_c); \quad a > 0 \quad \text{and} \quad B(T) = B(T_c) = B. \quad (2.2)$$

Keeping the above discussion in mind, we can rewrite the free energy functional (ignoring odd order terms) as

$$\mathcal{F}(T, \eta) = \alpha\eta^2 + \frac{\beta}{2}\eta^4, \quad \alpha = \alpha'(T - T_c). \quad (2.3)$$

Equilibrium conditions are found by examining the extrema of the free energy functional. Above T_c , $\partial\mathcal{F}(P, T, \eta)/\partial\eta = 0$, has only one real solution $\eta = 0$ corresponding to minima in the high symmetry phase. Below T_c , there are three real solutions – a

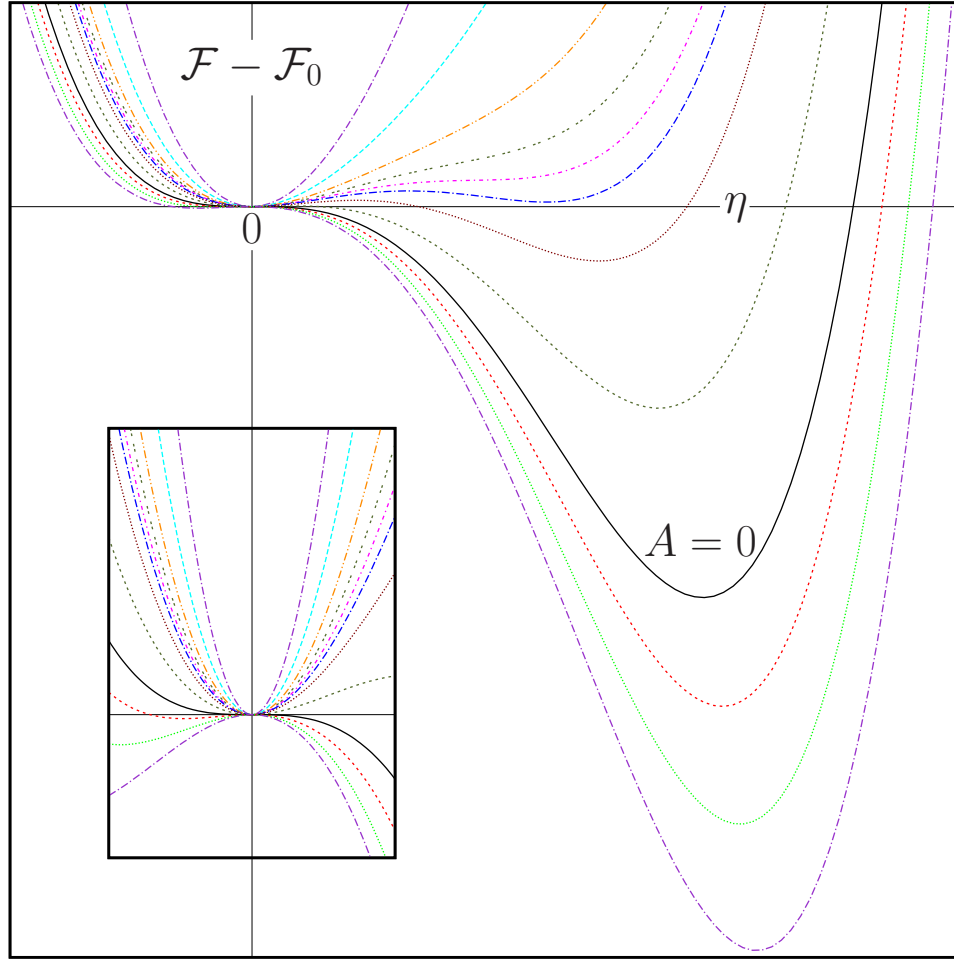


Figure 2.1: This figure explains how a first order transition occurs when the cubic term is present in Landau functional [Eq. (2.1 with $\alpha = 0$)]. Without any loss of generality coefficient of the cubic term is taken to be negative ($C < 0$). Black solid curve corresponds to $A = 0$ and the curves above and below that correspond to $A > 0$ and $A < 0$ respectively. For $A > (9/32)C^2/B$, there is only one minimum at $\eta = 0$. For $(9/32)C^2/B > A > C^2/4B$, there is a global minimum at $\eta = 0$, a local minimum at η_+ and a local maximum at η_- (here, $\eta_+ > 0$ and $\eta_- > 0$), for some +ve values of $\mathcal{F} - \mathcal{F}_0$. For $C^2/4B > A > 0$, there is a local minimum at $\eta = 0$, a global minimum at η_+ , and a local maximum at η_- (again $\eta_+ > 0$ and $\eta_- > 0$). For $A < 0$, there is a local maximum at $\eta = 0$, a global minimum at $\eta_+ > 0$, and a local minimum at $\eta_- < 0$. The global minimum at η_+ for $A > 0$ leads to metastable states while lowering the temperature because the second derivative at $\eta = 0$ (at local minimum) is still positive. The first two curves below the $\eta = 0$ line represent such metastable states. On increasing the temperature, from below T_c , again we encounter the metastable states (the first curve above zero line represents such states) until the local maximum at η_- becomes an inflexion point. In the metastable regime a first order transition, with a discontinuous jump in free energy minimum and corresponding value of order parameter from 0 to η_+ (decreasing temperature) or from η_+ to 0 (increasing temperature), is imminent, subject to system conditions. Here, $[\eta_{\pm} = -(3C/8B) \pm \sqrt{(3C/8B)^2 - (A/2B)}]$.

maximum at $\eta = 0$ and two minima at

$$\eta_{min} = \eta_0 = \pm \sqrt{-\frac{\alpha}{\beta}} = \pm \sqrt{-\frac{\alpha'(T - T_c)}{\beta}}. \quad (2.4)$$

This scaling, $\eta \propto \sqrt{(T - T_c)}$, is a characteristic of mean field theories.

2.2 Ginzburg Landau Functional

GL theory is masterpiece of physical intuition in which Ginzburg and Landau introduced a pseudowavefunction $\psi(\mathbf{r})$ as a complex order parameter with $|\psi(\mathbf{r})|^2$ representing the local density of superconducting electrons or superfluid $n_s(\mathbf{r})$, in analogy with Bose-Einstein condensation. Therefore,

$$|\psi|^2 = n_s(\mathbf{r}) \quad \text{and} \quad \int d^3r |\psi|^2 = N_s = n_s V. \quad (2.5)$$

The basic postulate of the GL theory extends upon the Landau theory to include spatial variations of the order parameter in the presence of a magnetic field. The GL free energy functional, therefore can be expanded in a series of the form

$$f[T, \psi, \mathbf{A}] = f_0 + \alpha |\psi|^2 + \frac{\beta}{2} |\psi|^4 + \frac{1}{2m^*} \left| \left(-i\hbar \nabla - \frac{e^*}{c} \mathbf{A} \right) \psi \right|^2 + \frac{B^2}{8\pi}, \quad (2.6)$$

where $\alpha = \alpha'(T - T_c)$. The last term in the expansion accounts for the energy due to magnetic field. Here, e^* and m^* are the charge and the mass respectively, of a superconducting charge carrier (Cooper pair).

2.2.1 Absence of fields and gradients

This condition arises when a superconductor is cooled below T_c in zero field or in the bulk of a type I superconductor in an applied field. In both these cases, fields

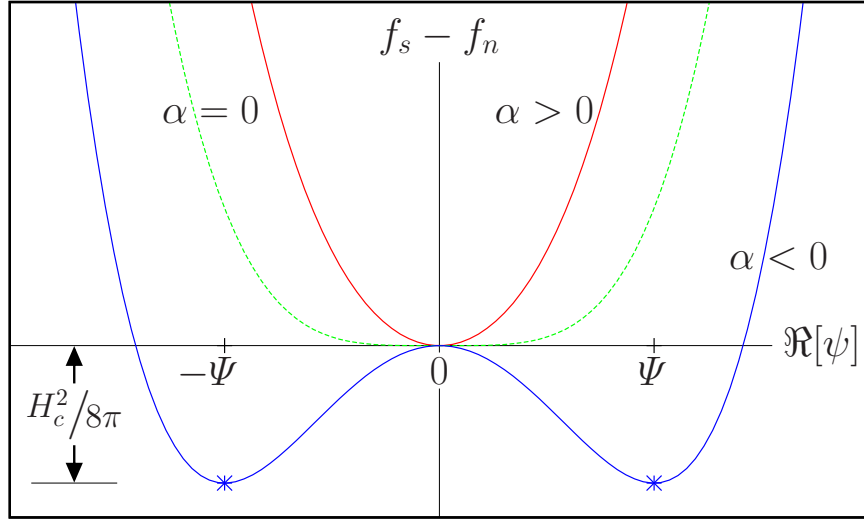


Figure 2.3: GL free energy versus order parameter. Only the real axis for the order parameter is shown. Including the imaginary part will lead to a circle of minima, in the complex plane, for $T < T_c$.

and gradients are absent below T_c . Therefore the GL theory in this case is similar to Landau theory and the stability condition in superconducting state is

$$|\psi|_{\min}^2 = \Psi^2 = -\frac{\alpha}{\beta}. \quad (2.7)$$

The difference is that in GL theory the order parameter is complex, $\psi = |\psi|e^{i\phi}$. Therefore, instead of two degenerate solutions, we actually have a continuous set of degenerate solutions. This can be visualized by rotating Fig. 2.3 about the vertical axis, which for $T < T_c$ yields a circle of minima in the complex plane. Due to the resulting shape, the solution is called ‘Mexican hat’ or ‘wine bottle’ potential. However, the superconducting state with $\psi = \Psi e^{i\phi} = (-\alpha/\beta)^{1/2} e^{i\phi}$ is realized with some fixed value of the phase ϕ . This state clearly is not invariant under the rotations of the phase factor. Hence, we say that the *global* $U(1)$ gauge symmetry is spontaneously broken because even though the free energy density f possess gauge symmetry $U(1)$, the equilibrium state below T_c (superconducting state) does not. In short, normal state lacks phase coherence whereas the superconducting state is phase coherent.

In the case of zero applied field, below transition point ($T < T_c$),

$$f_n - f_s = \frac{\alpha^2}{\beta} - \frac{\alpha^2}{2\beta} = \frac{\alpha^2}{2\beta}. \quad (2.8)$$

This must be equal to the condensation energy Eq. (1.1). Hence,

$$H_c(T) = \sqrt{4\pi \frac{\alpha^2}{\beta}}. \quad (2.9)$$

Same relation can be obtained for type I superconductors in a applied field. However, when \mathbf{H} field is held constant rather than \mathbf{B} field, the appropriate thermodynamic free energy to consider is Gibbs free energy. The two are related by

$$G = F - \int d^3r \frac{\mathbf{B} \cdot \mathbf{H}}{4\pi} \quad (2.10)$$

Again, in the normal state $B = H$ and in the superconducting state both magnetic induction \mathbf{B} and vector potential \mathbf{A} (in the London gauge) vanish. Therefore

$$g_n - g_s = -\frac{H^2}{8\pi} + \frac{\alpha^2}{2\beta}. \quad (2.11)$$

Now, the system will be superconducting only when g_s is smaller than g_n , i.e., $g_n - g_s > 0$. Again the critical field above which superconductivity is destroyed, given by $H = H_c$, turns out to be the same as given by Eq. (2.9).

Entropy

$$S = S_0 - \frac{\partial \alpha}{\partial T} |\psi|^2. \quad (2.12)$$

In normal phase, $\eta = 0$ and $S = S_0$; in superconducting phase,

$$S = S_0 + \frac{(\alpha')^2}{\beta} (T - T_c). \quad (2.13)$$

Thus, at $\Delta S|_{T_c} = 0$, i.e., entropy is continuous at transition temperature.

Specific heat

$$\Delta c_p|_{T_c} = T \left. \frac{\partial \Delta S}{\partial T} \right|_{T_c} = \frac{(\alpha')^2}{\beta} T_c. \quad (2.14)$$

Therefore, specific heat shows a discontinuity at transition temperature as expected in a second order transition. However, this theory results in a simple jump discontinuity in specific heat at T_c whereas in reality most second order transitions show a discontinuity divergent from both sides of T_c , a behavior known as ‘ λ ’ anomaly. The correct behavior can be obtained in a more complex theory that includes fluctuations.

2.2.2 Fields and gradients

To consider the effect of fields and gradients, we write

$$\psi(\mathbf{r}) = |\psi(\mathbf{r})| e^{i\phi} = \Psi f(\mathbf{r}) e^{i\phi(\mathbf{r})} \quad (2.15)$$

where in the last form spatial variation is included in the function $f(\mathbf{r})$ that can take the values between 0–1.

Now, the fourth term in Eq. (2.6) can be written as

$$\frac{1}{2m^*} \left[\hbar^2 (\nabla |\psi|)^2 + \left(\hbar \nabla \phi - \frac{e^* A}{c} \right)^2 |\psi|^2 \right]. \quad (2.16)$$

The first term in Eq. (2.16) accounts for the energy associated with spatial variations in the magnitude of the order parameter and the second term represents kinetic energy density associated with supercurrents. In the London gauge ϕ is constant so $\nabla \phi = 0$. In this limit, comparing the kinetic energy term in Eq. (2.16) to the kinetic energy density of a London superconductor, namely $A^2/8\pi\lambda_{\text{eff}}^2$ [11], and considering

that $|\psi|^2 = n_s^*$, we obtain the

$$\lambda_{\text{eff}}^2 = \frac{m^* c^2}{4\pi |\psi|^2 e^{*2}}, \quad (2.17)$$

where λ_{eff} is the *effective penetration depth*. This agrees with the usual definition of the London penetration depth Eq. (1.3). Experiments led to conclude that in BCS superconductors, $m^* = 2m_e$ and $e^* = 2e$, as expected for a Cooper pair. Hence [11],

$$\Psi^2 \equiv n_s^* = \frac{n_s}{2} = \frac{mc^2}{8\pi e^2 \lambda_{\text{eff}}^2}, \quad (2.18)$$

$$\alpha(T) = -\frac{2e^2}{mc^2} H_c^2(T) \lambda_{\text{eff}}^2(T), \quad (2.19)$$

$$\beta(T) = \frac{16\pi e^4}{m^2 c^4} H_c^2(T) \lambda_{\text{eff}}^4(T). \quad (2.20)$$

2.3 Ginzburg-Landau Equations

In the absence of fields and gradients, GL functional is minimized by requiring $|\psi| = \Psi = \sqrt{-\alpha/\beta}$, as seen previously. In the presence of fields and gradients, $\psi(\mathbf{r})$ adjust itself to minimize the functional. We can do this by applying variational approach. Consider

$$F[T, \psi^*, \mathbf{A}] = \int d^3r f[T, \psi^*, \mathbf{A}]. \quad (2.21)$$

To minimize it w.r.t. ψ^* , we write

$$\delta F = F[\psi^* + \delta\psi^*] - F[\psi^*] = 0. \quad (2.22)$$

This leads to the equation

$$\delta F = \int d^3r \left[\alpha\psi + \beta|\psi|^2\psi + \frac{1}{2m^*} \left(\frac{\hbar}{i} \nabla - \frac{e^* \mathbf{A}}{c} \right)^2 \psi \right] \delta\psi^* = 0. \quad (2.23)$$

Since $\delta\psi^*$ is arbitrary, the equation is satisfied only if the factor in the square brackets is zero. This gives us 1st Ginzburg-Landau differential equation.

$$\alpha\psi + \beta|\psi|^2\psi + \frac{1}{2m^*} \left(\frac{\hbar}{i} \nabla - \frac{e^* \mathbf{A}}{c} \right)^2 \psi = 0. \quad (2.24)$$

Similarly, we can minimize the functional w.r.t. vector potential \mathbf{A}

$$\begin{aligned} \delta F &= \int d^3r \left\{ \frac{1}{2m^*} \left[\left| \left(\frac{\hbar}{i} \nabla - \frac{e^* (\mathbf{A} + \delta \mathbf{A})}{c} \right) \psi \right|^2 - \left| \left(\frac{\hbar}{i} \nabla - \frac{e^* \mathbf{A}}{c} \right) \psi \right|^2 \right] \right. \\ &\quad \left. + \frac{1}{8\pi} [(\nabla \times (\mathbf{A} + \delta \mathbf{A}))^2 - (\nabla \times \mathbf{A})^2] \right\} \\ &= \int d^3r \left[\frac{e^* \hbar}{i 2m^* c} (\psi \nabla \psi^* - \psi^* \nabla \psi) + \frac{e^{*2}}{m^* c^2} \psi^* \psi \mathbf{A} + \frac{1}{c} \mathbf{J} \right] \delta \mathbf{A}. \end{aligned} \quad (2.25)$$

This leads to 2nd Ginzburg-Landau differential equation

$$\mathbf{J}(\mathbf{r}) = \frac{e^* \hbar}{i 2m^* c} (\psi^* \nabla \psi - \psi \nabla \psi^*) + \frac{e^{*2}}{m^* c^2} \psi^* \psi \mathbf{A}, \quad (2.26)$$

where $\mathbf{J}(\mathbf{r})$ is current density.

Absence of the fields implies $\mathbf{A} = 0$. In this case Eq. (2.24) involves only real coefficients, therefore we can take ψ to be real. Let, $\psi = f(\mathbf{r})\Psi$, where $f(\mathbf{r})$ is dimensionless. Then Eq. (2.24), in one dimension, becomes

$$\frac{\hbar^2}{2m^* |\alpha|} \frac{\partial^2 f}{\partial x^2} + f - f^3 = 0. \quad (2.27)$$

It is evident from Eq. (2.27) that there exists a characteristic length called coherence length $\xi(T)$, associated with the variation of ψ . It is equal to the square root of the coefficient of second order term in Eq. (2.27), i.e.,

$$\xi(T) = \sqrt{\frac{\hbar^2}{2m^* |\alpha(T)|}} \propto \sqrt{\frac{1}{T_c - T}} \quad (2.28)$$

This coherence length decreases with decreasing temperature and it diverges at T_c . Physically, coherence length $\xi(T)$ signifies the distance over which a small disturbance of ψ , from Ψ , dies out. In other words, it is the distance over which ψ varies. Using Eqs. (2.18), (2.19), (2.20), and (2.28), we can define the so called Ginzburg-Landau parameter κ

$$\kappa = \frac{\lambda_{\text{eff}}(T)}{\xi(T)} = \frac{2\sqrt{2}\pi H_c(T)\lambda_{\text{eff}}^2(T)}{\Phi_0} \quad (2.29)$$

where $\Phi_0 = \frac{hc}{2|e|}$ is the fluxoid quantum.

2.4 Type I and Type II Superconductors

The critical value $\kappa = 1/\sqrt{2}$ divides superconductors into two classes.

$$\kappa = \begin{cases} < \frac{1}{\sqrt{2}} & \text{Type I superconductors} \\ > \frac{1}{\sqrt{2}} & \text{Type II superconductors} \end{cases} \quad (2.30)$$

Suppose a superconductor is cooled below its T_c in a very high magnetic field so that the flux passes through it and it is no longer superconducting. Now, consider lowering the magnetic field slowly. The two classes of superconductors behave differently in such a situation. In a type I superconductor, depending upon the demagnetization factor of the geometry of the sample, either the flux is completely expelled below a certain field value (if demagnetization factor is zero) or the sample first divides into several normal and superconducting regions and the applied flux passes through the normal regions (if the demagnetization factor is non-zero) and then on further decreasing the field, the Meissner state appears. On the other hand, in type II superconductors, at a field much above H_c , the flux bearing (normal) regions subdivide until a quantum limit is reached such that each quantum of flux passes through the sample as a distinct flux tube [11]. This state is called mixed phase or Shubnikov

phase. This is unlike the case for type I superconductors, where the intermediate state occurs over a small range of magnetic field and there is no such quantization of flux. The Shubnikov phase occurs over a large range of magnetic field even if the demagnetization factor is zero. This distinction was predicted by A. A. Abrikosov [87] before the discovery of type II superconductivity. The primary reason for this difference between type I and type II superconductors is the *surface energy*. In type II superconductors the surface energy at the normal and superconducting interface is negative, therefore type II superconductors tend to maximize the surface area to minimize the free energy [88].

This separation of materials into two classes can also be seen in the Eq. (2.31) which relates the highest field H_{c2} at which superconductivity can nucleate in the bulk of a material to the thermodynamic critical field H_c [11]. When the nucleation begins $|\psi|^2 \ll \Psi^2$, therefore we can neglect the β term in Eq. (2.24). This leads to a linearized equation, which is much easier to solve with a proper gauge choice, say, $A_y = Hx$. The solution for H_{c2} is given by

$$H_{c2} = \frac{\Phi_0}{2\pi\xi^2} = \frac{4\pi\lambda^2 H_c^2}{\Phi_0} = \sqrt{2}\kappa H_c. \quad (2.31)$$

Equation (2.31) reveals that for type I superconductors $H_{c2} < H_c$ and for type II superconductors $H_{c2} > H_c$. This implies that type I superconductors ‘supercool’ below H_c remaining normal, ideally until H_{c2} is reached. Near H_{c2} nucleation occurs followed by a discontinuous jump in $|\psi|^2$ to Ψ^2 . And if the field is increased again, the material remain superconducting until H_c is reached where again the $|\psi|$ drops to zero discontinuously. Thus superconducting transition in type I superconductors is irreversible and it shows hysteresis. In contrast to this, in type II materials $|\psi|^2$ increases continuously from 0 at H_{c2} becoming superconducting much above H_c in a second order phase transition. These features are visible in Fig. 2.4.

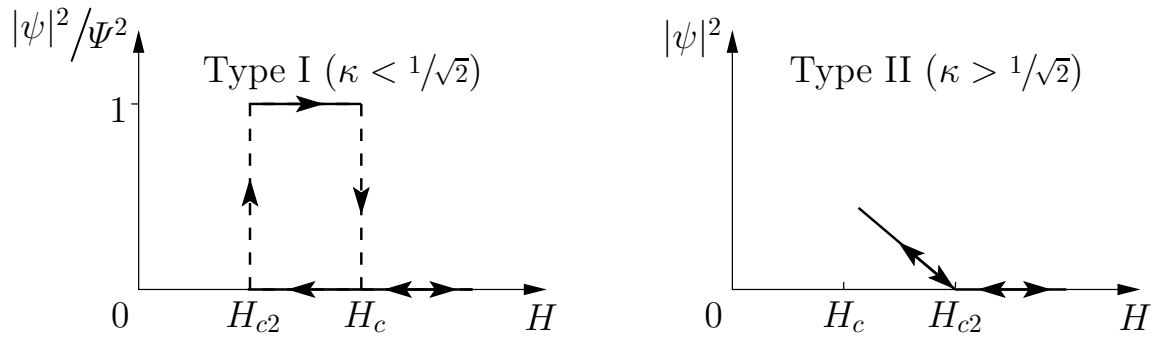


Figure 2.4: Behavior of the order parameter at nucleation field H_{c2} . In type I superconductors, nucleation field H_{c2} smaller than the thermodynamic critical field H_c and magnitude of the order parameter jumps discontinuously and irreversibly to its maximum value. In type II superconductors, nucleation occurs above the thermodynamic critical field and the magnitude of the order parameter increases continuously and reversibly.

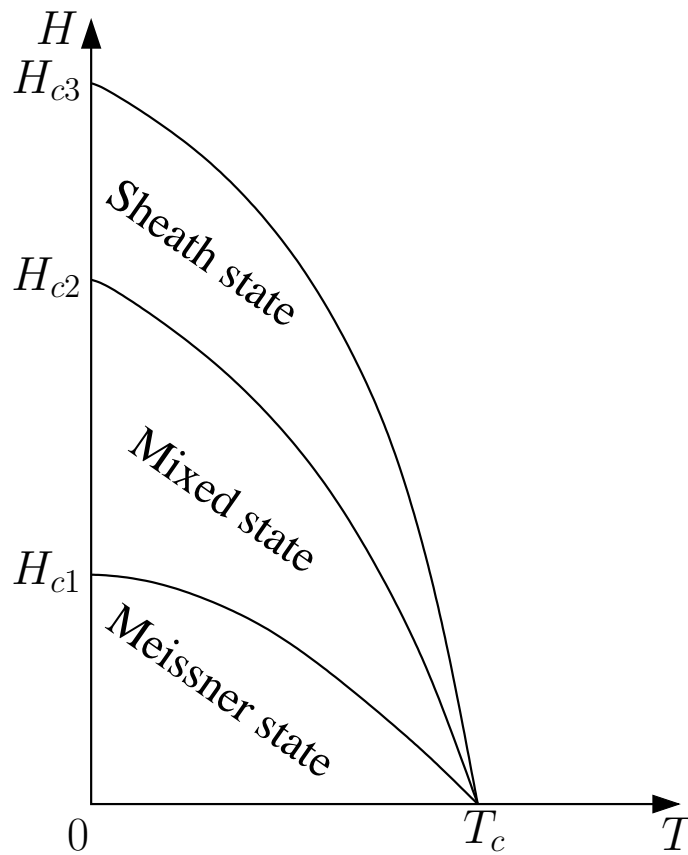


Figure 2.5: Temperature dependence of the critical field in type II superconductors.

Temperature dependence of the critical fields in a type II superconductor is shown in Fig. 2.5. Below H_{c1} , flux is completely expelled out of the superconductor. Between H_{c1} and H_{c2} mixed phase occurs and between H_{c2} and H_{c3} only surface superconductivity occurs in a sheath of thickness $\sim \xi(T)$. Nucleation of superconductivity at the surface begin at H_{c3} . At a metal-insulator interface, $H_{c3} = H_{c2}$ for H normal to the surface and $H_{c3} = 1.695H_{c2}$ for H parallel to the surface [89].

2.5 Single-vortex solution

Since the major emphasis in Chapter 3 is vortices in s-wave noncentrosymmetric superconductors, it is worth looking here at single vortex solution in the superconductors with inversion symmetry. This requires the solution of the GL differential equations [Eqs. (2.24) and (2.26)]. Symmetry of the problem suggests to work in cylindrical coordinates. Let us define, $\psi = \Psi f(r)e^{-i\phi}$ and choose the gauge for \mathbf{A} so that

$$\mathbf{A} = A(r)\hat{\phi} \quad \text{with} \quad A(r) = \frac{1}{r} \int_0^r r' B(r') dr'. \quad (2.32)$$

Near the center of the vortex, $B(r) \approx B(0)$, where $B(0)$ is the cutoff, therefore

$$A(r) = \frac{B(0)r}{2}, \quad r \rightarrow 0, \quad (2.33)$$

and far away from the center $\oint \mathbf{A} \cdot d\mathbf{l} = 2\pi r A_\infty = \Phi_0$, because total flux in a vortex is Φ_0 . Hence

$$A(r) = \frac{\Phi_0}{2\pi r}, \quad r \rightarrow \infty. \quad (2.34)$$

This satisfies the condition that $B(0) = 0$ at $r = \infty$.

Substituting the above definition of ψ in the GL Eqs. (2.24) and (2.26), we get

$$f - f^3 - \xi^2 \left[\left(\frac{1}{r} - \frac{2\pi A}{\Phi_0} \right)^2 f - \frac{1}{r} \frac{d}{dr} \left(r \frac{df}{dr} \right) \right] \quad (2.35)$$

$$\text{and} \quad \mathbf{J} = -\frac{e^*\hbar}{m^*}\Psi^2 f^2 \left(\frac{1}{r} - \frac{2\pi A}{\Phi_0} \right) \hat{\phi}. \quad (2.36)$$

The problem involves coupled nonlinear differential equations which require to be solved numerically. Nonetheless, we can look at the asymptotic solution analytically. Let us expand the $f(r)$ in a power series

$$f(r) = \sum_{k=0}^{\infty} c_k r^{n+k} \quad (2.37)$$

It is sufficient to substitute first few terms of the series in Eq. (2.35) to find the solution for small r . It turns out that the expansion contains only odd power terms and $f(r)$ is linear in the small r limit. Moreover, $f(r)$ must saturate to 1 in the large r limit. Therefore, a reasonable approximation over the entire range would be a hyperbolic function [†]

$$f \approx \tanh\left(\frac{\nu r}{\xi}\right) \quad (2.38)$$

where ν is constant ~ 1 .

In the large κ limit, the solution for B outside the core region of radius $\sim \xi$ can be obtained by substituting $f = 1$ in Eq. (2.36), because f rises to its maximum value (unity) in a distance $\sim \xi$. Therefore,

$$\nabla \times \nabla \times \left(\frac{c}{4\pi} \mathbf{B} \right) = \nabla \times \mathbf{J} = \frac{\Phi_0 c}{8\pi^2 \lambda^2} \left[\nabla \times (\nabla \phi) - \frac{2\pi}{\Phi_0} B(r) \hat{z} \right]. \quad (2.39)$$

Now,

$$\int [\nabla \times (\nabla \phi)] \cdot d\mathbf{a} = \oint \nabla \phi \cdot d\mathbf{l} = \oint \frac{1}{r} r d\phi = 2\pi \quad (2.40)$$

$$\Rightarrow \quad \nabla \times (\nabla \phi) = 2\pi \delta^2(r) \hat{z}, \quad (2.41)$$

[†] $\tanh(x) = x - \frac{x^3}{3} + \frac{2x^5}{15} - \frac{17x^7}{315} + \dots = \sum_{n=1}^{\infty} \frac{2^{2n}(2^{2n}-1)B_{2n}x^{2n-1}}{(2n)!}, |x| < \frac{\pi}{2}$, where B_n is n^{th} Bernoulli number

where $\delta^2(r)$ is a two dimensional delta function such that

$$1 = \int \delta^2(r) \hat{z} \cdot d\mathbf{a} = \int \delta^2(r) r dr d\phi = 2\pi \int \delta^2(r) r dr. \quad (2.42)$$

Hence,

$$\delta^2(r) = \frac{\delta(r)}{2\pi r}. \quad (2.43)$$

Thus, from Eq. (2.39), we can write

$$\nabla^2 B(r) - \frac{B(r)}{\lambda^2} = -\frac{\Phi_0}{\lambda^2} \hat{z} \quad (2.44)$$

This equation has an exact solution

$$B(r) = \frac{\Phi_0}{2\pi\lambda^2} K_0\left(\frac{r}{\lambda}\right), \quad (2.45)$$

where K_0 is a modified Bessel function. K_0 and thereby $B(r)$ decreases exponentially in the large r limit, so that $B(r) \rightarrow 0$ as $r \rightarrow \infty$ satisfying the physical requirement. On the hand, $B(r)$ shows a logarithmic divergence $\ln(\lambda/r)$ as $r \rightarrow 0$. However, this divergence is cutoff inside the core where $f(r)$ goes to zero at $r = 0$.

2.6 Lifshitz Invariants

In the GL functional defined by Eq. (2.2), only second order terms in gradients are included. This restriction is imposed by the inversion symmetry of the crystal lattice. However if, inversion symmetry is absent in the point group of the lattice, as is the case for NCS superconductors, it is allowed to include a term linear in gradient of the order parameter coupled with the magnetic flux density and multiplied by the complex conjugate of the order parameter to preserve the $U(1)$ gauge symmetry, plus its complex conjugate. Such terms are called Lifshitz invariant (LI). The most general

form of Lifshitz invariants is [15]

$$K_{ij}B_i[\psi^*(D_j\psi) + \psi(D_j\psi)^*], \quad (2.46)$$

where $D_i = -i\nabla_i - 2eA_i$ ($\hbar = e = m_e = 1$) and K_{ij} is the coupling constant. Under inversion \mathcal{I} , \mathbf{B} remains invariant but \mathbf{D} changes sign and therefore such a term is not allowed in materials whose point group contains inversion symmetry. On the other hand, the term is invariant under Time reversal \mathcal{T} because \mathbf{B} changes sign and $\mathbf{D}\psi$ goes to $-(\mathbf{D}\psi)^*$, under it.

The detailed form of Lifshitz invariant is point group specific. A list of allowed Lifshitz invariants corresponding to A_1 (identity) representation for different point groups is given in Ref. [15]. In the Section 2.6.1, Lifshitz invariants for all the 1-D representations of C_{4v} group are found. It is comparatively easier to determine Lifshitz invariants for 1-D representations because higher dimensional representation would require to deal with multidimensional order parameters.

2.6.1 Lifshitz invariants for C_{4v} group

Here, we will find Lifshitz invariants corresponding to all the 1-D representations of C_{4v} group. Elements of group C_{4v} are $(E, C_2, C_4, C'_4, \sigma_v, \sigma'_v, \sigma_d, \sigma'_d)$. Defining $j_i = \psi^*(\mathbf{D}_i\psi) + \psi(\mathbf{D}_i\psi)^*$ such that j_i transform under rotations like D_i . Moreover, \mathbf{B} being an axial vector transforms under proper rotation like ordinary (polar) vectors but behaves differently under improper rotations like reflections. Under reflection, an axial vector is reflected (like polar vectors) and reversed. Under the elements of C_{4v} , terms mixing $x - z$ and $y - z$ components, i.e., the terms $B_x j_z$, $B_y j_z$, $B_z j_x$, and $B_z j_y$ are not allowed because these transform differently under the elements of the same class, for e.g.,

$$B_x j_z \xrightarrow{C_4} B_y j_z \quad B_x j_z \xrightarrow{C'_4} -B_y j_z \quad (2.47)$$

Table 2.1 is the character table for point group C_{4v} . The last column gives the Lifshitz invariants corresponding to each 1-D representation.

Table 2.1: Character table for group C_{4v} with Lifshitz invariants for 1-D representations.

C_{4v} ($4mm$)		E	C_2	$2C_4$	$2\sigma_v$	$2\sigma_d$	Lifshitz Invariants
$x^2 + y^2, z^2$	z	A_1	1	1	1	1	$K(B_x j_y - B_y j_x)$
	R_z	A_2	1	1	1	-1	$K_1(B_x j_x + B_y j_y) + K_2 B_z j_z$
$x^2 - y^2$		B_1	1	1	-1	1	$K(B_x j_y + B_y j_x)$
xy		B_2	1	1	-1	-1	$K(B_x j_x - B_y j_y)$
(xz, yz)	(x, y) (R_x, R_y)	E	2	-2	0	0	

Chapter 3

Vortices in Cubic Noncentrosymmetric Superconductors

3.1 Introduction

In this chapter, we will examine Ginzburg-Landau (GL) theory for *s*-wave cubic superconductors with an emphasis on the vortex structure. The magnetoelectric effects (ME) play an important role here. This has previously been studied with a London theory. The London theory predicts a supercurrent that flows parallel to the applied magnetic field and further indicates that this current diverges in the the vortex core [90, 91]. GL theory is needed to understand the vortex core structure properly. In the following, we use GL theory first to derive single vortex solution in the London limit (finding results that agree with previous results [Ref. [90, 91]]), then to numerically examine the full single vortex structure. Finally, we find the high density vortex lattice solution near the upper critical field H_{c2} and discuss how it differs from single vortex solution.

3.2 Ginzburg Landau Free Energy

For point group symmetry O , the GL free energy is ($\hbar = c = m_e = 1$) [15]:

$$F = \int d^3r \left\{ \alpha |\eta|^2 + K \eta^* \mathbf{D}^2 \eta + \epsilon \mathbf{B} \cdot [\eta^* (\mathbf{D}\eta) + \eta (\mathbf{D}\eta)^*] + \frac{\beta}{2} |\eta|^4 + \frac{B^2}{8\pi} \right\}, \quad (3.1)$$

where $\alpha = \alpha_0(T - T_c)$, $D_i = -i\nabla_i - 2eA_i$ and $\mathbf{B} = \nabla \times \mathbf{A}$. An important feature of Eq. (3.1) is the existence of the Lifshitz invariant denoted by the parameter ϵ . Such Lifshitz invariants [24, 28, 31, 92, 93, 94] give rise to FFLO-like phases [28, 31, 32, 95, 96], magnetoelectric properties [24, 34, 35, 36, 90, 91] of NCS, and play a central role in the vortex physics examined here.

Eq. (3.1) leads to the following GL equations:

$$\alpha \eta + \beta |\eta|^2 \eta + K \mathbf{D}^2 \eta - 2\epsilon (\nabla \times \mathbf{A}) \cdot (i\nabla \eta + 2e\mathbf{A}\eta) = 0 \quad (3.2)$$

$$\text{and } \mathbf{J} = \frac{1}{4\pi} [\nabla \times (\mathbf{B} - 4\pi\mathbf{M})] = 2eK [\eta^* (\mathbf{D}\eta) + \eta (\mathbf{D}\eta)^*] + 4e\epsilon |\eta|^2 \mathbf{B}, \quad (3.3)$$

$$\text{where } \mathbf{M} = -\epsilon [\eta^* (\mathbf{D}\eta) + \eta (\mathbf{D}\eta)^*] = - \left(\frac{\partial F}{\partial \mathbf{B}} \right)_T. \quad (3.4)$$

These equations are joined by the boundary conditions (which follow from the surface terms that arise from integration by parts in the variation of F):

$$[K \hat{n}_i (D_i \eta) + \epsilon B_i \hat{n}_i \eta]_{\text{boundary}} = 0, \quad (3.5)$$

where \hat{n}_j is the component of surface normal along \hat{j} , and the usual Maxwell boundary conditions on the continuity of the normal component of \mathbf{B} and the transverse components of $\mathbf{H} = \mathbf{B} - 4\pi\mathbf{M}$.

3.3 Single-vortex structure

Here we examine the single vortex structure within London theory and numerically. We make two approximations, the first is we assume that the Lifshitz invariant can be treated as a perturbation to the GL free energy and the second assumes that we are in the large $\kappa = \lambda/\xi$ limit. Both these approximations are reasonable for $\text{Li}_2\text{Pt}_3\text{B}$ [91] and $\text{Mo}_3\text{Al}_2\text{C}$ [45, 46].

As seen earlier, the symmetry of the single vortex solution suggest use of cylindrical coordinate system. In cylindrical coordinates, let $\eta = \Psi f(r)e^{i\chi}$ where $\chi = \mp\phi$ (upper sign for negative winding and lower sign for positive winding); $K = \frac{1}{4}$, $\xi^2 = -\frac{1}{4\alpha}$; $\Psi^2 = -\frac{\alpha}{\beta} = \frac{1}{8\pi e^2 \lambda^2}$; $\Phi_o = -\frac{\pi}{e} = \frac{\pi}{|e|}$; $\mu = \frac{4\epsilon}{e\xi} = \frac{4\sigma}{\xi}$ and scale the various physical quantities as: $r \rightarrow \lambda x$, $\mathbf{A} \rightarrow \pm \frac{\Phi_o}{2\pi\xi} \mathbf{A} = \mp 2\xi e \mathbf{A}$, $\mathbf{B} \rightarrow \pm \frac{\Phi_o}{2\pi\xi\lambda} \mathbf{B}$ and $\mathbf{J} \rightarrow \pm \frac{\Phi_o}{2\pi\xi\lambda^2} \mathbf{J}$.

Using $\nabla \times \nabla\phi = 2\pi\delta^2(r)\hat{\mathbf{z}}$ where $\delta^2(r) = \frac{\delta(r)}{2\pi r}$, the GL Eqs. (3.2) and (3.3) transform to the dimensionless form as:

$$\begin{aligned} \frac{d^2 f}{dx^2} + \frac{1}{x} \frac{df}{dx} - \kappa^2 \left(\frac{1}{\kappa x} - A_\phi \right)^2 f + \kappa^2 (f - f^3) - \kappa^2 A_z^2 f \\ + \mu \frac{dA_z}{dx} \left(\frac{1}{x} - \kappa A_\phi \right) f + \kappa \mu A_z \left(\frac{A_\phi}{x} + \frac{dA_\phi}{dx} \right) f = 0, \end{aligned} \quad (3.6)$$

$$\frac{d^2 A_\phi}{dx^2} + \frac{1}{x} \frac{dA_\phi}{dx} - \frac{A_\phi}{x^2} - \left(A_\phi - \frac{1}{\kappa x} \right) f^2 - \frac{\mu}{\kappa} A_z f \frac{df}{dx} - \frac{\mu}{\kappa} f^2 \frac{dA_z}{dx} = 0, \quad (3.7)$$

$$\begin{aligned} \frac{d^2 A_z}{dx^2} + \frac{1}{x} \frac{dA_z}{dx} - f^2 A_z - \frac{\mu}{\kappa} f \left(\frac{1}{\kappa x} - A_\phi \right) \frac{df}{dx} + \frac{\mu}{\kappa x} f^2 A_\phi \\ + \frac{\mu}{\kappa} f^2 \frac{dA_\phi}{dx} - \frac{\mu\pi}{\kappa^2} f^2 \delta^2(x) = 0. \end{aligned} \quad (3.8)$$

We assume μ to be a small parameter which implies that A_z is also small. To first

order in μ and/or A_z :

$$\frac{d^2 f}{dx^2} + \frac{1}{x} \frac{df}{dx} - \kappa^2 \left(\frac{1}{\kappa x} - A_\phi \right)^2 f + \kappa^2 (f - f^3) = 0, \quad (3.9)$$

$$\frac{d^2 A_\phi}{dx^2} + \frac{1}{x} \frac{dA_\phi}{dx} - \frac{A_\phi}{x^2} - \left(A_\phi - \frac{1}{\kappa x} \right) f^2 = 0, \quad (3.10)$$

$$\begin{aligned} \frac{d^2 A_z}{dx^2} + \frac{1}{x} \frac{dA_z}{dx} - f^2 A_z - \frac{\mu}{\kappa} f \left(\frac{1}{\kappa x} - A_\phi \right) \frac{df}{dx} + \frac{\mu}{\kappa x} f^2 A_\phi \\ + \frac{\mu}{\kappa} f^2 \frac{dA_\phi}{dx} - \frac{\mu\pi}{\kappa^2} f^2 \delta^2(x) = 0. \end{aligned} \quad (3.11)$$

Eqs. (3.9) and (3.10) are usual GL equations, whereas Eq. (3.11) arise due to Lifshitz invariant in the free energy. In the large κ limit the usual GL equations simplify. Typically, f varies on distances $x \sim 1/\kappa$ [87, 11]. When $\kappa \gg 1$, f only varies for small x where the superfluid velocity $Q = |\frac{1}{\kappa x} - A_\phi|$ varies as $\frac{1}{\kappa x}$ (for small x , $A_\phi \sim x$). Thus, the usual GL equations can be approximated as:

$$\frac{d^2 f}{dx^2} + \frac{1}{x} \frac{df}{dx} - \frac{1}{x^2} f + \kappa^2 (f - f^3) = 0, \quad (3.12)$$

$$\frac{d^2 A_\phi}{dx^2} + \frac{1}{x} \frac{dA_\phi}{dx} - \frac{A_\phi}{x^2} - \left(A_\phi - \frac{1}{\kappa x} \right) f^2 = 0. \quad (3.13)$$

3.3.1 London limit

In the London limit: $f = 1$ and $\frac{df}{dx} = 0$. Also, $B_z = B_{oz}(x) = \frac{1}{\kappa} K_0(x)$, where $K_0(x)$ is modified Bessel function of first kind. Therefore, Eq. (3.11) reduces to

$$\nabla^2 A_z - k A_z = -\frac{\mu}{\kappa^2} K_0(x) + \frac{\mu\pi}{\kappa^2} \delta^2(x). \quad (\text{here, } k = 1). \quad (3.14)$$

The operator on the left hand side is the modified Helmholtz operator with Green's function: $G(x, x') = \frac{1}{2\pi} K_0(|\mathbf{x} - \mathbf{x}'|)$. In cylindrical coordinates [97]:

$$\begin{aligned} K_0(k|\mathbf{x} - \mathbf{x}'|) &= K_0(k\sqrt{x^2 - x'^2 - 2xx'\cos(\phi - \phi')}) \\ &= I_0(kx_<)K_0(kx_>) + 2\sum_{m=1}^{\infty} \cos[m(\phi - \phi')]I_m(kx_<)K_m(kx_>). \end{aligned} \quad (3.15)$$

Using this, we can find the solution for A_z . The solution involves an area integral in polar coordinates, but Eq. (3.14) lacks angular dependence and therefore the ϕ integral of the second term in Eq. (3.15) always yield zero. Hence, ignoring that term, the solution for A_z is

$$\begin{aligned} A_z(x) &= \frac{\mu}{\kappa^2} \left[K_0(x) \int_0^x x' I_0(x') K_0(x') dx' \right. \\ &\quad \left. + I_0(x) \int_x^\infty x' [K_0(x')]^2 dx' - \frac{1}{2} K_0(x) \right]. \end{aligned} \quad (3.16)$$

where, the last term is the contribution of the $\delta^2(x)$ -function source term in Eq. (3.14). Taking curl of A_z , we reproduce the result of Lu and Yip [Ref. [90, 91]] for transverse flux density *:

$$\begin{aligned} B_\phi(x) &= \frac{\mu}{\kappa^2} \left[K_1(x) \int_0^x x' I_0(x') K_0(x') dx' - I_1(x) \int_x^\infty x' [K_0(x')]^2 dx' - \frac{1}{2} K_1(x) \right] \\ &= \frac{\mu}{\kappa^2} \left[K_1(x) \int_0^x x' \left(\frac{I_1(x')}{x'} + I_1'(x') \right) K_0(x') dx' \right. \\ &\quad \left. - I_1(x) \int_x^\infty x' K_0(x') \left(-\frac{K_1(x')}{x'} - K_1'(x') \right) dx' - \frac{1}{2} K_1(x) \right] \\ &= \frac{\mu}{\kappa^2} \left[K_1(x) \int_0^x \cancel{I_1(x')} \cancel{K_0(x')} dx' + K_1(x) \left\{ x' K_0(x') I_1(x') \Big|_0^x \right. \right. \\ &\quad \left. \left. - \int_0^x [\cancel{K_0(x')} + x' K_0'(x')] I_1(x') dx' \right\} \right] \end{aligned}$$

*See Appendix A for justifying the intermediate steps to reach Eq. (3.17)

$$\begin{aligned}
& + I_1(x) \int_x^\infty \underline{K_0(x')K_1(x')} dx' + I_1(x) \left\{ x' K_0(x') K_1(x') \Big|_x^\infty \right. \\
& \quad \left. - \int_x^\infty [K_0(x') + x' K_0'(x')] K_1(x') dx' \right\} \\
& = \underline{x K_0(x) K_1(x) I_1(x)} + K_1(x) \int_0^x x' K_1(x') I_1(x') dx' \\
& \quad + I_1(x) [x' K_0(x') K_1(x') \Big|_{x'=\infty} - \underline{x K_0(x) K_1(x)}] \\
& \quad + I_1(x) \int_x^\infty x' [K_1(x')]^2 \\
& = \frac{\mu}{\kappa^2} \left[K_1(x) \int_0^x x' I_1(x') K_1(x') dx' + I_1(x) \int_x^\infty x' [K_1(x')]^2 dx' - \frac{1}{2} K_1(x) \right]. \quad (3.17)
\end{aligned}$$

The asymptotic behavior of transverse flux density is:

$$B_\phi \sim \begin{cases} -\frac{\mu}{2\kappa^2} \left[\frac{1}{x} + x \ln x - \frac{x}{2} \right], & x \rightarrow 0 \\ \frac{\mu}{\kappa^2} \sqrt{\frac{\pi x}{8}} e^{-x}, & x \rightarrow \infty \end{cases} \quad (3.18)$$

Furthermore, we find

$$\begin{aligned}
J_z(x) &= \frac{\mu}{4\pi\kappa^2} \left[-\frac{\kappa^2}{\mu} A_z(x) + \frac{1}{2} K_0(x) \right] \\
&= \frac{\mu}{4\pi\kappa^2} \left[K_0(x) - K_0(x) \int_0^x x' I_0(x') K_0(x') dx' - I_0(x) \int_x^\infty x' [K_0(x')]^2 dx' \right]. \quad (3.19)
\end{aligned}$$

The asymptotic behavior of current density J_z shows logarithmic divergence in the small x limit:

$$J_z(x) \sim \begin{cases} \frac{\mu}{4\pi\kappa^2} \ln \frac{1}{x}, & x \rightarrow 0 \\ -\frac{\mu}{4\pi\kappa^2} \sqrt{\frac{\pi x}{8}} e^{-x}, & x \rightarrow \infty \end{cases} \quad (3.20)$$

In the limit $x \rightarrow 0$, the $\frac{1}{x}$ divergence in the azimuthal component of magnetization M_ϕ [see Eq. (3.23)] in the London limit ($f = 1$) is canceled by the $\frac{1}{x}$ divergence in the transverse flux density B_ϕ , but the logarithmic divergence in B_ϕ still shows up

in current density J_z . This is evident in the numerical solution as shown in Fig. 3.6. These divergences are an artifact of the London theory and the next section presents a numerical solution in which these divergences are no longer present. Also, we have numerical solved London limit solutions to the problem i.e. Eqs. (3.16), (3.17), and (3.19), using Fortran 90 (Visual Fortran software). The numerical code is provided in section B.1.

3.3.2 Numerical solution

We use the finite difference (relaxation) method [98] for full solution of the GL equations [Eqs. (3.12), (3.13) and (3.11)]. The relevant code is provided in section B.2. It is worthwhile to note that the $\delta^2(x)$ -source term in the Eq. (3.11) does not contribute to the full solution. To see this, we work out the solution corresponding to that term.

Part of the solution corresponding to $\delta^2(x)$ -function source term in Eq. (3.11)

$$= -\frac{\mu}{2\kappa^2} \left[K_0(xf(x)) \int_0^x f^2(x')\delta(x')I_0(x'f(x'))dx' + I_0(xf(x)) \int_{x \neq 0}^{\infty} f^2(x')\delta(x')K_0(x'f(x'))dx' \right]. \quad (3.21)$$

The second term in Eq. (3.21) is zero on account of the delta function, irrespective of the value of x , as long as it is non-zero. In the small- x limit, the $f(x') = c_0x'$ i.e. f is linear and c_0 is constant (slope). Also, in this limit, $I_0(x'f(x'))$ is finite. So Eq. (3.21) can be written as

$$= -\frac{\mu c_0^2}{2\kappa^2} K_0(xf(x)) \int_0^x x'^2 \delta(x') I_0(x'f(x')) dx' = 0. \quad (3.22)$$

So, we can drop the $\delta^2(x)$ -function source term from Eq. (3.11) while looking for full solution. This greatly simplifies the problem.

The numerical solutions for B_z , B_ϕ , H_ϕ , J_ϕ and J_z are obtained using: $\mathbf{B} = \nabla \times \mathbf{A}$, $\mathbf{H} = \mathbf{B} - 4\pi\mathbf{M}$,

$$M_\phi(x) = \frac{\mu}{8\pi\kappa} \left[-\frac{1}{\kappa x} + A_\phi \right] f^2 \quad (3.23)$$

$$\text{and } J_z(x) = \frac{1}{4\pi} \left[-A_z + \frac{\mu}{2\kappa} B_{oz} \right] f^2. \quad (3.24)$$

The results are shown in Figs. 3.1, 3.2, 3.3, 3.4 and 3.5. Numerical integration of the current density J_z around the vortex line meets the physical requirement that the net current along the z-direction must be zero (J_z was numerically integrated from $x = 0$ to $x = 40$). The full numerical solution for J_z is compared with the solution in the London limit for $\mu = 0.020$ and $\kappa = 20$, in Fig. 3.6. The two match closely outside the core. Further, $J_{z,peak}$ decreases non-linearly with κ (Fig. 3.7) for fixed μ .

The magnitude of $B_{\phi,peak}$ is calculated to be ~ 0.08 gauss (G) and that of $J_{z,peak}$ is $\sim 6 \times 10^6$ A m⁻² for a μ value of 0.020. These values are appropriate for Li₂Pt₃B ($\kappa \approx 20$, $\lambda \approx 360$ nm [Ref. [91]]). For Mo₃Al₂C, $\kappa \approx 88$, $\lambda \approx 375.5$ nm [Ref. [45]] and with a μ value of 0.088, $B_{\phi,peak} \sim 0.3$ gauss (G) and $J_{z,peak} \sim 9.75 \times 10^6$ A m⁻². Though, current density along \hat{z} is large enough to produce measurable current in a small sample, the measurement of transverse field seem to be out of reach for now, as by one estimate [91] the resolution limit of μ SR (muon spin rotation) technique is 0.5 gauss (G) which is greater than the expected values reported here.

The current J_z changes sign at about 2λ (Fig. 3.5). Thus there exist a zero current surface at 2λ from vortex line. For negative winding, the current flows upwards before the zero current surface and it flows downwards after the zero current surface. For a boundary with normal along \hat{z} , the boundary conditions do not allow a current to flow through the surface, consequently, when J_z reaches the boundary from inside the zero current surface, it will flow radially outward and then flow back into the material outside the zero boundary surface.

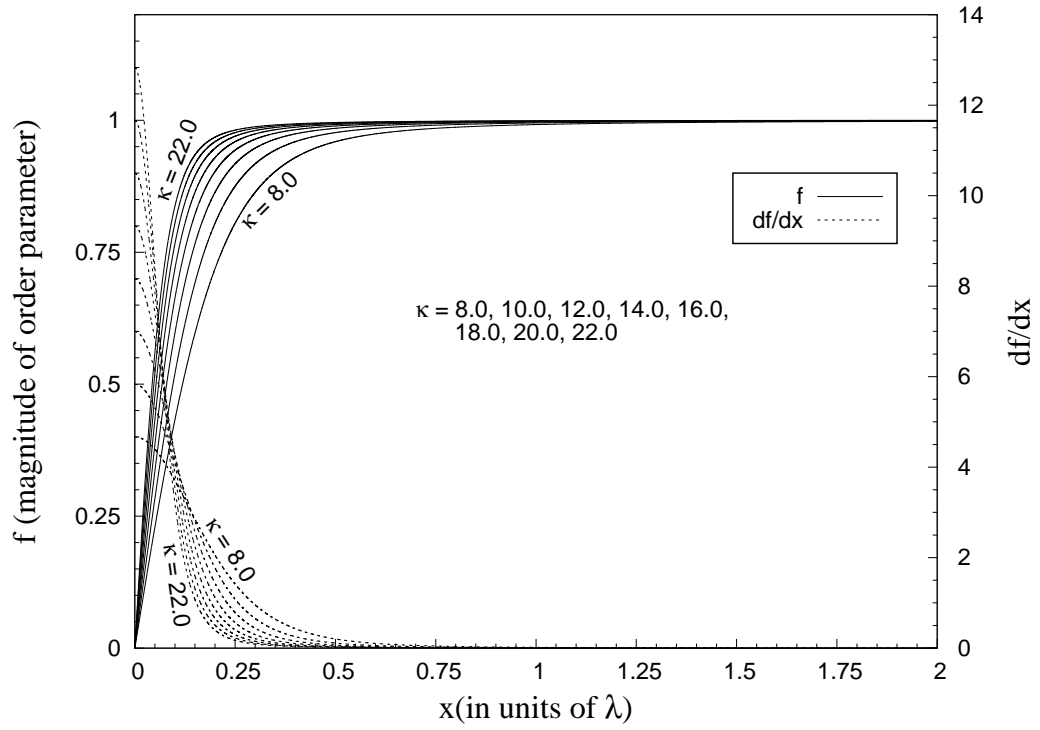


Figure 3.1: Order parameter (f) vs. radial distance from vortex center (x). Order parameter rises to its maximum value increasingly faster with larger values of κ

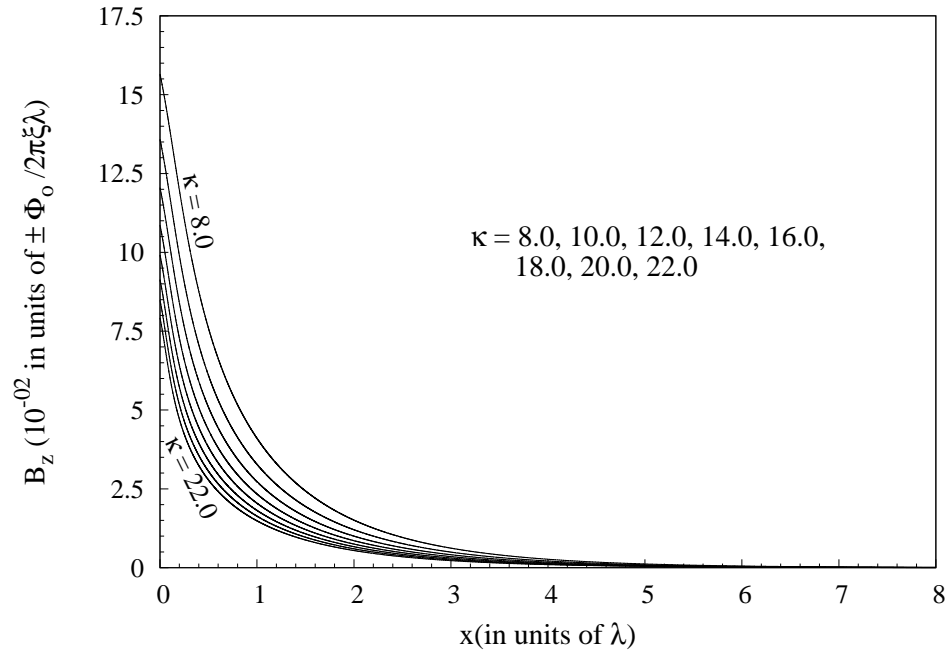


Figure 3.2: B_z vs. x . $B_z(0) = B_{0z}$ is finite as against the divergence in the London limit.

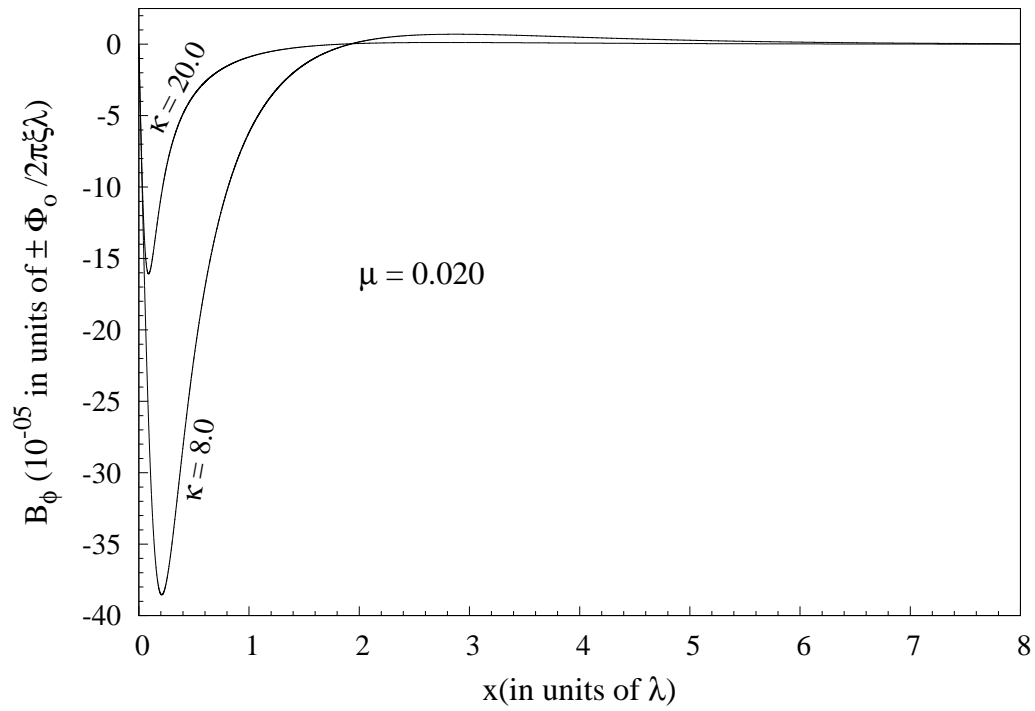


Figure 3.3: Magnetic flux density B_ϕ for $\mu = 0.020$

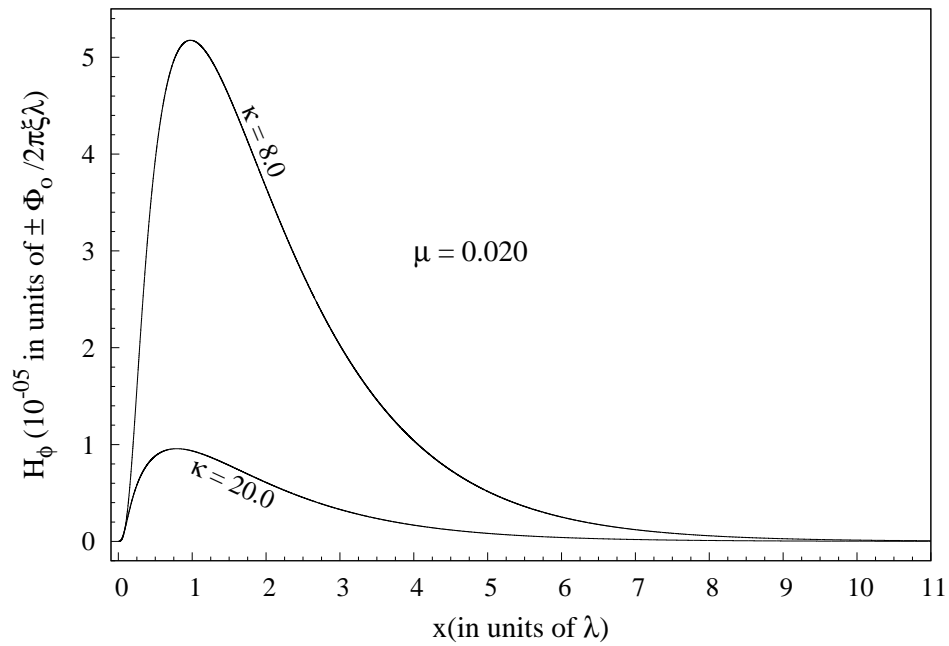


Figure 3.4: Magnetic field H_ϕ for $\mu = 0.020$

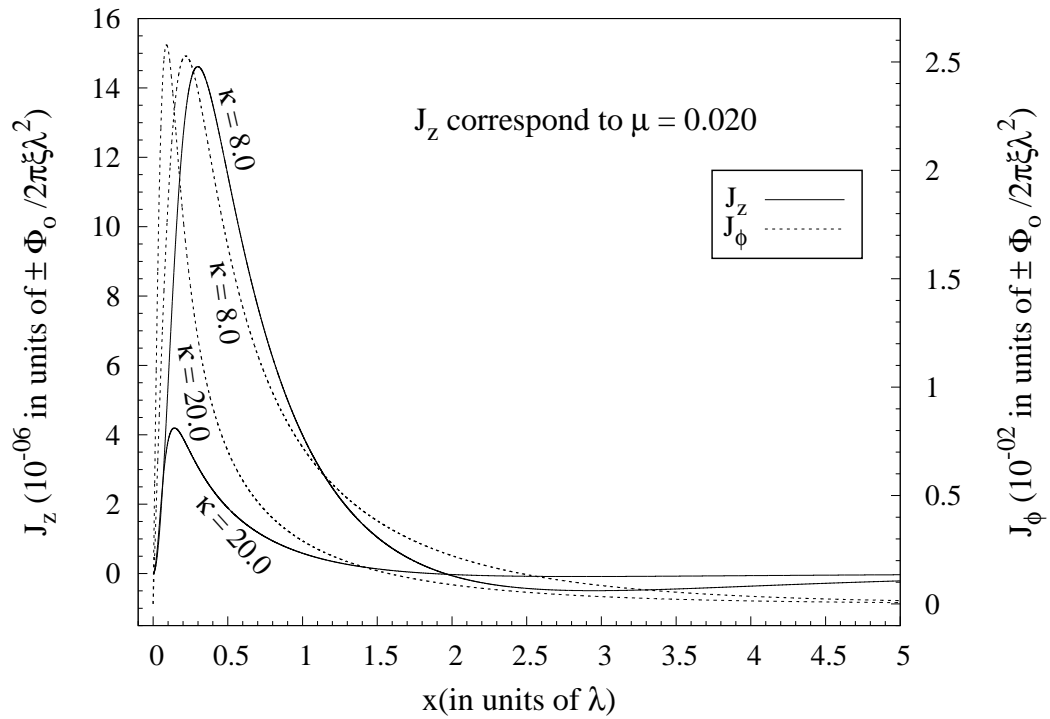


Figure 3.5: Components of current density \mathbf{J} . Plot of J_z correspond to $\mu = 0.020$

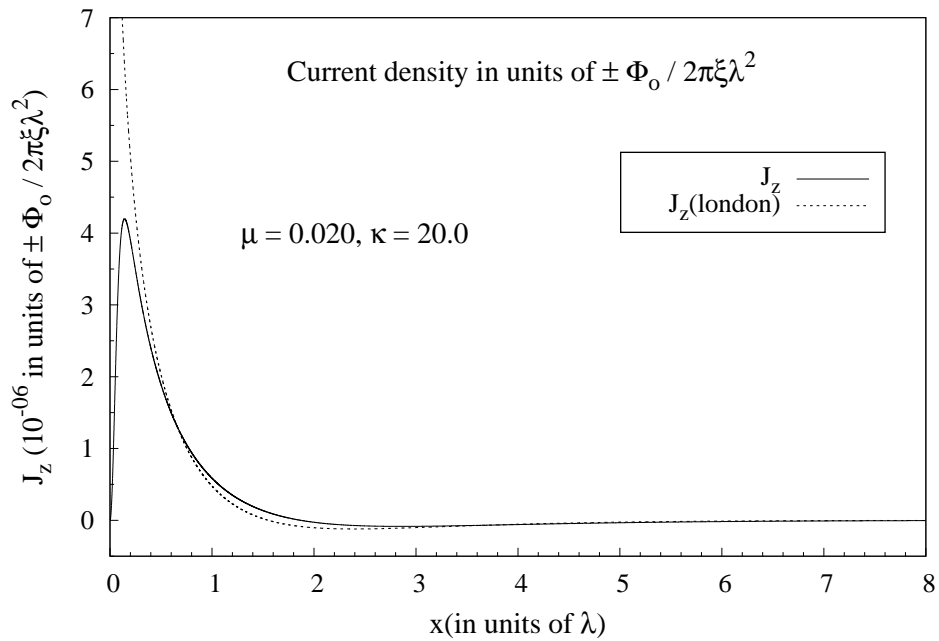


Figure 3.6: The plot shows the agreement between full solution and the london limit solution of current density J_z . Current density J_z as a function of radial distance.

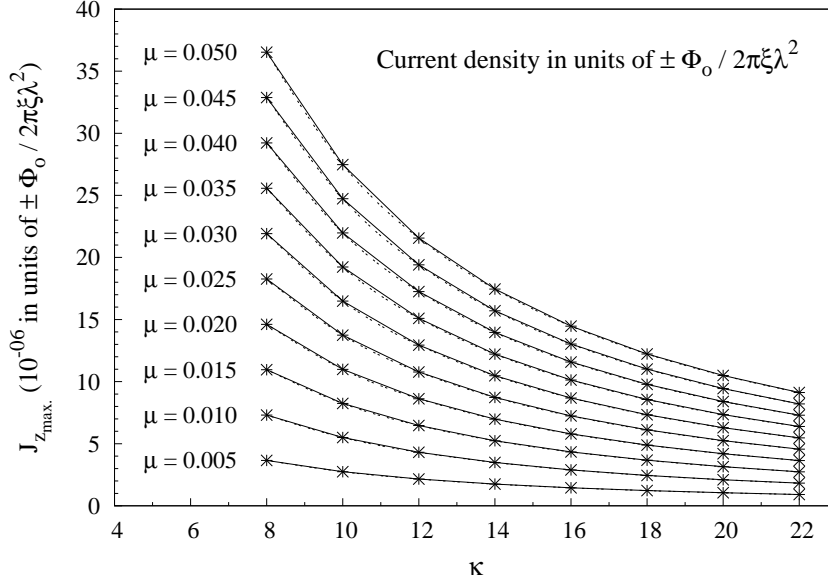


Figure 3.7: Peak Current ($J_{z_{max}}$) varies non-linearly with κ (for fixed μ). The dashed line is cubic spline fit.

3.4 Transverse field distribution near the upper critical field

Near the upper critical field, the order parameter η is known to have an Abrikosov's vortex lattice solution. Near B_{c2} , $|\eta|^2 \ll \Psi^2$. Therefore we can neglect non-linear terms in Eq. (3.1). This leads to linearized form of Eq. (3.2),

$$\alpha\eta + K\mathbf{D}^2\eta = 0. \quad (3.25)$$

Using London gauge $\mathbf{A} = (-B_0y, 0, 0)$, Eq. (3.25) can be written as

$$(-\nabla_y^2 + e^2B_0y^2 - \nabla_x^2 - i4eB_0y\nabla_x)\eta = \frac{1}{\xi^2}\eta, \quad \left(\text{here, } \frac{\alpha}{K} = -\frac{1}{\xi^2}\right). \quad (3.26)$$

Eq. (3.26) is an eigenvalue equation. The operator on L.H.S. in Eq. (3.26) commutes with the operator $p_x = -i\nabla_x$, because x is absent from it. Therefore the two must

have simultaneous eigenstates. Hence, $\eta \propto \phi = e^{ikx}\psi(y)$ because eigenstates of p_x are plane waves (e^{ikx}). Due to this separation of variable, we get a harmonic oscillator equation for $\psi(y)$ which can be written, with all lengths scaled by magnetic length $l_B = 1/\sqrt{2|eB_o|}$, as

$$\nabla_y^2 \psi(y) + 2 \left[\frac{1}{2\xi^2} - \frac{1}{2} (y \mp k)^2 \right] \psi(y) = 0. \quad (3.27)$$

In the last term in Eq. (3.27), upper sign corresponds to $eB_o < 0$ and lower sign to $eB_o > 0$. Here, $\omega = l_B^2 2|eB_o| = 1$. This defines the magnetic length l_B . The solution to Eq. (3.27) is quantized and is given by

$$\psi_n(y) = \exp \left[-\frac{1}{2} (y \mp k)^2 \right] H_n(y \mp k), \quad (3.28)$$

where H_n are Hermite polynomials.

The solution ϕ is still degenerate w.r.t. allowed values of k . Since we seek a lattice solution, only discrete values of k are allowed. The most general solution for ϕ with $k \equiv y_m$ can be written as

$$\phi_n(\mathbf{r}|\tau) = a_n \sum_{m=-\infty}^{\infty} c_m e^{iy_m x} e^{-\frac{(y \mp y_m)^2}{2}} H_n(y \mp y_m), \quad (3.29)$$

where $c_m = e^{i\pi m(\rho+1-\rho m)}$, $y_m = (m - 1/2)\sqrt{2\pi\sigma}$, $\rho = (b/a) \sin \alpha$, $\sigma = (b/a) \cos \alpha$, H_n are Hermite polynomials and $a_n = [2^n \pi^{1/2} (n!)]^{-1/2}$. Eq. (3.29) describes generalized vortex lattice solutions [87, 99, 100] with lattice vectors $\mathbf{a} = (a, 0)$ and $\mathbf{b} = b(\cos \alpha, \sin \alpha)$ and with a single flux quanta per unit cell (this lead to the constraint $ab \sin \alpha = 2\pi$, where all lengths are scaled by the magnetic length $l_B = 1/\sqrt{2|eB_o|}$). The lattice form depends on the complex parameter $\tau = \rho + i\sigma$. For conventional s -wave pairing, lattice is expected to be hexagonal, so we choose $a = b$ and $\alpha = \pi/3$

To linear order in ϵ , the transverse field at H_{c2} , when $\mathbf{J} \approx 0$, is given by $\mathbf{B}_\perp =$

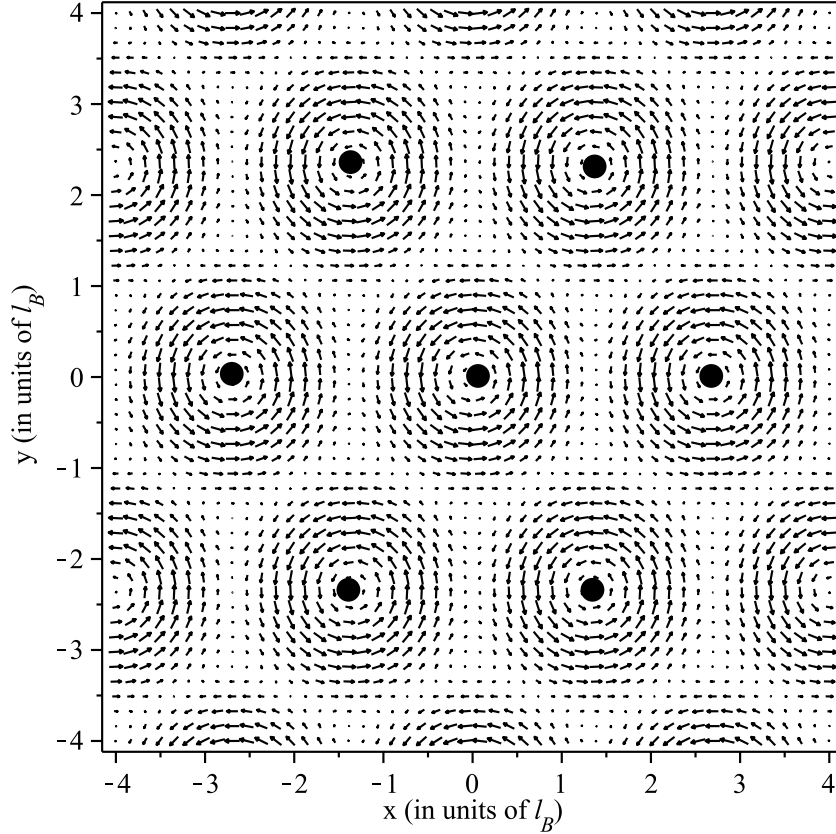


Figure 3.8: Transverse flux density (B_{\perp}) distribution near upper critical field, for $eB_o < 0$. The dark circles denote the position of vortex lines. The direction of the field lines is determined by the sign of ϵ .

$-4\pi\epsilon[\eta^*(\mathbf{D}\eta) + \eta(\mathbf{D}\eta)^*]$. Let us define operators $\Pi_+ = (\mp D_x - iD_y)/\sqrt{4|eB_o|}$ and $\Pi_- = (\mp D_x + iD_y)/\sqrt{4|eB_o|}$ (upper sign for $eB_o < 0$ and lower sign for $eB_o > 0$) in the Landau gauge. It turns out that Π_+ and Π_- are raising and lowering operators for ϕ_n and thereby for η . So, \mathbf{B}_{\perp} can be expressed in terms of the eigenstates of the operator $\Pi_+\Pi_-$ which are the same as given in Eq. (3.29). The order parameter near the upper critical field is $\eta = \sqrt{A} \phi_0$. This leads to:

$$\begin{aligned}
 B_x(x, y) &= A 4\pi\epsilon\sqrt{|eB_o|} [\pm(\phi_0^*\phi_1 + \phi_0\phi_1^*)] \\
 \text{and } B_y(x, y) &= A 4\pi\epsilon\sqrt{|eB_o|} [-i(\phi_0^*\phi_1 - \phi_0\phi_1^*)].
 \end{aligned}
 \tag{3.30}$$

The transverse flux density distribution near B_{c2} is shown in Fig. 3.8. Given the

redistribution of the transverse magnetic induction (as compared to a single vortex) due to lattice, it is possible that the transverse field in the high density regions is accessible in a μ SR experiment.

In addition, samples with many pinning centers can be treated using the Bean model. [11, 101] This predicts a non-zero average transverse flux density that is varying as a function of distance from the surface. This can also be observed through μ SR measurements. The field will be of the same order as in the vortex lattice.

3.5 Conclusions

We have studied s -wave cubic NCS with point group symmetry O using Ginzburg-Landau theory. Lack of inversion center, allows for the inclusion of Lifshitz invariants in the Ginzburg-Landau functional. Using the macroscopic theory we reproduced the single-vortex solution in NCS with cubic point group symmetry O in the London limit, which was earlier obtained through microscopic means. Going beyond the London limit, we have calculated the detailed structure of the transverse field B_ϕ and current J_z (current component in the same direction as the applied field) for a single vortex. Also, we have obtained the structure of the transverse field for a vortex lattice. Estimates of the magnitude of these fields suggest that they will be difficult to observe. The discovery of new superconductors with point group symmetry O that have smaller penetration depths and larger κ relative to $\text{Li}_2\text{Pt}_3\text{B}$ and $\text{Mo}_3\text{Al}_2\text{C}$ will allow these transverse fields to be observed more easily. We have not made any estimates about $\text{Li}_2\text{Pd}_3\text{B}$, which definitely needs to be considered. A similar study could be done for other point groups that lack inversion center. Also, there can be a theoretical study going beyond s -wave by including the possibility of additional broken symmetries which also lead to different form of the Lifshitz invariants.

The transverse fields are the result of magnetization M_ϕ which must be arising

due to component of the spin polarization in the transverse direction. Thus, Lifshitz invariants in cubic NCS lead to additional degrees of freedom in terms of B_{phi} (magnetic flux perpendicular to applied field) and J_z to manipulate, which can be potentially exploited in technological applications provided we have materials in which these effects are enhanced enough to be observed and controlled.

Chapter 4

Emergent Loop Current Order from Pair Density Wave Superconductivity

4.1 Introduction

The primary objective of the work presented in this chapter is to explain the pseudogap phase of the underdoped cuprates. The pseudogap phase shows the signatures of broken time-reversal (intraunit cell magnetic order), charge density wave (CDW) order and diamagnetism (indicating superconducting correlations). To explain the prevalence of superconducting (SC) correlations and CDW order, pair density wave (PDW) order has been suggested as an order parameter for the pseudogap phase [78, 102]. This proposal was bolstered by a demonstration that PDW order accounts for anomalous quasiparticle (QP) properties observed by angle-resolved photoemission (ARPES) [102]. PDW superconductivity is a spatially varying SC state similar to Fulde Ferrell Larkin Ovchinnikov (FFLO) states [103, 104]. It has been discussed in a variety of contexts for the cuprates [102, 105, 106, 107, 108].

Here we show that PDW order can naturally induce a translational invariant secondary order parameter that breaks both time-reversal and parity symmetries, but is invariant under the product of the two. Similar order parameters with this symmetry have appeared in the context of the cuprates under the name magnetoelectric (ME) order [109] and as ME loop current order [110]. Here we name such order ME loop current order. We further show that there exists a mean-field PDW ground state with ME loop current order that accounts for the Kerr effect and for intracell magnetic order, with CDW order at the observed wavevectors $2\mathbf{Q}_x = (2Q, 0)$ and $2\mathbf{Q}_y = (0, 2Q)$, and which accounts for qp properties observed by ARPES [70]. This PDW ground state has continuous $U(1)$ degeneracies (associated with broken SC gauge and translational symmetries) together with a discrete degeneracy associated with the ME loop current order. Fluctuations of the $U(1)$ degeneracies suppress both the SC and CDW order, allowing for a state with spatial long-range ME loop current order and short-range SC and CDW orders (Fig. 4.1). We propose that this state is responsible for behavior that emerges at the pseudogap temperature T^* [70]. Such a ME loop current state is conceptually similar to the nematic phase that arises due to magnetic fluctuations proposed for the pnictides [111] and to a translational invariant broken time-reversal symmetry state stemming from CDW and modulated bond current orders [112].

Since it is closely related to ME loop current PDW state we find, and has been used to explain the anomalous qp properties observed through ARPES experiments, we highlight the recent PDW proposal of Lee [102]. In particular, this proposal has its origin in a gauge theory description of the resonating valence bond phase. Here, pairing occurs through a transverse gauge field and leads to an incommensurate checkerboard PDW state for which the PDW order can be qualitatively expressed as $\Delta(\mathbf{x}) = \Delta_Q[\cos(\mathbf{Q}_x \cdot \mathbf{x}) + i \cos(\mathbf{Q}_y \cdot \mathbf{x})]$. This state has secondary CDW order at wavevectors $2\mathbf{Q}_x$ and $2\mathbf{Q}_y$, in agreement with experiment. This state cannot account

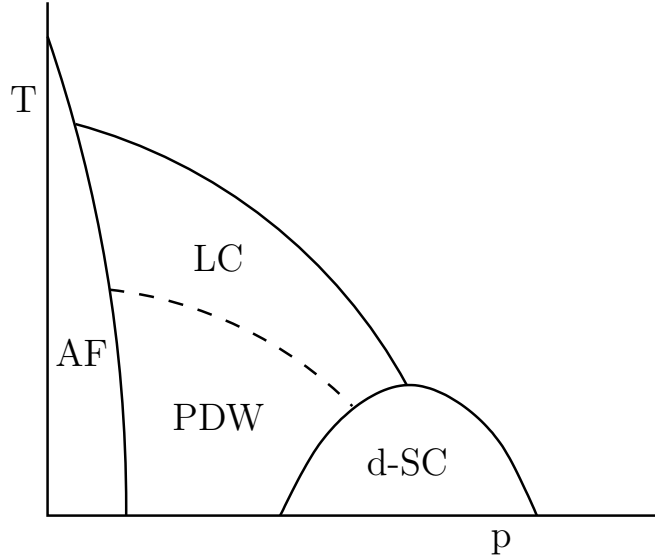


Figure 4.1: Qualitative temperature (T) versus hole doping (p) phase diagram. Here LC represents the ME loop current phase, PDW represents the pair density wave phase, AF represents antiferromagnetism, and d-SC represents d -wave superconductivity.

for the observed signatures of translational invariant broken time-reversal symmetry*.

In the following, we begin with a summary of the symmetry properties of PDW order and introduce the translational invariant loop current order parameter. This is followed by the relevant PDW action for tetragonal symmetry. For tetragonal symmetry, it is not possible to analytically find all possible ground states. For this reason we then turn to an analysis of PDW order for a theory with orthorhombic symmetry. This theory allows a complete understanding of all allowed PDW ground states and can be used to establish the existence of a phase which has long-range translation invariant loop current order but no long-range superconducting or CDW order. We then return to tetragonal symmetry and examine a loop current phase that is a natural generalization of that found for orthorhombic symmetry. After this we show there exists a PDW state that shares the same symmetry properties as the recent tilted loop current phase discussed by Yakovenko [113]. This phase is consistent with all observations of broken time-reversal symmetry in the underdoped cuprates. Fi-

*See Appendix C

nally, we examine the quasiparticle properties relevant to ARPES measurements for the tetragonal ME PDW phase. We show that while the qp properties of the ME PDW phase are similar to those found by Lee [102] for a PDW phase without loop current order, there are observable differences that will allow these two phases to be distinguished.

4.2 PDW induced translational invariant loop current order

PDW order originates when paired fermions have a finite center of mass momentum. It is characterized by order parameter components $\Delta_{\mathbf{Q}}$ which, under a translation \mathbf{T} , transform as $\Delta_{\mathbf{Q}} \rightarrow e^{i\mathbf{T}\cdot\mathbf{Q}}\Delta_{\mathbf{Q}}$. Key here are the transformation properties under time-reversal \mathcal{T} and parity symmetries \mathcal{P} :

$$\Delta_{\mathbf{Q}} \xrightarrow{\mathcal{T}} \Delta_{-\mathbf{Q}}^* \quad \text{and} \quad \Delta_{\mathbf{Q}} \xrightarrow{\mathcal{P}} \Delta_{-\mathbf{Q}}. \quad (4.1)$$

These symmetries suggest a consideration of the secondary ME loop current order parameter $l = (|\Delta_{\mathbf{Q}_i}|^2 - |\Delta_{-\mathbf{Q}_i}|^2)$. This order parameter has translational invariance, is odd under both \mathcal{T} and \mathcal{P} , and invariant under the product \mathcal{TP} . If a PDW ground state satisfies $|\Delta_{\mathbf{Q}_i}| \neq |\Delta_{-\mathbf{Q}_i}|$, then the state will have non-zero l . This condition is not satisfied by any of the PDW states proposed in the context of the cuprates [105, 107, 102, 78]. This motivates the question, are there stable PDW ground states that do exhibit loop current order? Below we show there are. We find that there exists a PDW ground state that can qualify as a pseudogap mean-field order parameter. We impose the following four criteria on such a state:

- It is a mean-field ground state of a Ginzburg-Landau-Wilson (GLW) action (for parameters that are not a set of measure zero in the GLW action parameter space).

- It has finite l and accounts for the Kerr effect and intracell magnetic order.
- It has CDW correlations at the observed momenta.
- It can account for ARPES spectra.

Prior to defining the PDW order parameter we consider in more detail, it is useful to point out that there are two previously found PDW ground states that should have finite l . The first is the well known Fulde-Ferrel (FF) phase for which $\Delta(\mathbf{x}) = e^{i\mathbf{Q}\cdot\mathbf{x}}$. This state has no CDW order and therefore cannot represent a pseudogap order parameter. The second state is found in Ref. [106], for which the gap can qualitatively be represented as $\Delta(\mathbf{x}) = \Delta_{\mathbf{Q}}[e^{i\mathbf{Q}_x\cdot\mathbf{x}} + e^{i\mathbf{Q}_y\cdot\mathbf{x}}]$. This state has CDW order, but this order is not at a wavevector that matches experiment and, consequently, cannot be a pseudogap order parameter[†].

Criterion 4 strongly restricts our search for a pseudogap order parameter. Specifically, we require that the Fermi arc is reproduced, the low energy bands near the anti-nodal point are reproduced (which has a gap minimum at momentum $k_G \neq k_F$, where k_F is Fermi momentum) [70], and the Fermi arc is derived from occupied states moving up towards the Fermi energy [70, 102]. The PDW state discussed in Ref. [102] gives rise to these properties, and it is natural to use this as a starting point. However, the GLW theory based on the PDW momenta chosen in Ref. [102] does not produce a ground state that satisfies the above four criteria and we must therefore consider generalizations of this state. To identify such a generalization, we note that a key feature of Ref. [102] that allows the ARPES spectra to be reproduced is the choice of the momenta about which fermions are paired. In particular, the mean-field pairing Hamiltonian for PDW order is

$$H = \sum_{\mathbf{p},s} \epsilon_{\mathbf{p}} c_{\mathbf{p}s}^{\dagger} c_{\mathbf{p}s} + \sum_{\mathbf{Q}_i, \mathbf{p}} [\Delta_{\mathbf{Q}_i}(\mathbf{p}) c_{\mathbf{p}+\mathbf{K}_i\uparrow}^{\dagger} c_{-\mathbf{p}+\mathbf{K}_i\downarrow}^{\dagger} + h.c.], \quad (4.2)$$

[†]See Appendix C

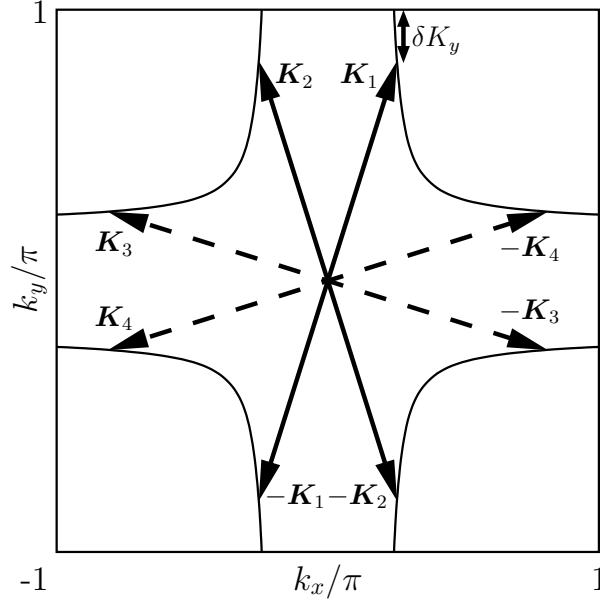


Figure 4.2: The positions of the momenta \mathbf{K}_i about which PDW Cooper pairs are formed. The corresponding eight PDW order parameter components $\Delta_{\mathbf{Q}_i}$ have momenta $\mathbf{Q}_i = 2\mathbf{K}_i$. The solid line momenta apply only to the theory with orthorhombic symmetry, and all the momenta (solid and dashed) are included for tetragonal symmetry. The displacement δK_y denotes the shift of the momenta \mathbf{K}_i from the zone edge. When $\delta K_y = 0$, the theory of Ref. [102] is reproduced.

where $c_{\mathbf{k}s}$ is the fermion destruction operator with momentum \mathbf{k} and spin s , $\epsilon_{\mathbf{k}}$ is the bare dispersion, and $h.c.$ means Hermitian conjugate. The momenta about which the fermions are paired are the \mathbf{K}_i , leading to PDW order at $\mathbf{Q}_i = 2\mathbf{K}_i$. In the following we examine PDW order that stems from the \mathbf{K}_i shown in Fig. 4.2. In the limit that $\delta K_y = 0$, the theory of Ref. [102] is reproduced. Consequently, we expect that for sufficiently small δK_y , the PDW states examined here should be able to reproduce the ARPES spectra. Section 4.8 shows that this is indeed the case.

4.3 GLW Action: tetragonal symmetry

The momenta[‡] specified in Fig. 4.2 lead to a PDW order parameter with eight complex degrees of freedom: $(\Delta_{\mathbf{Q}_1}, \Delta_{\mathbf{Q}_2}, \Delta_{\mathbf{Q}_3}, \Delta_{\mathbf{Q}_4}, \Delta_{-\mathbf{Q}_1}, \Delta_{-\mathbf{Q}_2}, \Delta_{-\mathbf{Q}_3}, \Delta_{-\mathbf{Q}_4})$. To con-

[‡]Here we consider only $\delta K_y \neq 0$. See Appendix C for the case when $\delta K_y = 0$

struct the GLW free energy, the transformation properties of this order parameter under rotations are required. The point group symmetry is D_{4h} with generators $\{C_4, \sigma_x, \sigma_z\}$ where C_4 is a 4-fold rotation about the c -axis and σ_x (σ_z) is a mirror reflection through y - z (x - y) plane. Under these generators, the PDW order $(\Delta_{\mathbf{Q}_1}, \Delta_{\mathbf{Q}_2}, \Delta_{\mathbf{Q}_3}, \Delta_{\mathbf{Q}_4}, \Delta_{-\mathbf{Q}_1}, \Delta_{-\mathbf{Q}_2}, \Delta_{-\mathbf{Q}_3}, \Delta_{-\mathbf{Q}_4})$ transforms as

$$\begin{aligned}
C_4 &: (\Delta_{\mathbf{Q}_3}, \Delta_{\mathbf{Q}_4}, \Delta_{-\mathbf{Q}_1}, \Delta_{-\mathbf{Q}_2}, \Delta_{-\mathbf{Q}_3}, \Delta_{-\mathbf{Q}_4}, \Delta_{\mathbf{Q}_1}, \Delta_{\mathbf{Q}_2}), \\
\sigma_x &: (\Delta_{\mathbf{Q}_2}, \Delta_{\mathbf{Q}_1}, \Delta_{-\mathbf{Q}_4}, \Delta_{-\mathbf{Q}_3}, \Delta_{-\mathbf{Q}_2}, \Delta_{-\mathbf{Q}_1}, \Delta_{\mathbf{Q}_4}, \Delta_{\mathbf{Q}_1}), \\
\sigma_z &: (\Delta_{\mathbf{Q}_1}, \Delta_{\mathbf{Q}_2}, \Delta_{\mathbf{Q}_3}, \Delta_{\mathbf{Q}_4}, \Delta_{-\mathbf{Q}_1}, \Delta_{-\mathbf{Q}_2}, \Delta_{-\mathbf{Q}_3}, \Delta_{-\mathbf{Q}_4}).
\end{aligned} \tag{4.3}$$

Considering invariance under translations, rotations, time-reversal, parity and gauge symmetries, the corresponding GLW action can be written as: $S_{0,\text{tet}} = S_{0,\text{hom}} + S_{0,\text{grad}}$. Here, $S_{0,\text{hom}}$ and $S_{0,\text{grad}}$ are

$$\begin{aligned}
S_{0,\text{hom}} &= r_0 \sum_i |\Delta_{\mathbf{Q}_i}|^2 + \beta_1 \left(\sum_i |\Delta_{\mathbf{Q}_i}|^2 \right)^2 \\
&+ \beta_2 (|\Delta_{\mathbf{Q}_1}|^2 |\Delta_{-\mathbf{Q}_1}|^2 + |\Delta_{\mathbf{Q}_2}|^2 |\Delta_{-\mathbf{Q}_2}|^2 + |\Delta_{\mathbf{Q}_3}|^2 |\Delta_{-\mathbf{Q}_3}|^2 + |\Delta_{\mathbf{Q}_4}|^2 |\Delta_{-\mathbf{Q}_4}|^2) \\
&+ \beta_3 (|\Delta_{\mathbf{Q}_1}|^2 |\Delta_{\mathbf{Q}_2}|^2 + |\Delta_{\mathbf{Q}_3}|^2 |\Delta_{\mathbf{Q}_4}|^2 + |\Delta_{-\mathbf{Q}_1}|^2 |\Delta_{-\mathbf{Q}_2}|^2 + |\Delta_{-\mathbf{Q}_3}|^2 |\Delta_{-\mathbf{Q}_4}|^2) \\
&+ \beta_4 (|\Delta_{\mathbf{Q}_1}|^2 |\Delta_{\mathbf{Q}_3}|^2 + |\Delta_{\mathbf{Q}_2}|^2 |\Delta_{\mathbf{Q}_4}|^2 + |\Delta_{\mathbf{Q}_3}|^2 |\Delta_{-\mathbf{Q}_1}|^2 + |\Delta_{\mathbf{Q}_4}|^2 |\Delta_{-\mathbf{Q}_2}|^2 \\
&+ |\Delta_{-\mathbf{Q}_1}|^2 |\Delta_{-\mathbf{Q}_3}|^2 + |\Delta_{-\mathbf{Q}_2}|^2 |\Delta_{-\mathbf{Q}_4}|^2 + |\Delta_{-\mathbf{Q}_3}|^2 |\Delta_{\mathbf{Q}_1}|^2 + |\Delta_{-\mathbf{Q}_4}|^2 |\Delta_{\mathbf{Q}_2}|^2) \\
&+ \beta_5 (|\Delta_{\mathbf{Q}_1}|^2 |\Delta_{\mathbf{Q}_4}|^2 + |\Delta_{-\mathbf{Q}_1}|^2 |\Delta_{-\mathbf{Q}_4}|^2 + |\Delta_{\mathbf{Q}_2}|^2 |\Delta_{-\mathbf{Q}_3}|^2 + |\Delta_{\mathbf{Q}_3}|^2 |\Delta_{-\mathbf{Q}_2}|^2) \\
&+ \beta_6 (|\Delta_{\mathbf{Q}_2}|^2 |\Delta_{\mathbf{Q}_3}|^2 + |\Delta_{\mathbf{Q}_4}|^2 |\Delta_{-\mathbf{Q}_1}|^2 + |\Delta_{-\mathbf{Q}_2}|^2 |\Delta_{-\mathbf{Q}_3}|^2 + |\Delta_{-\mathbf{Q}_4}|^2 |\Delta_{\mathbf{Q}_1}|^2) \\
&+ \beta_7 (|\Delta_{\mathbf{Q}_1}|^2 |\Delta_{-\mathbf{Q}_2}|^2 + |\Delta_{\mathbf{Q}_2}|^2 |\Delta_{-\mathbf{Q}_1}|^2 + |\Delta_{\mathbf{Q}_3}|^2 |\Delta_{-\mathbf{Q}_4}|^2 + |\Delta_{\mathbf{Q}_4}|^2 |\Delta_{-\mathbf{Q}_3}|^2) \\
&+ \beta_{c_1} \{ [\Delta_{\mathbf{Q}_1} \Delta_{-\mathbf{Q}_1} (\Delta_{\mathbf{Q}_2} \Delta_{-\mathbf{Q}_2})^* + \Delta_{\mathbf{Q}_3} \Delta_{-\mathbf{Q}_3} (\Delta_{\mathbf{Q}_4} \Delta_{-\mathbf{Q}_4})^*] + c.c. \} \\
&+ \beta_{c_2} \{ [\Delta_{\mathbf{Q}_1} \Delta_{-\mathbf{Q}_1} (\Delta_{\mathbf{Q}_3} \Delta_{-\mathbf{Q}_3})^* + \Delta_{\mathbf{Q}_2} \Delta_{-\mathbf{Q}_2} (\Delta_{\mathbf{Q}_4} \Delta_{-\mathbf{Q}_4})^*] + c.c. \} \\
&+ \beta_{c_3} \{ [\Delta_{\mathbf{Q}_1} \Delta_{-\mathbf{Q}_1} (\Delta_{\mathbf{Q}_4} \Delta_{-\mathbf{Q}_4})^* + \Delta_{\mathbf{Q}_2} \Delta_{-\mathbf{Q}_2} (\Delta_{\mathbf{Q}_3} \Delta_{-\mathbf{Q}_3})^*] + c.c. \}, \tag{4.4}
\end{aligned}$$

$$\begin{aligned}
S_{0,\text{grad}} = & \kappa_1 \sum_i |D_\perp \Delta_{\mathbf{Q}_i}|^2 \\
& + \kappa_2 \left[\sum_{\mathbf{Q}_j=\pm\mathbf{Q}_{1,2}} (|D_x \Delta_{\mathbf{Q}_j}|^2 - |D_y \Delta_{\mathbf{Q}_j}|^2) - \sum_{\mathbf{Q}_k=\pm\mathbf{Q}_{3,4}} (|D_x \Delta_{\mathbf{Q}_k}|^2 - |D_y \Delta_{\mathbf{Q}_k}|^2) \right] \\
& + \kappa_3 \left[\sum_{\mathbf{Q}_l=\pm\mathbf{Q}_{1,4}} [(D_x \Delta_{\mathbf{Q}_l})(D_y \Delta_{\mathbf{Q}_l})^* + c.c.] - \sum_{\mathbf{Q}_m=\pm\mathbf{Q}_{2,3}} [(D_x \Delta_{\mathbf{Q}_m})(D_y \Delta_{\mathbf{Q}_m})^* + c.c.] \right] \\
& + \kappa_4 \sum_i |D_z \Delta_{\mathbf{Q}_i}|^2 + \frac{1}{2}(\nabla \times \mathbf{A})^2, \quad (4.5)
\end{aligned}$$

where $\mathbf{D} = -i\nabla - 2e\mathbf{A}$, $\mathbf{D}_\perp = (D_x, D_y)$, and $\mathbf{B} = \nabla \times \mathbf{A}$. In the spatially homogeneous case (for which spatial variations of the order parameter are ignored), the possible ground states depend upon nine unknown phenomenological constants. This parameter space is too large to carry out a complete analysis of all the possible ground states. However, with the above action, it is straightforward to find the conditions under which a particular state is a local minimum. In Section 4.5, we shall consider a simplified theory that applies to materials with orthorhombic symmetry (such as YBCO), for which a complete analysis can be carried out. This analysis yields a PDW state compatible with experiments and then we generalize this state to tetragonal symmetry. Prior to the discussion of the solvable orthorhombic theory, we first consider the secondary order parameters that are relevant for PDW order.

4.4 Secondary order parameters

Different PDW ground states are distinguished by the secondary order parameters that are induced by the PDW order. These secondary order parameters play a central role in situations in which the original PDW order does not appear either due to impurities or due to fluctuations. In some circumstance, these secondary order parameters have also been named vestigial order [114]. These secondary or-

der parameters are identified by examining all possible bi-linear products of the $\Delta_{\mathbf{Q}_i}$. This leads to five distinct kinds of secondary order: CDW [105, 106], orbital density wave order (ODW) [106] (with spatially modulated orbital currents), translational invariant charge-4 superconductivity (4SC) [115, 116] (we do not consider finite-momentum charge-4 superconductivity), strain [115, 116], and translational invariant loop current (LC) order. Specifically, the CDW order is given by $\rho_{2\mathbf{Q}} \propto (\Delta_{\mathbf{Q}}\Delta_{-\mathbf{Q}}^* + \Delta_{-\mathbf{Q}}\Delta_{\mathbf{Q}}^*)$ or $\rho_{\mathbf{Q}_1-\mathbf{Q}_2} \propto (\Delta_{\mathbf{Q}_1}\Delta_{\mathbf{Q}_2}^* + \Delta_{-\mathbf{Q}_2}\Delta_{-\mathbf{Q}_1}^*)$, the ODW order is given by $L_{\mathbf{Q}_1-\mathbf{Q}_2}^z \propto i(\Delta_{\mathbf{Q}_1}\Delta_{-\mathbf{Q}_2}^* - \Delta_{\mathbf{Q}_2}\Delta_{-\mathbf{Q}_1}^*)$, the 4SC order is given by $\Delta_4 \propto \Delta_{\mathbf{Q}}\Delta_{-\mathbf{Q}}$, strain order is given by $\epsilon_i \propto (|\Delta_{\mathbf{Q}_1}|^2 + |\Delta_{-\mathbf{Q}_1}|^2 - |\Delta_{\mathbf{Q}_2}|^2 - |\Delta_{-\mathbf{Q}_2}|^2)$ [105, 116], and the loop current order, which was discussed above, by $l_i \propto (|\Delta_{\mathbf{Q}_i}|^2 - |\Delta_{-\mathbf{Q}_i}|^2)$.

4.5 GLW Action: orthorhombic symmetry

Here we consider the orthorhombic variant of Fig. 4.2. The GLW action in this case allows all possible ground states to be found and further allows for a analysis of preemptive loop current order discussed in the next section. The order parameter has four complex degrees of freedom and is represented by the momenta given by the solid arrows in Fig. 4.2. The same symmetry considerations as in Section 4.3 lead to the partition function $Z \propto \int \Pi_i \mathcal{D}\Delta_i e^{-S_0}$ with GLW action S_0 given by

$$\begin{aligned}
S_0 = & r_0 \sum_i |\Delta_{\mathbf{Q}_i}|^2 + \frac{\beta_1}{2} \left(\sum_i |\Delta_{\mathbf{Q}_i}|^2 \right)^2 \\
& + \frac{\beta_2}{2} (|\Delta_{\mathbf{Q}_1}|^2 + |\Delta_{-\mathbf{Q}_1}|^2 - |\Delta_{\mathbf{Q}_2}|^2 - |\Delta_{-\mathbf{Q}_2}|^2)^2 \\
& + \frac{\beta_3}{2} (|\Delta_{\mathbf{Q}_1}|^2 - |\Delta_{-\mathbf{Q}_1}|^2 - |\Delta_{\mathbf{Q}_2}|^2 + |\Delta_{-\mathbf{Q}_2}|^2)^2 \\
& + \frac{\beta_4}{2} (|\Delta_{\mathbf{Q}_1}|^2 - |\Delta_{-\mathbf{Q}_1}|^2 + |\Delta_{\mathbf{Q}_2}|^2 - |\Delta_{-\mathbf{Q}_2}|^2)^2 \\
& + \beta_5 [\Delta_{\mathbf{Q}_1}\Delta_{-\mathbf{Q}_1}(\Delta_{\mathbf{Q}_2}\Delta_{-\mathbf{Q}_2})^* + \Delta_{\mathbf{Q}_2}\Delta_{-\mathbf{Q}_2}(\Delta_{\mathbf{Q}_1}\Delta_{-\mathbf{Q}_1})^*] \\
& + \kappa_1 \sum_i |D_{\perp}\Delta_i|^2 + \kappa_2 \sum_i (|D_x\Delta_i|^2 - |D_y\Delta_i|^2)
\end{aligned}$$

$$\begin{aligned}
& + \kappa_3 [((D_x \Delta_{\mathbf{Q}_1})(D_y \Delta_{\mathbf{Q}_1})^* + (D_x \Delta_{-\mathbf{Q}_1})(D_y \Delta_{-\mathbf{Q}_1})^* \\
& - (D_x \Delta_{\mathbf{Q}_2})(D_y \Delta_{\mathbf{Q}_2})^* - (D_x \Delta_{-\mathbf{Q}_2})(D_y \Delta_{-\mathbf{Q}_2})^*) + c.c.] \\
& + \kappa_4 \sum_i |D_z \Delta_{\mathbf{Q}_i}|^2 + \frac{1}{2}(\nabla \times \mathbf{A})^2. \quad (4.6)
\end{aligned}$$

4.5.1 Ground states

For this action [Eq. (4.6)], it is possible to find all homogeneous mean-field ground states analytically. These are listed in Table 4.1 together with the corresponding conditions that the ground state represents a global minimum, secondary order parameters, and degeneracy manifold (degeneracy manifold specifies the number of states with the same ground state energy). Of the ground states listed in Table 4.1, only one state (named the ME PDW state) has the potential to represent a pseudogap mean-field order parameter when generalized to tetragonal symmetry. This ME PDW state has the order parameter $(\Delta_{\mathbf{Q}_1}, \Delta_{\mathbf{Q}_2}, \Delta_{-\mathbf{Q}_1}, \Delta_{-\mathbf{Q}_2}) = \Delta(1, 1, 0, 0)$ and is depicted in Fig. 4.3. It is stable when $\beta_1 + \beta_2 > 0$, $\beta_2 + \beta_3 > 0$, $\beta_4 < \beta_2$, $\beta_4 < \beta_3$, and $\beta_4 < -|\beta_5|/4$. This state can be characterized by the secondary orders that it induces: loop current order $l_y = |\Delta_{\mathbf{Q}_1}|^2 - |\Delta_{-\mathbf{Q}_1}|^2 + |\Delta_{\mathbf{Q}_2}|^2 - |\Delta_{-\mathbf{Q}_2}|^2$; CDW order $\rho_{2\mathbf{Q}_x} = \Delta_{\mathbf{Q}_1} \Delta_{\mathbf{Q}_2}^* + \Delta_{-\mathbf{Q}_2} \Delta_{-\mathbf{Q}_1}^*$; and orbital density wave (ODW) order at the same wavevector as the CDW order $L_{2\mathbf{Q}_x}^z = i(\Delta_{\mathbf{Q}_1} \Delta_{-\mathbf{Q}_2}^* - \Delta_{\mathbf{Q}_2} \Delta_{-\mathbf{Q}_1}^*)$ (L^z is the z -component of angular momentum). The ground state manifold of the ME PDW state has a $U(1) \times U(1) \times Z_2$ degeneracy. The two $U(1)$ degeneracies arise from the usual SC phase symmetry breaking and from the breaking of translational invariance. The Z_2 symmetry denotes the degeneracy between the $(\Delta_{\mathbf{Q}_1}, \Delta_{\mathbf{Q}_2}, \Delta_{-\mathbf{Q}_1}, \Delta_{-\mathbf{Q}_2}) = \Delta(1, 1, 0, 0)$ and $\Delta(0, 0, 1, 1)$ states and is associated with the ME loop current order (which is of opposite sign for these two degenerate states). In the next section we discuss how this ground state manifold can give rise to a preemptive transition for which there is only ME loop current long-range order.

Table 4.1: Properties of PDW Ground States for orthorhombic symmetry in Fig. 4.2. All possible PDW ground states and accompanying CDW and ODW order. The second column shows the parameter regions for which these phases are stable. In the third and fourth columns: $2\mathbf{Q}_x = (2Q, 0)$, $2\mathbf{Q}_y = (0, 2Q)$, other modes can be found by using the relationships $\rho_{\mathbf{Q}} = (\rho_{-\mathbf{Q}})^*$ and $L_{\mathbf{Q}}^z = (L_{-\mathbf{Q}}^z)^*$. The fifth column gives all translational invariant order parameters with $l_x \propto |\Delta_{\mathbf{Q}_1}|^2 - |\Delta_{-\mathbf{Q}_1}|^2 - |\Delta_{\mathbf{Q}_2}|^2 + |\Delta_{-\mathbf{Q}_2}|^2$, $l_y \propto |\Delta_{\mathbf{Q}_1}|^2 - |\Delta_{-\mathbf{Q}_1}|^2 + |\Delta_{\mathbf{Q}_2}|^2 - |\Delta_{-\mathbf{Q}_2}|^2$, $\Delta_{4e,s} \propto \Delta_{\mathbf{Q}_1}\Delta_{-\mathbf{Q}_1} + \Delta_{\mathbf{Q}_2}\Delta_{-\mathbf{Q}_2}$, $\Delta_{4e,d} \propto \Delta_{\mathbf{Q}_1}\Delta_{-\mathbf{Q}_1} - \Delta_{\mathbf{Q}_2}\Delta_{-\mathbf{Q}_2}$, and $\epsilon_{xy} \propto |\Delta_{\mathbf{Q}_1}|^2 + |\Delta_{-\mathbf{Q}_1}|^2 - |\Delta_{\mathbf{Q}_2}|^2 - |\Delta_{-\mathbf{Q}_2}|^2$. The sixth column gives the degeneracy of the ground state.

$(\Delta_{\mathbf{Q}_1}, \Delta_{\mathbf{Q}_2}, \Delta_{-\mathbf{Q}_1}, \Delta_{-\mathbf{Q}_2})$	Stability	CDW modes	ODW modes	Q=0 Order	Degeneracy Manifold
(1, 0, 0, 0)	$\beta_2 + \beta_3 < 0, \beta_2 + \beta_4 < 0$	none	none	ϵ_{xy}	$U(1) \times Z_2 \times Z_2$
	$\beta_3 + \beta_4 < 0$				
(1, 1, 0, 0)	$\beta_2 + \beta_3 + \beta_4 < - \beta_5 /4$	$\rho_{2\mathbf{Q}_x}$	$L_{2\mathbf{Q}_x}^z$	l_y	$U(1) \times U(1) \times Z_2$
	$\beta_2 + \beta_3 > 0, \beta_4 < \beta_2$				
(1, 0, 0, 1)	$\beta_4 < \beta_3, \beta_4 < - \beta_5 /4$	$\rho_{2\mathbf{Q}_y}$	$L_{2\mathbf{Q}_y}^z$	l_x	$U(1) \times U(1) \times Z_2$
	$\beta_2 + \beta_4 > 0, \beta_3 < \beta_2$				
(1, 0, 1, 0)	$\beta_3 < \beta_4, \beta_3 < - \beta_5 /4$	$\rho_{2\mathbf{Q}_1}$	none	ϵ_{xy}	$U(1) \times U(1) \times Z_2$
	$\beta_2 < \beta_4, \beta_2 < - \beta_5 /4$				
(1, 1, 1, 1)	$\beta_5 < 0, \beta_5 < 4\beta_2$	$\rho_{2\mathbf{Q}_1}, \rho_{2\mathbf{Q}_2}$	none	$\Delta_{4e,s}$	$U(1) \times U(1) \times U(1)$
	$\beta_5 < 4\beta_3, \beta_5 < 4\beta_4$				
(1, i , 1, i)	$\beta_5/4 < \beta_2 + \beta_3 + \beta_4$	$\rho_{2\mathbf{Q}_x}, \rho_{2\mathbf{Q}_y}$	$L_{2\mathbf{Q}_y}^z, L_{2\mathbf{Q}_x}^z$	$\Delta_{4e,d}$	$U(1) \times U(1) \times U(1)$
	$\beta_5 > 0, -\beta_5 < 4\beta_2$				
(1, i , 1, i)	$-\beta_5 < 4\beta_3, -\beta_5 < 4\beta_4$	$\rho_{2\mathbf{Q}_1}, \rho_{2\mathbf{Q}_2}$	$L_{2\mathbf{Q}_y}^z, L_{2\mathbf{Q}_x}^z$	$\Delta_{4e,d}$	$U(1) \times U(1) \times U(1)$
	$-\beta_5/4 < \beta_2 + \beta_3 + \beta_4$				

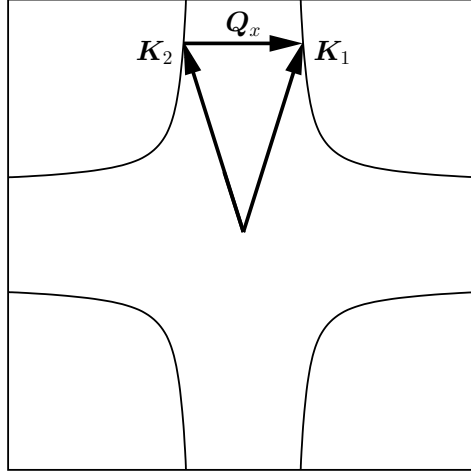


Figure 4.3: The ME PDW state for orthorhombic symmetry. The arrows K_i depict the non-zero components of the PDW order parameter (which order at $Q_i = 2K_i$). Together with the PDW order at the two wavevectors Q_i , this state has CDW order at the wavevector $2Q_x = Q_1 - Q_2$, ODW order at the same wavevector, and ME loop current order.

4.5.2 Emergent loop current order - Orthorhombic symmetry

Fluctuations can lead to a preemptive transition in which the $U(1) \times U(1)$ symmetry is not broken, but the Z_2 symmetry is. Such a state will exhibit spatial long-range ME loop current order and short-range SC and CDW order. To examine this possibility, we consider the partition function given by the effective action in Eq. (4.6) in two dimensions (2D), ignore the vector potential, and focus on the parameter regime for which the ME PDW state is stable. We decouple the quartic terms through Hubbard-Stratonovich (HS) transformations. In particular, we introduce the field ψ to decouple the $(\sum_i |\Delta_i|^2)^2$ term, ϵ_{xy} to decouple the $(|\Delta_{Q_1}|^2 + |\Delta_{-Q_1}|^2 - |\Delta_{Q_2}|^2 - |\Delta_{-Q_2}|^2)^2$ term, l_x to decouple the $(|\Delta_{Q_1}|^2 - |\Delta_{-Q_1}|^2 - |\Delta_{Q_2}|^2 + |\Delta_{-Q_2}|^2)^2$ term, l_y to decouple the $(|\Delta_{Q_1}|^2 - |\Delta_{-Q_1}|^2 + |\Delta_{Q_2}|^2 - |\Delta_{-Q_2}|^2)^2$ term, and two complex fields $\Delta_{4e,s}$ and $\Delta_{4e,d}$ to decouple the $[\Delta_{Q_1}\Delta_{-Q_1}(\Delta_{Q_2}\Delta_{-Q_2})^* + \Delta_{Q_2}\Delta_{-Q_2}(\Delta_{Q_1}\Delta_{-Q_1})^*]$ term. The resultant action is quadratic in the fields Δ_{Q_i} and these fields can be integrated out. For the parameter regime we examine, the phases with non-zero $\Delta_{4e,s}$ and $\Delta_{4e,d}$ are

energetically unfavorable. Consequently we set these fields to zero. Additionally, the remaining fields have Ising symmetry, so it is reasonable to treat these at a mean-field level. This leads to the following effective action

$$\begin{aligned} \frac{S_{\text{eff}}}{A} = & \frac{l_x^2}{2|\beta_3|} + \frac{l_y^2}{2|\beta_4|} - \frac{\psi^2}{2\beta_1} - \frac{\epsilon_{xy}^2}{2\beta_2} \\ & + \int \frac{d^2q}{4\pi^2} \ln \left[(\chi_{1,\mathbf{q}}^{-1} + \epsilon_{xy} + l_x + l_y)(\chi_{1,\mathbf{q}}^{-1} + \epsilon_{xy} - l_x - l_y) \right. \\ & \left. (\chi_{2,\mathbf{q}}^{-1} - \epsilon_{xy} + l_x - l_y)(\chi_{2,\mathbf{q}}^{-1} - \epsilon_{xy} - l_x + l_y) \right], \quad (4.7) \end{aligned}$$

where A is the area, $\chi_{1,\mathbf{q}}^{-1} = r_0 + \psi + \kappa_1 q^2 + \kappa_2(q_x^2 - q_y^2) + 2\kappa_3 q_x q_y$, $\chi_{2,\mathbf{q}}^{-1} = r_0 + \psi + \kappa_1 q^2 + \kappa_2(q_x^2 - q_y^2) - 2\kappa_3 q_x q_y$. The anisotropy due to κ_2 and κ_3 can be removed by rotating and re-scaling q_x and q_y , yielding $(\tilde{q}_x^2 + \tilde{q}_y^2)/\tilde{\kappa}$ with $\tilde{\kappa} = \sqrt{\kappa_1^2 - \kappa_2^2 - \kappa_3^2}$, and the integrals over momenta can then be carried out. Treating S_{eff} within a mean field approximation leads to the following self-consistency equations

$$\begin{aligned} r^* &= \bar{r}_0 - \tilde{\beta}_1 \ln \left\{ [(r^* + \epsilon_{xy}^*)^2 - (l_x^* + l_y^*)^2][(r^* - \epsilon_{xy}^*)^2 - (l_x^* - l_y^*)^2] \right\}, \\ \epsilon_{xy}^* &= -\tilde{\beta}_2 \ln \left[\frac{(r^* + \epsilon_{xy}^*)^2 - (l_x^* + l_y^*)^2}{(r^* - \epsilon_{xy}^*)^2 - (l_x^* - l_y^*)^2} \right], \\ l_x^* &= -\tilde{\beta}_3 \ln \left[\frac{(r^* + l_x^*)^2 - (\epsilon_{xy}^* + l_y^*)^2}{(r^* - l_x^*)^2 - (\epsilon_{xy}^* - l_y^*)^2} \right], \\ l_y^* &= \ln \left[\frac{(r^* + l_y^*)^2 - (\epsilon_{xy}^* + l_x^*)^2}{(r^* - l_y^*)^2 - (\epsilon_{xy}^* - l_x^*)^2} \right], \end{aligned} \quad (4.8)$$

where $r^* = r_0^* + \psi^*$, the $*$ denotes a rescaling by a factor $4\pi\tilde{\kappa}/|\beta_4|$, $\tilde{\beta}_i = \beta_i/|\beta_4|$, $\bar{r}_0 = r_0^* + 8\tilde{\beta}_1 \ln \Lambda + 4\tilde{\beta}_1 \ln(4\pi\tilde{\kappa}/|\beta_4|)$ and Λ is the momentum cutoff. We find that for parameters β_i such that the ME PDW state is stable, the mean field solution is given by $\epsilon_{xy} = l_x = 0$ and $l_y \neq 0$. Therefore, the solution reduces to only two self-consistency equations

$$r^* = \bar{r}_0 - 2\tilde{\beta}_1 \ln \left\{ [(r^{*2} - l_y^{*2})] \right\} \quad (4.9)$$

$$\text{and} \quad l_y^* = 2 \ln \left[\frac{(r^* + l_y^*)}{(r^* - l_y^*)} \right] \quad (4.10)$$

Eq. (4.10) can be rewritten as[§]

$$r^* = l_y^* \coth \left(\frac{l_y^*}{4} \right) \quad (4.11)$$

Eliminating r^* from Eq. (4.11) using Eq. (4.9) we get

$$\bar{r}_0 = \bar{l}_y \coth(\bar{l}_y) + \tilde{\beta}_1 \ln \left[\frac{\bar{l}_y}{\sinh(\bar{l}_y)} \right] \quad (4.12)$$

where $\bar{l}_y = \frac{l_y^*}{4}$ and $\bar{r}_0 = \frac{\bar{r}_0}{4} - 2\tilde{\beta}_1 \ln 2$. The mathematical analysis of this solution is the same as that used to examine preemptive nematic order in Ref. [111]. This work implies that there is a second order transition into a ME loop current state when $\tilde{\beta}_1 > 2$ (this becomes first order transition if $\tilde{\beta}_1 < 2$). This analysis can be extended to three dimensions and, provided $\kappa_4/\tilde{\kappa}$ is sufficiently small, a second order transition into a loop current phase will occur [111]. Such a preemptive ME loop current phase will exhibit: SC and CDW correlations consistent with experiment [73, 74, 75, 77, 78]; broken time-reversal symmetry; broken parity symmetry; and is invariant under the product of time-reversal and parity symmetry.

4.6 In-plane loop current order – tetragonal symmetry

The ME PDW state found in Section 4.5.1 has a natural generalization to tetragonal symmetry. In particular, $(\Delta_{\mathbf{Q}_1}, \Delta_{\mathbf{Q}_2}, \Delta_{\mathbf{Q}_3}, \Delta_{\mathbf{Q}_4}, \Delta_{-\mathbf{Q}_1}, \Delta_{-\mathbf{Q}_2}, \Delta_{-\mathbf{Q}_3}, \Delta_{-\mathbf{Q}_4}) = (\Delta_1, \Delta_2, 0, 0, 0, 0, \Delta_2, \Delta_1)$ is a stable state of the tetragonal GLW action (this will

[§] $\coth(x) = \frac{e^x + e^{-x}}{e^x - e^{-x}}$

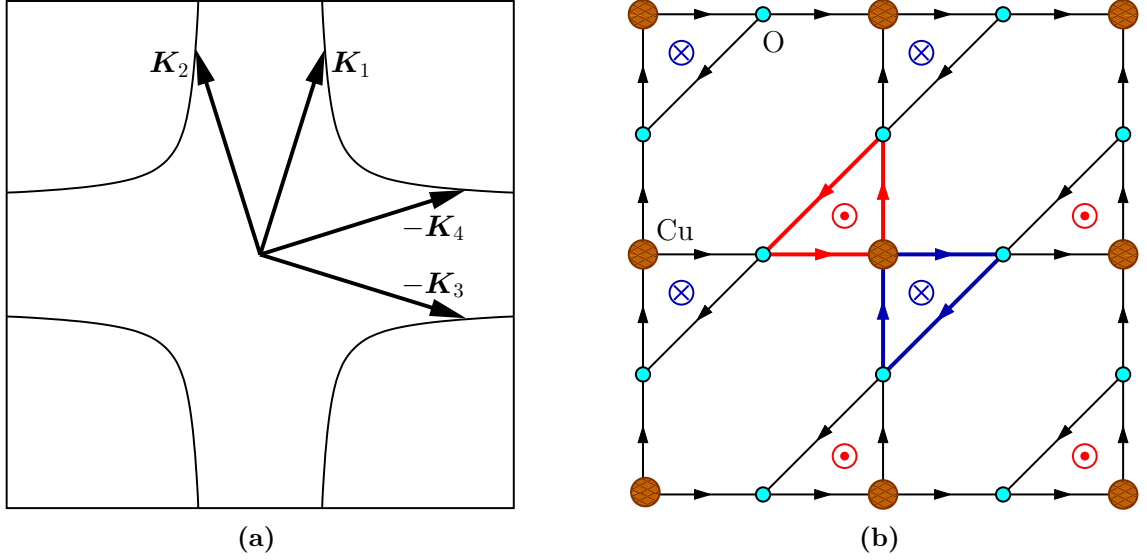


Figure 4.4: The ME PDW state for tetragonal symmetry. (a) The arrows K_i depict the non-zero components of the PDW order parameter in the ME PDW state (which order at $Q_i = 2K_i$). This state has the same symmetry properties as the ME loop current phase discussed in Ref. [110]. (b) ME Loop current state introduced in Ref. [110]. Here the larger dark circles are Cu sites, the smaller circles are O sites, the arrows represent the direction of the current, and the arrow heads and tails give the direction of the magnetic moments induced by the currents.

become apparent in the analysis that follows). This state is depicted in Fig. 4.4(a). It shares the same symmetries as the ME loop current state shown in Fig. 4.4(b) which has been discussed in Refs. [110, 117]. Note that $\Delta_1 \neq \Delta_2$, however, as $\delta K_y = 0$, we recover the state examined in Ref. [102] for which $\Delta_1 = \Delta_2$, so for sufficiently small δK_y , we expect that $\Delta_1 \approx \Delta_2$. To carry out an analysis of this phase, we follow the approach used in Section 4.5 for orthorhombic symmetry. In particular, we re-write the free energy terms denoted by β_1 to β_7 as squares of basis functions of irreducible invariants for tetragonal symmetry. This allows for a straightforward HS transformation. While we can also introduce HS fields for the terms β_{ci} , for the loop current phases we are interested in, these fields vanish (as they did in the orthorhombic case), consequently, we will not include these terms in the following. To reformulate the quartic portion of the effective action, we set $l_i = |\Delta_{Q_i}|^2 - |\Delta_{-Q_i}|^2$

and $\epsilon_i = |\Delta_{\mathbf{Q}_i}|^2 + |\Delta_{-\mathbf{Q}_i}|^2$. Basis functions for irreducible representations of D_{4h} are then $p_{1x} = -l_3 - l_4$, $p_{1y} = l_1 + l_2$, $p_{2x} = l_1 - l_2$, $p_{2y} = l_3 - l_4$ (\mathbf{p}_1 and \mathbf{p}_2 are both bases for the E_u representation), $\psi = \sum_i \epsilon_i$ (corresponding to the A_{1g} representation), $\gamma = \epsilon_1 - \epsilon_2 + \epsilon_3 - \epsilon_4$ (corresponding to the A_{2g} representation), $\epsilon_{x^2-y^2} = \epsilon_1 + \epsilon_2 - \epsilon_3 - \epsilon_4$ (corresponding to the B_{1g} representation), $\epsilon_{xy} = \epsilon_1 - \epsilon_2 - \epsilon_3 + \epsilon_4$ (corresponding to the B_{2g} representation). In terms of these basis functions Eq. (4.4) can be rewritten:

$$\begin{aligned}
S_{0,\text{hom}} = r_0 \sum_i & |\Delta_{\mathbf{Q}_i}|^2 + \tilde{\beta}_1 \psi^2 + \tilde{\beta}_2 \mathbf{p}_1^2 + \tilde{\beta}_3 \mathbf{p}_2^2 + \tilde{\beta}_4 \mathbf{p}_1 \cdot \mathbf{p}_2 \\
& + \tilde{\beta}_5 \gamma^2 + \tilde{\beta}_6 \epsilon_{x^2-y^2}^2 + \tilde{\beta}_7 \epsilon_{xy}^2 \\
& + \beta_{c_1} \{ [\Delta_{\mathbf{Q}_1} \Delta_{-\mathbf{Q}_1} (\Delta_{\mathbf{Q}_2} \Delta_{-\mathbf{Q}_2})^* + \Delta_{\mathbf{Q}_3} \Delta_{-\mathbf{Q}_3} (\Delta_{\mathbf{Q}_4} \Delta_{-\mathbf{Q}_4})^*] + c.c. \} \\
& + \beta_{c_2} \{ [\Delta_{\mathbf{Q}_1} \Delta_{-\mathbf{Q}_1} (\Delta_{\mathbf{Q}_3} \Delta_{-\mathbf{Q}_3})^* + \Delta_{\mathbf{Q}_2} \Delta_{-\mathbf{Q}_2} (\Delta_{\mathbf{Q}_4} \Delta_{-\mathbf{Q}_4})^*] + c.c. \} \\
& + \beta_{c_3} \{ [\Delta_{\mathbf{Q}_1} \Delta_{-\mathbf{Q}_1} (\Delta_{\mathbf{Q}_4} \Delta_{-\mathbf{Q}_4})^* + \Delta_{\mathbf{Q}_2} \Delta_{-\mathbf{Q}_2} (\Delta_{\mathbf{Q}_3} \Delta_{-\mathbf{Q}_3})^*] + c.c. \}, \quad (4.13)
\end{aligned}$$

where $\tilde{\beta}_1 = \beta_1 + (1/8)(\beta_4 + \beta_6 + \beta_7 - \beta_2)$, $\tilde{\beta}_2 = (1/8)(\beta_3 - \beta_2 - \beta_7)$, $\tilde{\beta}_3 = (1/8)(\beta_7 - \beta_2 - \beta_3)$, $\tilde{\beta}_4 = (1/4)(\beta_6 - \beta_5)$, $\tilde{\beta}_5 = (1/8)(\beta_4 - \beta_3 - \beta_6)$, $\tilde{\beta}_6 = (\beta_2/4) + (1/8)(\beta_3 - \beta_4 - \beta_6)$, $\tilde{\beta}_7 = (1/8)(\beta_2 + \beta_6 - \beta_4 - \beta_7)$. In the above expression, all terms except β_{c_i} and $\tilde{\beta}_4$ are squares of basis functions. To account for $\tilde{\beta}_4$, we rotate $l_{1i} = \cos \theta p_{1i} + \sin \theta p_{2i}$ and $l_{2i} = -\sin \theta p_{1i} + \cos \theta p_{2i}$ with $\cos \theta = \frac{\sqrt{(\tilde{\beta}_2 - \tilde{\beta}_3 + \sqrt{(\tilde{\beta}_2 - \tilde{\beta}_3)^2 + \tilde{\beta}_4^2})^2 + \tilde{\beta}_4^2}}{2\sqrt{(\tilde{\beta}_2 - \tilde{\beta}_3)^2 + \tilde{\beta}_4^2}}$ and $\sin \theta = \frac{\sqrt{(\tilde{\beta}_2 - \tilde{\beta}_3 - \sqrt{(\tilde{\beta}_2 - \tilde{\beta}_3)^2 + \tilde{\beta}_4^2})^2 + \tilde{\beta}_4^2}}{2\sqrt{(\tilde{\beta}_2 - \tilde{\beta}_3)^2 + \tilde{\beta}_4^2}}$. In terms of these new parameters Eq. (4.13) can be expressed as ($\tilde{\beta}$'s and λ 's have been rescaled by a factor of half for convenience)

$$\begin{aligned}
S_{0,\text{hom}} = r_0 \sum_i & |\Delta_{\mathbf{Q}_i}|^2 + \frac{\tilde{\beta}_1}{2} \psi^2 + \frac{\lambda_1}{2} (l_{1x}^2 + l_{1y}^2) + \frac{\lambda_2}{2} (l_{2x}^2 + l_{2y}^2) \\
& + \frac{\tilde{\beta}_5}{2} \gamma^2 + \frac{\tilde{\beta}_6}{2} \epsilon_{x^2-y^2}^2 + \frac{\tilde{\beta}_7}{2} \epsilon_{xy}^2 \\
& + \beta_{c_1} \{ [\Delta_{\mathbf{Q}_1} \Delta_{-\mathbf{Q}_1} (\Delta_{\mathbf{Q}_2} \Delta_{-\mathbf{Q}_2})^* + \Delta_{\mathbf{Q}_3} \Delta_{-\mathbf{Q}_3} (\Delta_{\mathbf{Q}_4} \Delta_{-\mathbf{Q}_4})^*] + c.c. \} \\
& + \beta_{c_2} \{ [\Delta_{\mathbf{Q}_1} \Delta_{-\mathbf{Q}_1} (\Delta_{\mathbf{Q}_3} \Delta_{-\mathbf{Q}_3})^* + \Delta_{\mathbf{Q}_2} \Delta_{-\mathbf{Q}_2} (\Delta_{\mathbf{Q}_4} \Delta_{-\mathbf{Q}_4})^*] + c.c. \} \\
& + \beta_{c_3} \{ [\Delta_{\mathbf{Q}_1} \Delta_{-\mathbf{Q}_1} (\Delta_{\mathbf{Q}_4} \Delta_{-\mathbf{Q}_4})^* + \Delta_{\mathbf{Q}_2} \Delta_{-\mathbf{Q}_2} (\Delta_{\mathbf{Q}_3} \Delta_{-\mathbf{Q}_3})^*] + c.c. \}
\end{aligned}$$

$$\begin{aligned}
&= r_0 \sum_i |\Delta_{\mathbf{Q}_i}|^2 + \frac{\tilde{\beta}_1}{2} \left(\sum_i |\Delta_{\mathbf{Q}_i}|^2 \right)^2 \\
&\quad + \frac{\lambda_1}{2} [(-|\Delta_{\mathbf{Q}_3}|^2 + |\Delta_{-\mathbf{Q}_3}|^2 - |\Delta_{\mathbf{Q}_4}|^2 + |\Delta_{-\mathbf{Q}_4}|^2) \cos \theta \\
&\quad\quad + (|\Delta_{\mathbf{Q}_1}|^2 - |\Delta_{-\mathbf{Q}_1}|^2 - |\Delta_{\mathbf{Q}_2}|^2 + |\Delta_{-\mathbf{Q}_2}|^2) \sin \theta]^2 \\
&\quad + \frac{\lambda_1}{2} [(|\Delta_{\mathbf{Q}_1}|^2 - |\Delta_{-\mathbf{Q}_1}|^2 + |\Delta_{\mathbf{Q}_2}|^2 - |\Delta_{-\mathbf{Q}_2}|^2) \cos \theta \\
&\quad\quad + (|\Delta_{\mathbf{Q}_3}|^2 - |\Delta_{-\mathbf{Q}_3}|^2 - |\Delta_{\mathbf{Q}_4}|^2 + |\Delta_{-\mathbf{Q}_4}|^2) \sin \theta]^2 \\
&\quad + \frac{\lambda_2}{2} [(|\Delta_{\mathbf{Q}_3}|^2 - |\Delta_{-\mathbf{Q}_3}|^2 + |\Delta_{\mathbf{Q}_4}|^2 - |\Delta_{-\mathbf{Q}_4}|^2) \sin \theta \\
&\quad\quad + (|\Delta_{\mathbf{Q}_1}|^2 - |\Delta_{-\mathbf{Q}_1}|^2 - |\Delta_{\mathbf{Q}_2}|^2 + |\Delta_{-\mathbf{Q}_2}|^2) \cos \theta]^2 \\
&\quad + \frac{\lambda_2}{2} [(-|\Delta_{\mathbf{Q}_1}|^2 + |\Delta_{-\mathbf{Q}_1}|^2 - |\Delta_{\mathbf{Q}_2}|^2 + |\Delta_{-\mathbf{Q}_2}|^2) \sin \theta \\
&\quad\quad + (|\Delta_{\mathbf{Q}_3}|^2 - |\Delta_{-\mathbf{Q}_3}|^2 - |\Delta_{\mathbf{Q}_4}|^2 + |\Delta_{-\mathbf{Q}_4}|^2) \cos \theta]^2 \\
&\quad + \frac{\tilde{\beta}_5}{2} (|\Delta_{\mathbf{Q}_1}|^2 + |\Delta_{-\mathbf{Q}_1}|^2 - |\Delta_{\mathbf{Q}_2}|^2 - |\Delta_{-\mathbf{Q}_2}|^2 \\
&\quad\quad + |\Delta_{\mathbf{Q}_3}|^2 + |\Delta_{-\mathbf{Q}_3}|^2 - |\Delta_{\mathbf{Q}_4}|^2 - |\Delta_{-\mathbf{Q}_4}|^2)^2 \\
&\quad + \frac{\tilde{\beta}_6}{2} (|\Delta_{\mathbf{Q}_1}|^2 + |\Delta_{-\mathbf{Q}_1}|^2 + |\Delta_{\mathbf{Q}_2}|^2 + |\Delta_{-\mathbf{Q}_2}|^2 \\
&\quad\quad - |\Delta_{\mathbf{Q}_3}|^2 - |\Delta_{-\mathbf{Q}_3}|^2 - |\Delta_{\mathbf{Q}_4}|^2 - |\Delta_{-\mathbf{Q}_4}|^2)^2 \\
&\quad + \frac{\tilde{\beta}_7}{2} (|\Delta_{\mathbf{Q}_1}|^2 + |\Delta_{-\mathbf{Q}_1}|^2 - |\Delta_{\mathbf{Q}_2}|^2 - |\Delta_{-\mathbf{Q}_2}|^2 \\
&\quad\quad - |\Delta_{\mathbf{Q}_3}|^2 - |\Delta_{-\mathbf{Q}_3}|^2 + |\Delta_{\mathbf{Q}_4}|^2 + |\Delta_{-\mathbf{Q}_4}|^2)^2 \\
&\quad + \beta_{c_1} \{ [\Delta_{\mathbf{Q}_1} \Delta_{-\mathbf{Q}_1} (\Delta_{\mathbf{Q}_2} \Delta_{-\mathbf{Q}_2})^* + \Delta_{\mathbf{Q}_3} \Delta_{-\mathbf{Q}_3} (\Delta_{\mathbf{Q}_4} \Delta_{-\mathbf{Q}_4})^*] + c.c. \} \\
&\quad + \beta_{c_2} \{ [\Delta_{\mathbf{Q}_1} \Delta_{-\mathbf{Q}_1} (\Delta_{\mathbf{Q}_3} \Delta_{-\mathbf{Q}_3})^* + \Delta_{\mathbf{Q}_2} \Delta_{-\mathbf{Q}_2} (\Delta_{\mathbf{Q}_4} \Delta_{-\mathbf{Q}_4})^*] + c.c. \} \\
&\quad + \beta_{c_3} \{ [\Delta_{\mathbf{Q}_1} \Delta_{-\mathbf{Q}_1} (\Delta_{\mathbf{Q}_4} \Delta_{-\mathbf{Q}_4})^* + \Delta_{\mathbf{Q}_2} \Delta_{-\mathbf{Q}_2} (\Delta_{\mathbf{Q}_3} \Delta_{-\mathbf{Q}_3})^*] + c.c. \}, \quad (4.14)
\end{aligned}$$

where $\lambda_1 = \frac{\tilde{\beta}_2 + \tilde{\beta}_3 + \sqrt{(\tilde{\beta}_2 - \tilde{\beta}_3)^2 + \tilde{\beta}_4^2}}{2}$ and $\lambda_2 = \frac{\tilde{\beta}_2 + \tilde{\beta}_3 - \sqrt{(\tilde{\beta}_2 - \tilde{\beta}_3)^2 + \tilde{\beta}_4^2}}{2}$. Notice that if $\lambda_1 < 0$, β_{c_i} are sufficiently small, and all other quartic terms are positive, then the ME loop current phase will be the mean-field ground state. This is the limit that we will examine further. In particular, in the next paragraph, we examine preemptive loop current order emerging from this ME PDW phase.

We decouple the quartic terms of Eq. (4.14) through HS transformations. In particular, introducing ψ , l_{1x} , l_{1y} , l_{2x} , l_{2y} , γ , $\epsilon_{x^2-y^2}$ and ϵ_{xy} to decouple the second $((\sum_i |\Delta_i|^2)^2)$, third, fourth, fifth, sixth, seventh, eighth and ninth term respectively. The resultant action is quadratic in fields $\Delta_{\mathbf{Q}_i}$ and these fields can be integrated out. As in the orthorhombic case, the terms with β_{c_i} do not contribute to the effective action in the ME PDW phase, so we ignore these terms (HS decomposition of these terms can proceed through charge-4e superconducting fields, ignoring these terms is equivalent to setting these fields to zero). The remaining fields have discrete symmetries, so it is reasonable to treat these at a mean-field level. This leads to the following effective action (note we have set $\lambda_1 < 0$ and all other quartic terms are positive)

$$\begin{aligned} \frac{S_{\text{eff,tet}}}{A} &= \frac{l_{1x}^2 + l_{1y}^2}{2|\lambda_1|} - \frac{l_{2x}^2 + l_{2y}^2}{2\lambda_2} - \frac{\psi^2}{2\tilde{\beta}_1} - \frac{\gamma^2}{2\tilde{\beta}_5} - \frac{\epsilon_{x^2-y^2}^2}{2\tilde{\beta}_6} - \frac{\epsilon_{xy}^2}{2\tilde{\beta}_7} \\ &+ \int \frac{d^2q}{4\pi^2} \ln [(\chi_{1,\mathbf{q}}^{-1} + \gamma + \epsilon_{x^2-y^2} + \epsilon_{xy} - l_{1x} \sin \theta - l_{1y} \cos \theta + l_{2x} \cos \theta - l_{2y} \sin \theta) \\ &\quad (\chi_{1,\mathbf{q}}^{-1} + \gamma + \epsilon_{x^2-y^2} + \epsilon_{xy} + l_{1x} \sin \theta + l_{1y} \cos \theta - l_{2x} \cos \theta + l_{2y} \sin \theta) \\ &\quad (\chi_{2,\mathbf{q}}^{-1} - \gamma + \epsilon_{x^2-y^2} - \epsilon_{xy} + l_{1x} \sin \theta - l_{1y} \cos \theta - l_{2x} \cos \theta - l_{2y} \sin \theta) \\ &\quad (\chi_{2,\mathbf{q}}^{-1} - \gamma + \epsilon_{x^2-y^2} - \epsilon_{xy} - l_{1x} \sin \theta + l_{1y} \cos \theta + l_{2x} \cos \theta + l_{2y} \sin \theta) \\ &\quad (\chi_{3,\mathbf{q}}^{-1} + \gamma - \epsilon_{x^2-y^2} - \epsilon_{xy} + l_{1x} \cos \theta - l_{1y} \sin \theta + l_{2x} \sin \theta + l_{2y} \cos \theta) \\ &\quad (\chi_{3,\mathbf{q}}^{-1} + \gamma - \epsilon_{x^2-y^2} - \epsilon_{xy} - l_{1x} \cos \theta + l_{1y} \sin \theta - l_{2x} \sin \theta - l_{2y} \cos \theta) \\ &\quad (\chi_{4,\mathbf{q}}^{-1} - \gamma - \epsilon_{x^2-y^2} + \epsilon_{xy} + l_{1x} \cos \theta + l_{1y} \sin \theta + l_{2x} \sin \theta - l_{2y} \cos \theta) \\ &\quad (\chi_{4,\mathbf{q}}^{-1} - \gamma - \epsilon_{x^2-y^2} + \epsilon_{xy} - l_{1x} \cos \theta - l_{1y} \sin \theta - l_{2x} \sin \theta + l_{2y} \cos \theta)], \quad (4.15) \end{aligned}$$

where $\chi_{1,\mathbf{q}}^{-1} = r_0 + \psi + \kappa_1(q_x^2 + q_y^2) + \kappa_2(q_x^2 - q_y^2) + 2\kappa_3q_xq_y$, $\chi_{2,\mathbf{q}}^{-1} = r_0 + \psi + \kappa_1(q_x^2 + q_y^2) + \kappa_2(q_x^2 - q_y^2) - 2\kappa_3q_xq_y$, $\chi_{3,\mathbf{q}}^{-1} = r_0 + \psi + \kappa_1(q_x^2 + q_y^2) - \kappa_2(q_x^2 - q_y^2) - 2\kappa_3q_xq_y$, and $\chi_{4,\mathbf{q}}^{-1} = r_0 + \psi + \kappa_1(q_x^2 + q_y^2) - \kappa_2(q_x^2 - q_y^2) + 2\kappa_3q_xq_y$.

To carry out the integrals, the anisotropy in $\chi_{i,\mathbf{q}}^{-1}$ due to κ_2 and κ_3 , can again be removed by rotating and re-scaling q_x and q_y , yielding $(\tilde{q}_x^2 + \tilde{q}_y^2)/\tilde{\kappa}$ with $\tilde{\kappa} =$

$\sqrt{\kappa_1^2 - \kappa_2^2 - \kappa_3^2}$. We find the self-consistency equations by setting the first derivatives with respect to the field equal to zero. The relevant solution that minimizes the action satisfies $\gamma = 0$, $\epsilon_{x^2-y^2} = 0$, $l_{1x} = l_{1y} \equiv l_1$ and $l_{2x} = l_{2y} \equiv l_2$ and the self consistency equations become (here $r = r_0 + \psi$ and $\bar{r}_0 = r_0 + (4\tilde{\beta}_1/\pi\tilde{\kappa}) \ln \Lambda$)

$$r = \bar{r}_0 - \frac{8\tilde{\beta}_1}{\pi\tilde{\kappa}} \ln \left\{ [(r + \epsilon_{xy})^2 - (\ell_1 \cos \theta + \ell_1 \sin \theta + \ell_2 \sin \theta - \ell_2 \cos \theta)^2] \right. \\ \left. [(r - \epsilon_{xy})^2 - (\ell_1 \cos \theta - \ell_1 \sin \theta + \ell_2 \sin \theta + \ell_2 \cos \theta)^2] \right\}, \quad (4.16)$$

$$\epsilon_{xy} = -\frac{\tilde{\beta}_7}{4\pi\tilde{\kappa}} \left\{ \ln \left[\frac{(r + \epsilon_{xy})^2 - (\ell_1 \sin \theta + \ell_1 \cos \theta - \ell_2 \cos \theta + \ell_2 \sin \theta)^2}{(r - \epsilon_{xy})^2 - (\ell_1 \cos \theta - \ell_1 \sin \theta + \ell_2 \sin \theta + \ell_2 \cos \theta)^2} \right] \right. \\ \left. + \ln \left[\frac{(r + \epsilon_{xy})^2 - (\ell_1 \cos \theta + \ell_1 \sin \theta + \ell_2 \sin \theta - \ell_2 \cos \theta)^2}{(r - \epsilon_{xy})^2 - (\ell_1 \sin \theta - \ell_1 \cos \theta - \ell_2 \cos \theta - \ell_2 \sin \theta)^2} \right] \right\}, \quad (4.17)$$

$$\ell_1 = \frac{|\lambda_1|}{4\pi\tilde{\kappa}} \left\{ \cos \theta \ln \left[\frac{(r + \ell_1 \cos \theta + \ell_2 \sin \theta)^2 - (\epsilon_{xy} + \ell_1 \sin \theta - \ell_2 \cos \theta)^2}{(r - \ell_1 \cos \theta - \ell_2 \sin \theta)^2 - (\epsilon_{xy} - \ell_1 \sin \theta + \ell_2 \cos \theta)^2} \right] \right. \\ \left. + \sin \theta \ln \left[\frac{(r + \ell_1 \sin \theta - \ell_2 \cos \theta)^2 - (\epsilon_{xy} + \ell_1 \cos \theta + \ell_2 \sin \theta)^2}{(r - \ell_1 \sin \theta + \ell_2 \cos \theta)^2 - (\epsilon_{xy} - \ell_1 \cos \theta - \ell_2 \sin \theta)^2} \right] \right\}, \quad (4.18)$$

$$\ell_2 = -\frac{\lambda_2}{4\pi\tilde{\kappa}} \left\{ \cos \theta \ln \left[\frac{(r - \ell_1 \sin \theta + \ell_2 \cos \theta)^2 - (\epsilon_{xy} - \ell_1 \cos \theta - \ell_2 \sin \theta)^2}{(r + \ell_1 \sin \theta - \ell_2 \cos \theta)^2 - (\epsilon_{xy} + \ell_1 \cos \theta + \ell_2 \sin \theta)^2} \right] \right. \\ \left. + \sin \theta \ln \left[\frac{(r + \ell_1 \cos \theta + \ell_2 \sin \theta)^2 - (\epsilon_{xy} + \ell_1 \sin \theta - \ell_2 \cos \theta)^2}{(r - \ell_1 \cos \theta - \ell_2 \sin \theta)^2 - (\epsilon_{xy} - \ell_1 \sin \theta + \ell_2 \cos \theta)^2} \right] \right\}. \quad (4.19)$$

To address whether or not there can be a second order transition into a phase with loop current order, we expand in powers of ℓ_1 . To cubic order in ℓ_1 we find

$$\epsilon_{xy} = -\frac{\tilde{\beta}_7^*}{2(2\tilde{\beta}_7^* + r)r} [4 \cos 2\theta \ell_1 \ell_2 + 2 \sin 2\theta (-\ell_1^2 + \ell_2^2)], \quad (4.20)$$

$$\ell_2 \sim \mathcal{O}(\ell_1^3), \quad (4.21)$$

$$4r^2(r - |\lambda_1^*|)\ell_1 = -4|\lambda_1^*| \frac{\tilde{\beta}_7^*}{2(2\tilde{\beta}_7^* + r)} \sin^2 2\theta \ell_1^3 - \frac{2}{3} |\lambda_1^*| (\cos 4\theta - 3) \ell_1^3, \quad (4.22)$$

where * denotes that the coefficients are scaled by $\pi\tilde{\kappa}$. Thus to leading order in ℓ_1 , $r = |\lambda_1^*|$. Going to next higher order, let $r = r_{\delta=0} + \delta = |\lambda_1^*| + \delta$ where δ is small correction such that $(\delta/|\lambda_1^*| \ll 1)$, then the previous equation becomes

$$\frac{\delta}{|\lambda_1^*|} = \left(-\frac{\alpha_7}{2\alpha_7 + 1} + \frac{1}{6} \right) \sin^2 2\theta \ell_1^{*2} - \frac{1}{6} \cos^2 2\theta \ell_1^{*2} + \frac{1}{2} \ell_1^{*2} \quad (4.23)$$

and Eq. (4.16) leads to

$$\bar{r}_0 = 1 + (1 + 32\alpha_1) \frac{\delta}{|\lambda_1^*|} - 16\alpha_1 \ell_1^{*2}, \quad (4.24)$$

where $\bar{r}_0 = (\bar{r}_0/|\lambda_1^*|) - 32\alpha_1 \ln |\lambda_1^*|$, $\alpha_1 = \tilde{\beta}_1/|\lambda_1|$, $\alpha_7 = \tilde{\beta}_7/|\lambda_1|$ and $\ell_1^* = \ell_1/|\lambda_1^*|$. Eliminating δ between Eqs. (4.23) and (4.24), we obtain

$$\bar{r}_0 = 1 + (1 + 32\alpha_1) \left[\left(-\frac{\alpha_7}{1 + 2\alpha_7} + \frac{1}{6} \right) \sin^2 2\theta - \frac{1}{6} \cos^2 2\theta \right] \ell_1^{*2} + \frac{1}{2} \ell_1^{*2}. \quad (4.25)$$

Equation (4.25) shows that a local maximum $\bar{r}_0 = 1$ occurs if the quadratic term in ℓ_1^* is negative. Since \bar{r}_0 is monotonically increasing with temperature, this maximum gives the highest possible transition temperature (provided there are no other local maxima at higher \bar{r}_0 – here we note that no such maxima occurred in a related model [111]) and the corresponding transition is second order. However, if the quadratic term in ℓ_1^* is positive, then the largest value of \bar{r}_0 will occur at non-zero ℓ_1^* , indicating a first order transition. This emergent loop current phase shares the same symmetry properties as the ME loop current state discussed in Refs. [110, 117]. While such a

phase captures much of the physics associated with broken time-reversal symmetry, it does not provide a complete explanation of all the signatures of broken time-reversal symmetry in the pseudogap phase [113]. We address this in the next section.

4.7 Tilted loop current order

It has been argued that the Kerr effect [69, 118] is zero for the ME loop current state discussed above and a non-vanishing Kerr effect requires additional physics (such as a structural transition [119] or ordering along the c -axis). This has been discussed in detail by Yakovenko [113] and he has identified a modified loop current state consistent with all experiments of broken time-reversal symmetry. This tilted loop

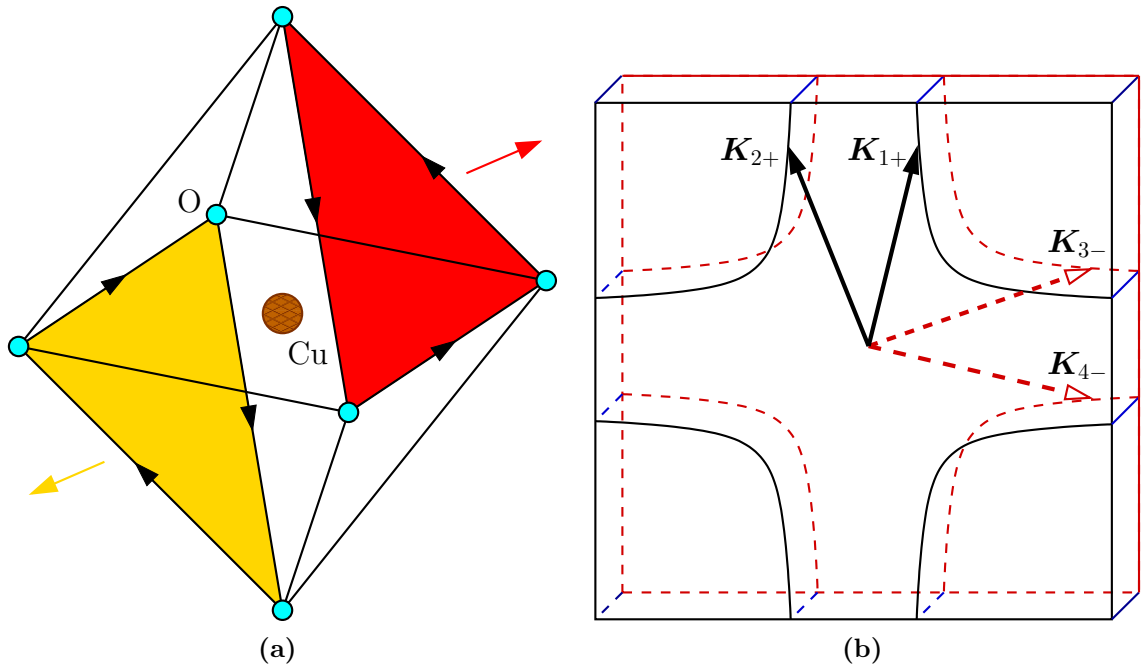


Figure 4.5: (a) Tilted loop current state proposed by Yakovenko [113]. The arrows on the bonds depict the direction of the current, the longer arrows depict the associated magnetic moments. (b) PDW state with the same symmetry properties as the tilted loop current state. The arrows \mathbf{K}_i depict the non-zero components of the PDW order parameter. Wavevectors labeled “+” (black arrows) are above the x - y plane and those labeled “-” (red arrows) are below the x - y plane.

current state is shown in Fig. 4.5(a). It is possible to find a PDW state that shares the same symmetry properties as the tilted loop current state (once the SC and CDW orders are removed through fluctuations). The simplest way to find such a state is to allow for the pairing momenta to have a c -axis component. The corresponding PDW order parameter has sixteen complex degrees of freedom (eight for momenta $\mathbf{Q}_i + Q_z \hat{z}$ and eight for PDW momenta $\mathbf{Q}_i - Q_z \hat{z}$ where the \mathbf{Q}_i are the momenta considered in Section 4.6). Here we do not present a complete analysis of this order parameter. However, it is possible to show that the state depicted in Fig. 4.5(b) is a mean-field ground state and thus represents a viable order parameter. In this state only four of the PDW momenta have non-zero order parameter components. As depicted in Fig. 4.5(b), two of these momenta lie below the x - y plane and two lie above the x - y plane. When the SC and CDW order are removed through fluctuations, this state will have the same symmetry properties as the tilted loop-current phase and is therefore also consistent with all existing experiments that show broken time-reversal symmetry.

4.8 Quasiparticle properties of loop current PDW phases

In this section we examine whether the broken time-reversal symmetric PDW states are consistent with ARPES measurements. Here we focus our analysis on the tetragonal ME PDW state discussed in Section 4.6 (qualitatively similar results will appear for the PDW state discussed in Section 4.7). To examine the qp properties, we consider the Hamiltonian

$$H = \sum_{\mathbf{k}, s} \epsilon_{\mathbf{k}} c_{\mathbf{k}s}^\dagger c_{\mathbf{k}s} + \sum_{\mathbf{Q}_i, \mathbf{k}} [\Delta_{\mathbf{Q}_i}(\mathbf{k}) c_{\mathbf{k} + \frac{\mathbf{Q}_i}{2}, \uparrow}^\dagger c_{-\mathbf{k} + \frac{\mathbf{Q}_i}{2}, \downarrow}^\dagger + h.c.], \quad (4.26)$$

where $c_{\mathbf{k}s}$ is the fermion destruction operator with momentum \mathbf{k} and spin s , $\epsilon_{\mathbf{k}}$ is the bare dispersion, and $h.c.$ means Hermitian conjugate. We compute the eigenstates of Eq. (4.26) and the spectral weight using

$$I(\omega, \mathbf{k}) = \text{Im} \sum_{\alpha} \frac{|u_{\alpha, \mathbf{k}}|^2}{\omega - E_{\alpha, \mathbf{k}} - i\Gamma}, \quad (4.27)$$

where $E_{\alpha, \mathbf{k}}$ are the eigenenergies of Eq. (4.26), $u_{\alpha, \mathbf{k}}$ is the weight of the fermion with momentum \mathbf{k} in the band α , and the damping factor Γ models short-range order in the PDW phase. In our calculations we use the bare dispersion $\epsilon_{\mathbf{k}}$ given in Ref. [70] and set $\Gamma = 0.1$ eV. In addition, we set $\Delta_{Q_i}(\mathbf{k}) = \Delta_i f_i(\mathbf{k} - \mathbf{K}_i)$ which localizes the pairing in \mathbf{k} space as described in [102] (for Δ_{Q_1} , $f_1(\mathbf{k} - \mathbf{K}_1) = e^{-(k_y - K_y)^2/k_0^2}$, the other f_i are determined by tetragonal symmetry). Figures 4.6(a) and 4.6(b) show the bands weighted by a factor $|u_{\alpha, \mathbf{k}}|^2$ for fixed $k_y = \pi$ and $k_y = \pi - 0.7$ as a function of k_x (with $\Delta_1 = \Delta_2$). These first two figures show that the Fermi arc results from occupied states moving towards the Fermi level, a point emphasized in Ref. [102]. In Fig. 4.6(c) we illustrate the role of $\Delta_1 \neq \Delta_2$. Notice that the ARPES bands become asymmetric about $k_x = 0$. This asymmetry is consistent with existing ARPES measurements and

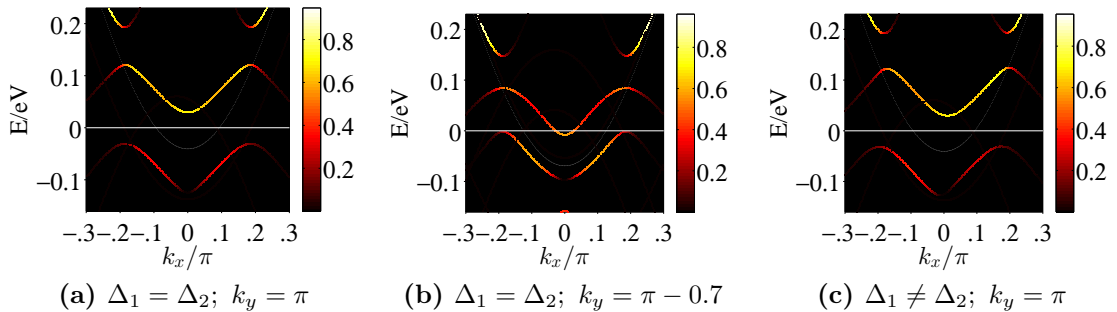


Figure 4.6: Quasiparticle spectrum for the ME PDW state with $\delta K_y = 0.1$. Shown are the bare electron dispersion (the white parabola) and the PDW bands weighted by $|u(k)|^2$ (the negative energy portion is observable by ARPES). (a) $\Delta_1 = \Delta_2 = 75$ meV and $k_y = \pi$. (b) $\Delta_1 = \Delta_2 = 75$ meV and $k_y = \pi - 0.7$, here occupied bands have moved up to ϵ_F to create the Fermi arcs. (c) $\Delta_1 = 85$ meV, $\Delta_2 = 65$ meV, and $k_y = \pi$. Notice the asymmetry in k_x about $k_x = 0$. [The spectra was calculated by Drew S. Melchert]

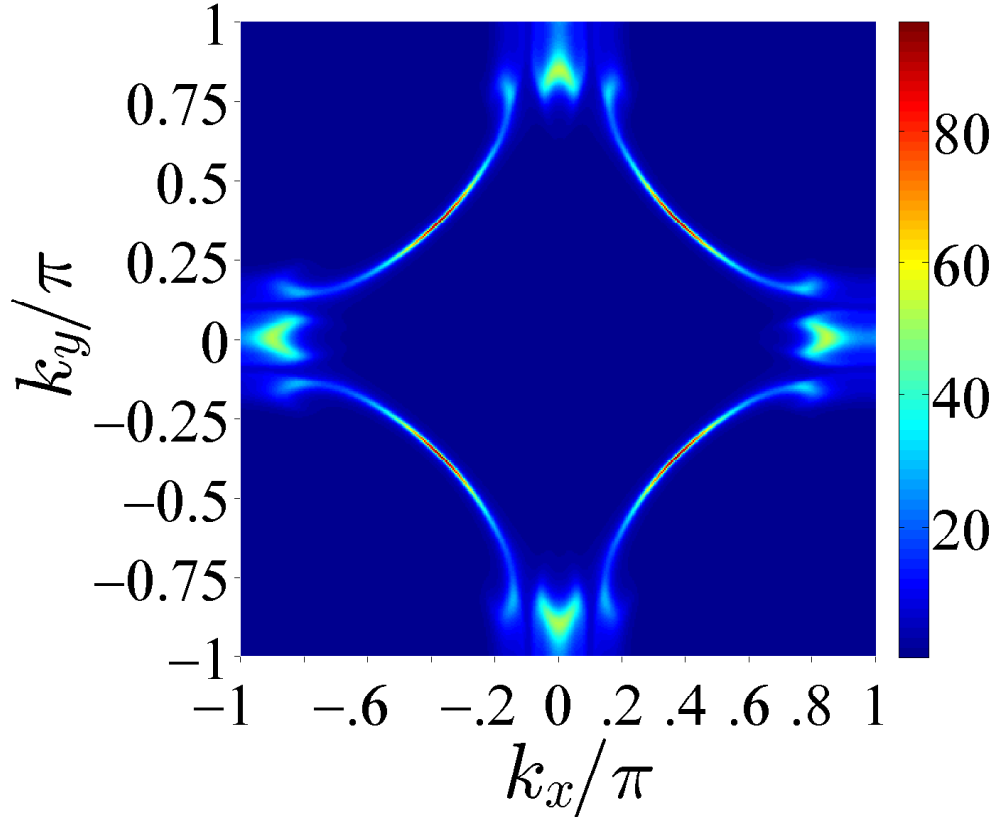


Figure 4.7: Spectral weight showing Fermi arcs for ME PDW state. Here $\Delta_1 = \Delta_2 = 75$ meV and $\Gamma = 10$ meV. [The spectral weight map was calculated by Drew S. Melchert]

it would be of interest to examine this experimentally. We note that this asymmetry does not exist in the PDW phase proposed in Ref. [102]. Fig. 4.7 shows the spectral weight for $\Delta_1 = \Delta_2 = 75$ meV revealing the Fermi arcs.

4.9 Conclusions

PDW order has earlier been proposed to account for the SC correlations and CDW order in pseudogap phase in cuprates. Also proposals for translational invariant loop current orders already exist to account for broken time reversal in pseudogap phase. This work shows that PDW order naturally induces what we call ME loop current order parameter as secondary order parameter, which has the same symmetry

properties as existing proposals. ME loop current order parameter is translational invariant. It breaks both time-reversal and parity symmetries, but is invariant under the product of the two. This translational invariant ME loop current order parameter can account for the signatures of broken time-reversal like intracell magnetic order and Kerr effect.

We have shown that for both orthorhombic and tetragonal pairing symmetries, there exist a mean-field PDW ground state with ME loop current order that accounts for CDW order at observed wave vectors, intracell magnetic order and SC correlations. Going further, we restored the continuous symmetries by including the fluctuations associated with $U(1)$ degeneracies in the GLW action using a Hubbard-Stratonovich transformation. This allows for a state with emergent long-range ME loop current order coexisting with short range SC and CDW correlations, which agrees with the observation that $T_{\text{mag}} \approx T^*$, where T_{mag} is the temperature at which intracell magnetic order appears and T^* is pseudogap temperature.

We have also identified a state, by including c -axis component to the pairing momenta, that has the same symmetry properties as Yakovenko's loop current order which can account for Kerr effect. Since experiments reveal that Kerr temperature T_{Kerr} is lower than T^* ($\approx T_{\text{mag}}$) [68, 119], we propose that as temperature is lowered initially only the c -component of the magnetic order (in-plane loop current order) sets in near T^* and then on further decreasing the temperature somehow the pairing correlations along the c -axis become active leading to in-plane component of the magnetic order (in addition to c -axis component) and Kerr effect. This proposal is further bolstered by the observation that at T_{mag} only the c -component of the magnetic order appears and the in-plane component appears only when temperature is further reduced [120].

The ME loop current ground state considered here, for tetragonal symmetry, is shown to have compliance with the ARPES data. In particular, not only does it lead

to Fermi arcs but it also agrees with the observation that Fermi arcs are produced by occupied states moving up (from below the Fermi energy) as you go from antinodal region to nodal region. This cannot be explained by considering charge order as the primary order because Fermi arcs in that case are theoretically shown to be produced by occupied states moving down [102] as you go from antinodal region to nodal region. Our theoretical model also results in an asymmetry in the magnitude of the minimum gap wavevectors on the two side of the zero of the axis (see Fig. 4.6(c)). Such an observation is consistent with the existing ARPES data [70] though it has been attributed to experimental artifact. In light of our prediction, it would be interesting to further examine it experimentally.

In essence, the work produced here explains all observations of broken symmetries in the pseudogap phase of cuprates within a single theory.

References

- [1] R. de Bruyn Ouboter, *Scientific American* **276**, 98 (1997).
- [2] D. van Delft and P. Kes, *Physics Today* **63**, 38 (2010).
- [3] D. Goodstein and J. Goodstein, *Phys. perspect.* **2**, 30 (2000).
- [4] H. Kamelmingh Onnes, *Leiden Comm.* **120b**, **122b**, **124c** (1911).
- [5] W. Meissner and R. Ochsenfeld, *Naturwissenschaften* **21**, 787–788 (1933).
- [6] F. London and H. London, *Proc. Roy. Soc. (London)* **A149**, 71 (1935).
- [7] A. B. Pippard, *Proc. Roy. Soc. (London)* **A216**, 547 (1953).
- [8] J. Bardeen, L. N. Cooper, and J. R. Schrieffer, *Phys. Rev.* **106**, 162 (1957).
- [9] J. Bardeen, L. N. Cooper, and J. R. Schrieffer, *Phys. Rev.* **108**, 1175 (1957).
- [10] L. Cooper, *Phys. Rev.* **104**, 1189–1190 (1956).
- [11] M. Tinkham, *Introduction to Superconductivity*, 2nd ed. (Dover Publications, Inc., Mineola, New York, 2004).
- [12] V. P. Mineev and K. V. Samokhin, *Introduction to Unconventional Superconductivity* (Gordon and Breach Science Publishers, Amsterdam, 1999).
- [13] P. W. Anderson, *J. Phys. Chem. Solids* **11**, 26–30 (1959).
- [14] P. W. Anderson, *Phys. Rev. B* **30**, 4000–4002 (1984).
- [15] E. Bauer and M. Sigrist, eds., *Non-centrosymmetric Superconductors: Introduction and Overview* (Springer, Heidelberg, 2012) [Lecture Notes in Physics 847].
- [16] V. M. Edelstein, *Zh. Eksp. Teor. Fiz.* **95**, 2151 (1989), [*Sov. Phys. JETP* **68**,

- 1244 (1989)].
- [17] P. A. Frigeri, D. F. Agterberg, A. Koga, and M. Sigrist, *Phys. Rev. Lett.* **92**, 097001 (2004).
- [18] P. A. Frigeri, D. F. Agterberg, A. Koga, and M. Sigrist, *Phys. Rev. Lett.* **93**, 099903(E) (2004).
- [19] P. A. Frigeri, D. F. Agterberg, I. Milat, and M. Sigrist, *Eur. Phys. J. B* **54**, 435 (2006).
- [20] N. Hayashi, K. Wakabayashi, P. A. Frigeri, and M. Sigrist, *Phys. Rev. B* **73**, 092508 (2006).
- [21] H. Q. Yuan, D. F. Agterberg, N. Hayashi, P. Badica, D. Vandervelde, K. Togano, M. Sigrist, and M. B. Salamon, *Phys. Rev. Lett.* **97**, 017006 (2006).
- [22] A. P. Schnyder, P. M. R. Brydon, and C. Timm, *Phys. Rev. B* **85**, 024522 (2012).
- [23] L. P. Gor'kov and E. I. Rashba, *Phys. Rev. Lett.* **87**, 037004 (2001).
- [24] S. K. Yip, *Phys. Rev. B* **65**, 144508 (2002).
- [25] K. V. Samokhin, *Phys. Rev. Lett.* **94**, 027004 (2005).
- [26] P. A. Frigeri, D. F. Agterberg, and M. Sigrist, *New J. Phys.* **6**, 115 (2004).
- [27] K. V. Samokhin, *Phys. Rev. B* **78**, 224520 (2008).
- [28] R. P. Kaur, D. F. Agterberg, and M. Sigrist, *Phys. Rev. Lett.* **94**, 137002 (2005).
- [29] N. Kimura, K. Ito, H. Aoki, S. Uji, and T. Terashima, *Phys. Rev. Lett.* **98**, 197001 (2007).
- [30] V. Barzykin and L. P. Gor'kov, *Phys. Rev. Lett.* **89**, 227002 (2002).
- [31] D. F. Agterberg, *Physica C* **387**, 13 (2003).
- [32] O. Dimitrova and M. V. Feigel'man, *Phys. Rev. B* **76**, 014522 (2007).
- [33] K. Michaeli, A. C. Potter, and P. A. Lee, *Phys. Rev. Lett.* **108**, 117003 (2012).

- [34] L. S. Levitov, Y. V. Nazarov, and G. M. Eliashberg, *Pis'ma Zh. Eksp. Teor. Fiz.* **41**, 188 (1985), [*JETP Lett.* **41**, 228, (1985)].
- [35] V. M. Edelstein, *Phys. Rev. Lett.* **75**, 2004 (1995).
- [36] S. Fujimoto, *Phys. Rev. B* **72**, 024515 (2005).
- [37] C.-K. Lu and S. Yip, *Phys. Rev. B* **78**, 132502 (2008).
- [38] M. Oka, M. Ichioka, and K. Machida, *Phys. Rev. B* **73**, 214509 (2006).
- [39] S. K. Yip, *J. Low. Temp. Phys.* **140**, 67 (2005).
- [40] P. Badica, T. Kondo, and K. Togano, *J. Phys. Soc. Jpn.* **74**, 1014 (2005).
- [41] K. Togano, P. Badica, Y. Nakamori, S. Orimo, H. Takeya, and K. Hirata, *Phys. Rev. Lett.* **93**, 247004 (2004).
- [42] H. Takeya, K. Hirata, K. Yamaura, K. Togano, M. El Massalami, R. Rapp, F. A. Chaves, and B. Ouladdiaf, *Phys. Rev. B* **72** (2005), 10.1103/physrevb.72.104506.
- [43] P. Badica, T. Kondo, T. Kudo, Y. Nakamori, S. Orimo, and K. Togano, *Appl. Phys. Lett.* **85**, 4433 (2004).
- [44] J. Johnston, L. Toth, K. Kennedy, and E. R. Parker, *Solid State Commun.* **2**, 123 (1964).
- [45] A. B. Karki, Y. M. Xiong, I. Vekhter, D. Browne, P. W. Adams, D. P. Young, K. R. Thomas, J. Y. Chan, H. Kim, and R. Prozorov, *Phys. Rev. B* **82**, 064512 (2010).
- [46] E. Bauer, G. Rogl, X.-Q. Chen, R. T. Khan, H. Michor, G. Hilscher, E. Royanian, K. Kumagai, D. Z. Li, Y. Y. Li, R. Podloucky, and P. Rogl, *Phys. Rev. B* **82**, 064511 (2010).
- [47] M. Nishiyama, Y. Inada, and G.-q. Zheng, *Phys. Rev. B* **71** (2005), 10.1103/physrevb.71.220505.
- [48] M. Nishiyama, Y. Inada, and G.-q. Zheng, *Phys. Rev. Lett.* **98** (2007), 10.1103/physrevlett.98.047002.
- [49] C. N. Kuo, H. F. Liu, and C. S. Lue, *Phys. Rev. B* **85**, 052501 (2012).
- [50] J. Nagamatsu, N. Nakagawa, T. Muranaka, Y. Zenitani, and J. Akimitsu,

- Nature **410**, 63–64 (2001).
- [51] H. J. Choi, D. Roundy, H. Sun, M. L. Cohen, and S. G. Louie, Nature **418**, 758–760 (2002).
- [52] B. Keimer, S. A. Kivelson, M. R. Norman, S. Uchida, and Zaane, Nature **518**, 179–186 (2015).
- [53] M. K. Wu, J. R. Ashburn, C. J. Torng, P. H. Hor, R. L. Meng, L. Gao, Z. J. Huang, Y. Q. Wang, and C. W. Chu, Phys. Rev. Lett. **58**, 908–910 (1987).
- [54] S. Hikami, T. Hirai, and S. Kagoshima, Jpn. J. Appl. Phys. **26**, L314–L315 (1987).
- [55] Z. X. Zhao, L. Q. Chen, Q. S. Yang, Y. Z. Huang, G. H. Chen, R. M. Tang, G. R. Liu, C. G. Cui, L. Chen, L. G. Wang, S. Q. Guo, S. L. Li, and J. Q. Bi, Kexue Tongbao **33**, 661 (1987).
- [56] A. Schilling, M. Cantoni, J. D. Guo, and H. R. Ott, Nature **363**, 56–58 (1993).
- [57] L. Gao, Y. Y. Xue, F. Chen, Q. Xiong, R. L. Meng, D. Ramirez, C. W. Chu, J. H. Eggert, and H. K. Mao, Phys. Rev. B **50**, 4260–4263 (1994).
- [58] N. W. Ashcroft, Physical Review Letters **21**, 1748–1749 (1968).
- [59] A. P. Drozdov, M. I. Erements, and I. A. Troyan, (2014), arXiv:1412.0460v1 .
- [60] C. P. Poole, ed., *Handbook of Superconductivity*, 1st ed. (Academic Press, San Diego, 2000).
- [61] Wikipedia, “Yttrium barium copper oxide — wikipedia, the free encyclopedia,” http://en.wikipedia.org/w/index.php?title=Yttrium_barium_copper_oxide&oldid=656376770 (2015), [Online; accessed 21-May-2015].
- [62] S. Martin, A. T. Fiory, R. M. Fleming, L. F. Schneemeyer, and J. V. Waszczak, Phys. Rev. B **41**, 846–849 (1990).
- [63] T. Chien, Z. Wang, and N. Ong, Physical Review Letters **67**, 2088–2091 (1991).
- [64] C. M. Varma, P. B. Littlewood, S. Schmitt-Rink, E. Abrahams, and A. E. Ruckenstein, Phys. Rev. Lett. **63**, 1996–1999 (1989).

- [65] T. Valla, A. V. Fedorov, P. D. Johnson, Q. Li, G. D. Gu, and N. Koshizuka, *Phys. Rev. Lett.* **85**, 828–831 (2000).
- [66] V. J. Emery and S. A. Kivelson, *Nature* **374**, 434 (1995).
- [67] P. A. Lee, N. Nagaosa, and X.-G. Wen, *Rev. Mod. Phys.* **78**, 17 (2006).
- [68] Y. Sidis and P. Bourges, *J. Phys.: Conf. Ser.* **449**, 012012 (2013).
- [69] J. Xia, E. Schemm, G. Deutscher, S. A. Kivelson, D. A. Bonn, W. N. Hardy, R. Liang, W. Siemons, G. Koster, M. M. Fejer, and A. Kapitulnik, *Phys. Rev. Lett.* **100**, 127002 (2008).
- [70] R.-H. He, M. Hashimoto, H. Karapetyan, J. D. Koralek, J. P. Hinton, J. P. Testaud, V. Nathan, Y. Yoshida, H. Yao, K. Tanaka, W. Meevasana, R. G. Moore, D. H. Lu, S.-K. Mo, M. Ishikado, H. Eisaki, Z. Hussain, T. P. Devereaux, S. A. Kivelson, J. Orenstein, A. Kapitulnik, and Z.-X. Shen, *Science* **331**, 1579 (2011),
<http://www.sciencemag.org/content/331/6024/1579.full.pdf> .
- [71] C. M. Varma, *Phys. Rev. B* **55**, 14554 (1997).
- [72] S. Chakravarty, R. B. Laughlin, D. K. Morr, and C. Nayak, *Phys. Rev. B* **63**, 094503 (2001).
- [73] G. Ghiringhelli, M. Le Tacon, M. Minola, S. Blanco-Canosa, C. Mazzoli, N. B. Brookes, G. M. De Luca, A. Frano, D. G. Hawthorn, F. He, T. Loew, M. M. Sala, D. C. Peets, M. Salluzzo, E. Schierle, R. Sutarto, G. A. Sawatzky, E. Weschke, B. Keimer, and L. Braicovich, *Science* **337**, 821 (2012),
<http://www.sciencemag.org/content/337/6096/821.abstract> .
- [74] R. Comin, A. Frano, M. M. Yee, Y. Yoshida, H. Eisaki, E. Schierle, E. Weschke, R. Sutarto, F. He, A. Soumyanarayanan, Y. He, M. Le Tacon, I. S. Elfimov, J. E. Hoffman, G. A. Sawatzky, B. Keimer, and A. Damascelli, *Science* **343**, 390 (2014),
<http://www.sciencemag.org/content/343/6169/390.full.pdf> .
- [75] E. H. da Silva Neto, P. Aynajian, A. Frano, R. Comin, E. Schierle, E. Weschke, A. Gyenis, J. Wen, J. Schneeloch, Z. Xu, S. Ono, G. Gu, M. Le Tacon, and A. Yazdani, *Science* **343**, 393 (2014),
<http://www.sciencemag.org/content/343/6169/393.full.pdf> .
- [76] T. Wu, H. Mayaffre, S. Krämer, M. Horvatić, C. Berthier, W. N. Hardy, R. Liang, D. A. Bonn, and M.-H. Julien, (2014), arXiv:1404.1617v1 [cond-mat.supr-con] .

- [77] L. Li, Y. Wang, S. Komiya, S. Ono, Y. Ando, G. D. Gu, and N. P. Ong, Phys. Rev. B **81**, 054510 (2010).
- [78] F. Yu, M. Hirschberger, T. Lowe, G. Li, B. J. Lawson, T. Asaba, J. B. Kemper, T. Liang, J. Porras, G. S. Boebinger, J. Singleton, B. Keimer, L. Li, and N. P. Ong, (2014), arXiv:1402.7371v1 [cond-mat.supr-con] .
- [79] A. Damascelli, Z. Hussain, and Z.-X. Shen, Rev. Mod. Phys. **75**, 473–541 (2003).
- [80] A. Damascelli, Phys. Scr. **2004**, 61 (2004).
- [81] J. Braun, Rep. Prog. Phys. **59**, 1267–1338 (1996).
- [82] S. Hüfner, *Photoelectron Spectroscopy: Principles and Applications*, 3rd ed. (Springer, 2003).
- [83] V. L. Ginzburg and L. D. Landau, Zh. Eksp. Teor. Fiz. **20**, 1064 (1950), [L. D. Landau, Collected papers (Oxford: Pergamon Press, 1965) p. 546].
- [84] L. P. Gor’kov, Zh. Eksp. Teor. Fiz. **36**, 1918 (1959), [Sov. Phys. JETP **9**, 1364 (1959)].
- [85] L. D. Landau, Zh. Eksp. Teor. Fiz. **7**, 19 (1937), [Ukr. J. Phys. **53**, 25-35 (2008)].
- [86] L. D. Landau and E. M. Lifshitz, *Statistical Physics, Part 1*, 3rd ed., Course of Theoretical Physics, Vol. 5 (Butterworth-Heinemann, Oxford, Boston, Johannesburg, Melbourne, New Delhi, Singapore, 1980).
- [87] A. A. Abrikosov, Zh. Eksp. Teor. Fiz. **32**, 1442 (1957), [Sov. Phys. JETP **5**, 1174 (1957)].
- [88] A. C. Rose-Innes and E. H. Rhoderick, *Introduction to Superconductivity*, 2nd ed., edited by R. Smoluchowski and N. Kurti, International Series in Solid State Physics, Vol. 6 (Permagon Press, 1988).
- [89] D. Saint-James and P. G. de Gennes, Phys. Lett. **7**, 306 (1963).
- [90] C.-K. Lu and S. Yip, Phys. Rev. B **77**, 054515 (2008).
- [91] C.-K. Lu and S. Yip, J. Low. Temp. Phys. **155**, 160 (2009).
- [92] V. P. Mineev and K. V. Samokhin, Zh. Eksp. Teor. Fiz. **105**, 747 (1994), [JETP **78**, 401 (1994)].

- [93] V. M. Edelstein, J. Phys.: Condens. Matter **8**, 339 (1996).
- [94] V. P. Mineev and K. V. Samokhin, Phys. Rev. B **78**, 144503 (2008).
- [95] O. V. Dimitrova and M. V. Feigel'man, Pis'ma Zh. Eksp. Teor. Fiz. **78**, 1132 (2003).
- [96] D. F. Agterberg and R. P. Kaur, Phys. Rev. B **75**, 064511 (2007).
- [97] J. D. Jackson, *Classical Electrodynamics*, 3rd ed. (Wiley India (P) Ltd., New Delhi, 2007).
- [98] W. H. Press, B. P. Flannery, S. A. Teukolsky, and W. T. Vetterling, *Numerical Recipes: The Art of Scientific Computing (FORTRAN Version)* (Cambridge University Press, New York, 1989).
- [99] I. A. Luk'yanchuk and M. E. Zhitomirsky, Supercond. Rev. **1**, 207 (1995).
- [100] D. F. Agterberg, Phys. Rev. B **58**, 14 484 (1998).
- [101] C. P. Bean, Phys. Rev. Lett. **8**, 250 (1962).
- [102] P. A. Lee, Phys. Rev. X **4**, 031017 (2014).
- [103] P. Fulde and R. A. Ferrell, Phys. Rev. **135**, A550 (1964).
- [104] A. I. Larkin and Y. N. Ovchinnikov, Zh. Eksp. Teor. Fiz. **47**, 1136 (1964).
- [105] E. Berg, E. Fradkin, S. A. Kivelson, and J. M. Tranquada, New J. Phys. **11**, 115004 (2009).
- [106] D. F. Agterberg and H. Tsunetsugu, Nat. Phys. **4**, 639 (2008).
- [107] P. Corboz, T. M. Rice, and M. Troyer, Phys. Rev. Lett. **113**, 046402 (2014), arXiv:1402.2859v2 [cond-mat.str-el] .
- [108] M. Zelli, C. Kallin, and A. J. Berlinsky, Phys. Rev. B **84**, 174525 (2011).
- [109] J. Orenstein, Phys. Rev. Lett. **107**, 067002 (2011).
- [110] M. E. Simon and C. M. Varma, Phys. Rev. Lett. **89**, 247003 (2002).
- [111] R. M. Fernandes, A. V. Chubukov, J. Knolle, I. Eremin, and J. Schmalian, Phys. Rev. B **85**, 024534 (2012).

-
- [112] Y. Wang and A. Chubukov, *Phys. Rev. B* **90**, 035149 (2014).
- [113] V. M. Yakovenko, *Physica B: Condensed Matter* **460**, 159–164 (2015).
- [114] E. Fradkin, S. A. Kivelson, and J. M. Tranquada, (2014), arXiv:1407.4480v2 [cond-mat.supr-con] .
- [115] E. Berg, E. Fradkin, and S. A. Kivelson, *Nat. Phys.* **5**, 830 (2009).
- [116] L. Radzihovsky and A. Vishwanath, *Phys. Rev. Lett.* **103**, 010404 (2009).
- [117] V. Aji, Y. He, and C. M. Varma, *Phys. Rev. B* **87**, 174518 (2013).
- [118] H. Karapetyan, J. Xia, M. Hücker, G. D. Gu, J. M. Tranquada, M. M. Fejer, and A. Kapitulnik, *Phys. Rev. Lett.* **112**, 047003 (2014).
- [119] A. Shekhter, B. J. Ramshaw, R. Liang, W. N. Hardy, D. A. Bonn, F. F. Balakirev, R. D. McDonald, J. B. Betts, S. C. Riggs, and A. Migliori, *Nature* **498**, 75 (2013).
- [120] L. Mangin-Thro, Y. Sidis, A. Wildes, and P. Bourges, (2015), arXiv:1501.04919 [cond-mat.supr-con] .

Appendix A

Modified Bessel functions

A.1 Some properties of Modified Bessel functions

$$\left(\frac{1}{z} \frac{d}{dz}\right)^k \{z^\nu \mathcal{L}_\nu(z)\} = z^{\nu-k} \mathcal{L}_{\nu-k}, \quad \mathcal{L}_\nu = \begin{cases} I_\nu \\ e^{i\pi\nu} K_\nu \end{cases} \quad (\text{A.1})$$

where I_ν and K_ν are modified Bessel functions. This leads to the identities

$$K_0(x) = -\frac{K_1(x)}{x} - K_1'(x) \quad (\text{A.2})$$

$$I_0(x) = \frac{I_1(x)}{x} + I_1'(x) \quad (\text{A.3})$$

Also,

$$K_0'(x) = -K_1(x) \quad \text{and} \quad I_0'(x)I_1(x) \quad (\text{A.4})$$

Another useful identity is

$$I_\nu(x)K_\nu'(x) - I_\nu'(x)K_\nu = -\frac{1}{x} \quad (\text{A.5})$$

A.1.1 Limiting forms for small arguments

In the limit $z \rightarrow 0$

$$K_0(z) \sim -\ln(z) \quad (\text{A.6})$$

$$K_\nu(z) \sim \frac{1}{2}\Gamma(\nu)\left(\frac{1}{2}z\right)^{-\nu}, \quad (\Re \nu > 0) \quad (\text{A.7})$$

$$I_\nu(z) \sim \left(\frac{1}{2}z\right)^\nu / \Gamma(\nu + 1), \quad (\nu \neq -1, -2, \dots) \quad (\text{A.8})$$

A.1.2 Asymptotic expansions

Defining $\mu = 4\nu^2$, in the limit $|z| \rightarrow \infty$, the asymptotic expansions are

$$K_\nu(z) \sim \sqrt{\frac{\pi}{2z}} e^{-z} \left\{ 1 + \frac{(\mu - 1)}{8z} + \frac{(\mu - 1)(\mu - 9)}{2!(8z)^2} + \frac{(\mu - 1)(\mu - 9)(\mu - 25)}{3!(8z^3)} \right\},$$

(where $|\arg z| < \frac{3}{2}\pi$) (A.9)

$$I_\nu(z) \sim \frac{e^z}{\sqrt{2\pi z}} \left\{ 1 - \frac{(\mu - 1)}{8z} + \frac{(\mu - 1)(\mu - 9)}{2!(8z)^2} - \frac{(\mu - 1)(\mu - 9)(\mu - 25)}{3!(8z^3)} \right\},$$

(where $|\arg z| < \frac{1}{2}\pi$) (A.10)

Appendix B

Numerical codes

B.1 London limit solution

```

! The equation being solved is
! Az(x) = (MU/(KAPPA**2))(K0(x)*(int(0 to x) dt t*I0(t)*K0(t))
!           + I0(x)*(int(x to infnty) dt t*((K0(t))^2)) - K0/2)
! Output is Az, Bphi and Jz
MODULE KINDS

!       To determine the kinds of single and double precision real values on a
!       particular computer

IMPLICIT NONE

INTEGER, PARAMETER :: SHORT = SELECTED_INT_KIND(3), MEDIUM = SELE&
&   CTED_INT_KIND (9), LONG = SELECTED_INT_KIND(18)

INTEGER, PARAMETER :: SGL = KIND(0.0), DBL = KIND(0.0D0)

END MODULE KINDS

!*****
!*****

MODULE FILE_NOMEN

USE KINDS

IMPLICIT NONE

CONTAINS

SUBROUTINE FILE_NAME(String, MU, FILENAME1, FILENAME2)

```

```

CHARACTER(LEN = *) :: STRING
CHARACTER(LEN = 25) :: FILENAME1, FILENAME2
REAL(DBL) :: MU
IF(MU .LT. 10.0_DBL) THEN
WRITE(STRING, '(F5.3)') MU
ELSE IF (MU .LT. 100.0_DBL) THEN
WRITE(STRING, '(F6.3)') MU
END IF

FILENAME1 = 'lvec2mu'//TRIM(STRING)//'.dat'
FILENAME2 = 'ljzmu'//TRIM(STRING)//'.dat'
END SUBROUTINE FILE_NAME
END MODULE FILE_NOMEN

!*****
!*****

PROGRAM LONDONZ
USE KINDS
USE FILE_NOMEN
USE numerical_libraries !uses the ISML libraries
REAL(DBL) :: XLEFT, XRIGHT, H, X, Az, Bphi, Jz, KAPPA, MU, PI
REAL(DBL) :: KAPMIN, KAPMAX, KAPSTEP, MUMIN, MUMAX, MUSTEP
REAL(DBL) :: F1, F3, A, B, RES1, RES3, ERREST1, ERREST3
REAL(DBL) :: K0, I0, K1, I1, ERRABS, ERRREL
REAL(DBL) :: F2, F4, BOUND, RES2, RES4, ERREST2, ERREST4
INTEGER(MEDIUM) :: K, M
INTEGER(SHORT) :: L, N
CHARACTER(LEN = 19) :: STRING
CHARACTER(LEN = 25) :: FILENAME1, FILENAME2
INTEGER :: INTERV
EXTERNAL F1, F2, F3, F4
ERRABS = 0.0 !Set error tolerances
ERRREL = 0.001
WRITE(*, *) 'MODIFY MODULE FILE_NOMEN TO EDIT THE OUTPUT FILE NAMES'
WRITE (*, *) 'ENTER KAPPA MINIMUM'

```

```

READ (*, *) KAPMIN
WRITE (*, *) 'ENTER KAPPA MAXIMUM'
READ (*, *) KAPMAX
WRITE (*, *) 'ENTER KAPPA STEP (NON ZERO POSITIVE #)'
READ (*, *) KAPSTEP
WRITE (*, *) 'ENTER MINIMUM COUPLING PARAMETER'
READ (*, *) MUMIN
WRITE (*, *) 'ENTER MAXIMUM COUPLING PARAMETER'
READ (*, *) MUMAX
WRITE (*, *) 'ENTER MU STEP (NON ZERO POSITIVE #)'
READ (*, *) MUSTEP
PI = 3.141592653589793238
XLEFT = 0.0_DBL
XRIGHT = 40.0_DBL
H = 0.0001
M = 168651
L = NINT((MUMAX - MUMIN)/MUSTEP) + 1
WRITE(*, *) '# OF MU VALUES BEING SOLVED FOR IS', L
N = NINT((KAPMAX - KAPMIN)/KAPSTEP) + 1
WRITE(*, *) '# OF KAPPA VALUES BEING SOLVED FOR IS', N
OPEN(UNIT = 3, FILE = 'lmu_filename.dat', STATUS = 'REPLACE')
WRITE (3, *) "# The first column contains mu value, second ",&
& " column contains the name of the corresponding result file and"
WRITE (3, *) "# third column contains the name of the ",&
& "corresponding result file for current Jz."
MU = MUMIN
DO I = 1, L
    CALL FILE_NAME(STRING, MU, FILENAME1, FILENAME2)
    WRITE(3, *) MU, " ", TRIM(FILENAME1), " ", TRIM(FILENAME2)
    OPEN(UNIT = 1, FILE = TRIM(FILENAME1), STATUS = 'REPLACE')
    OPEN(UNIT = 2, FILE = TRIM(FILENAME2), STATUS = 'REPLACE')
    WRITE (1, *) "# Coupling parameter mu =", MU
    WRITE (1, *) "#

```

```

WRITE (1, *) "# First column is spatial coordinate, second ",&
& "# column contains vector potential(Az),"
WRITE (1, *) "#third column contains magnetic flux (Bphi)."
WRITE (1, *) "#                                     "
WRITE (2, *) "# Coupling parameter mu =", MU
WRITE (2, *) "#                                     "
WRITE (2, *) "# First column is spatial coordinate, second ",&
& "column contains Current(Jz)."
WRITE (2, *) "#                                     "
N = 0
KAPPA = KAPMIN
DO
    IF(KAPPA .GT. KAPMAX) EXIT
    N = N + 1
    WRITE (1, *) "# G-L PARAMETER KAPPA =", KAPPA
    WRITE (2, *) "# G-L PARAMETER KAPPA =", KAPPA
    DO K = 1, M-1
        X = XLEFT + (K)*H
! X = 0 is excluded for K0 is divergent there
        K0 = DBSKO(X)
        I0 = DBSIO(X)
        K1 = DBSK1(X)
        I1 = DBSI1(X)
        A= 0.0_DBL
        B = X
        BOUND = X
        INTERV = 1
    CALL DQDAGS (F1, A, B, ERRABS, ERRREL, RES1, ERREST1)
    CALL DQDAGI (F2, BOUND, INTERV, ERRABS, ERRREL, RES2, ERREST2)
    CALL DQDAGS (F3, A, B, ERRABS, ERRREL, RES3, ERREST3)
    CALL DQDAGI (F4, BOUND, INTERV, ERRABS, ERRREL, RES4, ERREST4)
        Az = K0*RES1 + I0*RES2 - K0/2
        Bphi = K1*RES3 + I1*RES4 - K1/2

```

```

Jz = K0 - K0*RES1 - I0*RES2

Az = (MU/(KAPPA**2)) * Az
Bphi = (MU/(KAPPA**2)) * Bphi
Jz = (MU/(4.0_DBL*PI*(KAPPA**2))) * Jz
Jz = 10**6 * Jz

! Multiplied with 10^6 to obtain proper scaling for plotting.
WRITE (1, *) X, Az, Bphi
WRITE (2, *) X, Jz

END DO
WRITE (1, *) "#*****", &
& "*****"
WRITE (1, *) " " "
WRITE (1, *) " " "
WRITE (2, *) "#*****", &
& "*****"
WRITE (2, *) " " "
WRITE (2, *) " " "
KAPPA = KAPPA + KAPSTEP

END DO
WRITE(*, *) '# of Kappa values solved for is ', N
CLOSE(UNIT = 1); CLOSE(UNIT = 2)
MU = MU + MUSTEP

END DO
END PROGRAM LONDONZ

! *****
! *****

FUNCTION F1 (t)
USE KINDS
REAL(DBL) :: t, I0, K0
EXTERNAL DBSIO, DBSKO
I0 = DBSIO (t)
K0 = DBSKO (t)

```



```
F1 = t*I0*K0
RETURN
END
! *****
! *****
FUNCTION F2 (t)
USE KINDS
REAL(DBL) :: t, K0
EXTERNAL DBSK0
K0 = DBSK0 (t)
F2 = t*K0*K0
RETURN
END
! *****
! *****
FUNCTION F3 (t)
USE KINDS
REAL(DBL) :: t, I1, K1
EXTERNAL DBSI1, DBSK1
I1 = DBSI1 (t)
K1 = DBSK1 (t)
F3 = t * I1 * K1
RETURN
END
! *****
! *****
FUNCTION F4 (t)
USE KINDS
REAL(DBL) :: t, K1
EXTERNAL DBSK1
K1 = DBSK1 (t)
F4 = t * K1 * K1
RETURN
```

END

B.2 Full solution

The code included here generates numerical solution for Eq. (3.12). This same code can be appropriately modified to solve Eqs. (3.13) and (3.11).

```

MODULE KINDS
! To determine the kinds of single and double precision real
! values on a particular computer.
IMPLICIT NONE
INTEGER, PARAMETER :: SHORT = SELECTED_INT_KIND(3), MEDIUM = SELEC&
&TED_INT_KIND(9), LONG = SELECTED_INT_KIND(18)
INTEGER, PARAMETER :: SGL = KIND(0.0), DBL = KIND(0.0D0)
END MODULE KINDS

!*****
!*****

MODULE PARAMETER
USE KINDS
IMPLICIT NONE
! Global Parameters
INTEGER(SHORT), PARAMETER :: NE = 2, NB = 1
! NE is number of first order equations and NB is number of boundary conditions
! at first boundary
INTEGER(LONG), PARAMETER :: M = 400001
! M is no. of grid points (including first and last boundary)
INTEGER(KIND = SHORT), PARAMETER :: NSI = NE, NSJ = 2*NE + 1
INTEGER(KIND = SHORT), PARAMETER :: NCI = NE, NCJ = NE - NB + 1
INTEGER(KIND = LONG), PARAMETER :: NCK = M + 1
INTEGER(LONG), PARAMETER :: ITMAX = 1000
REAL(DBL), PARAMETER :: CONV = 1.0E-16

```

```

REAL(DBL), PARAMETER :: XLEFT = 0.0_DBL, XRIGHT = 40.0_DBL,&
& H = 0.0001

! XLEFT and XRIGHT: initial and final mesh points respectively. H is mesh size.
! If XRIGHT or H is changed M must be adjusted. M = NINT((XRIGHT - XLEFT)/H)+1
REAL(KIND = DBL), DIMENSION(M) :: X ! Matrix X stores mesh points
REAL(KIND = DBL), DIMENSION(NE, M):: Y
! Matrix Y stores the intial guess and then the calculated corrections are
! added to stored values after each iteration.
REAL(KIND = DBL), DIMENSION(NSI, NSJ):: S
REAL(KIND = DBL), DIMENSION(NCI, NCJ, NCK):: C
END MODULE PARAMETER

!*****
!*****

MODULE STEPS

! This module include the subroutines used to solve the Matrix equation.
! This module is completely independent of the equations being solved.

USE KINDS
USE PARAMETER
IMPLICIT NONE
CONTAINS
SUBROUTINE PINVS(K)
! PINVS Diagonalize the required section of the S matrix at given mesh point to
! unit matrix. K keeps the count of mesh points
INTEGER(SHORT) :: ID, I, J, JP, IPIV, JPIV, IROW, L
INTEGER(SHORT), DIMENSION(NE) :: INDXR
INTEGER(SHORT) :: IINIT, IFIN, JINIT, JFIN, ICOFF, JCOFF, JS1
INTEGER(LONG) :: K
REAL(DBL) :: BIG, PIV, PIVINV, DUM
REAL(DBL), DIMENSION(NE) :: PSCL
IINIT = 1
IFIN = NE
JFIN = NE + NB
ICOFF = -NB

```

```
JCOFF = -NE - NB
IF (K == 1) THEN
    IINIT = NE - NB + 1
    JINIT = NE + 1
ELSE
    IF(K == M + 1) THEN
        IFIN = NE - NB
        JINIT = NE + NB + 1
        JFIN = 2*NE
        ICOFF = -NE - NB
    ELSE
        JINIT = NB + 1
    END IF
END IF
DO I = IINIT, IFIN
    BIG = 0.0_DBL
    DO J = JINIT, JFIN
        IF(ABS(S(I, J)) > BIG) THEN
            BIG = ABS(S(I, J))
        END IF
    END DO
    IF(BIG == 0.0_DBL)THEN
        STOP
    END IF
    PSCL(I) = BIG
    INDXR(I) = 0
END DO
BIG = 0.0_DBL
L = 0
DO ID = IINIT, IFIN
    PIV = 0.0_DBL
    DO I = IINIT, IFIN
        IF(INDXR(I) == 0)THEN
```

```
      IF(L == 0) THEN
        DO J = JINIT, JFIN
          IF(ABS(S(I, J)) .GT. BIG) THEN
            BIG = ABS(S(I, J))
            JPIV = J
            IPIV = I
          END IF
        END DO
      ELSE
        BIG = 0.0_DBL
        DO J = JINIT, JFIN
          IF(ABS(S(I, J)) > BIG) THEN
            BIG = ABS(S(I, J))
            JP = J
          END IF
        END DO
        IF(BIG/PSCL(I) > PIV) THEN
          IPIV = I
          JPIV = JP
          PIV = BIG/PSCL(I)
        END IF
      END IF
    ENDIF
  END DO
  IF(S(IPIV, JPIV) == 0.0_DBL) THEN
    WRITE(*, *) '## SINGULAR MATRIX'
    STOP
  ENDIF
  INDXR(IPIV) = JPIV
  PIVINV = 1.0_DBL / S(IPIV, JPIV)
  DO J = JINIT, NSJ
    S(IPIV, J) = S(IPIV, J)*PIVINV
  END DO
```

```

      S(IPIV, JPIV) = 1.0_DBL
      DO I = IINIT, IFIN
        IF(I /= IPIV) THEN
          IF(S(I, JPIV) /= 0.0_DBL) THEN
            DUM = S(I, JPIV)
            DO J = JINIT, NSJ
              S(I, J) = S(I, J) - DUM      &
&                                         *S(IPIV, J)
            END DO
            S(I, JPIV) = 0.0_DBL
          END IF
        END IF
      END DO

      L = L + 1
      END DO

      JS1 = JFIN + 1
      DO I = IINIT, IFIN
        IROW = INDXR(I) + ICOFF
        DO J = JS1, NSJ
          C(IROW, J + JCOFF, K) = S(I, J)
        END DO
      END DO

      ! The modified S matrix is stored in C matrix for each mesh point labeled by K.
      END DO

      END SUBROUTINE PINVS

      !*****
      !*****
      SUBROUTINE RED(K)  ! This reduces the first NB coulumns of a S Matrix to zero.
      INTEGER(SHORT) :: I, J, L, IC
      INTEGER(SHORT) :: IFIN, JINIT, JFIN, LINIT, LFIN
      INTEGER(LONG)  :: K
      REAL(DBL)     :: VX

      IFIN = NE
      JINIT = 1

```

```

JFIN = NB
LINIT = NB + 1
LFIN = NE
IC = NCJ
IF (K == 1) RETURN          ! At first mesh point no reduction is required.
IF (K == M + 1) THEN
    IFIN = NE - NB
    JINIT = NE + 1
    JFIN = NE + NB
    LINIT = NE + NB + 1
    LFIN = 2*NE
END IF
DO J = JINIT, JFIN
    DO L = LINIT, LFIN
        VX = C (IC, L - JFIN, K - 1)
        DO I = 1, IFIN
            S(I, L) = S(I, L) - S(I, J)*VX
        END DO
    END DO
    VX = C(IC, NCJ, K - 1)
    DO I = 1, IFIN
        S(I, NSJ) = S(I, NSJ) - S(I, J)*VX
    END DO
    IC = IC + 1
END DO
END SUBROUTINE RED
!*****
!*****
SUBROUTINE BKSUB()
! This subroutine involves Back Substitution . This is used only once for an
! iteration. It operates on the C matrix.
INTEGER(SHORT) :: I, J, IC1
INTEGER(LONG) :: K

```

```

REAL(DBL) :: XX
IC1 = 1
DO K = M, 1, -1
    IF(K == 1) IC1 = NCJ
    DO J = 1, NE - NB
        XX = C(J, NCJ, K + 1)
        DO I = IC1, NE
            C(I, NCJ, K) = C(I, NCJ, K) - C(I, J, K)*XX
        END DO
    END DO
END DO

! REORDER CORRECTION IN COULUMN 1
DO K = 1, M
    DO I = 1, NB
        C(I, 1, K) = C (I + NE - NB, NCJ, K)
    END DO
    DO I = 1, NE - NB
        C(I + NB, 1, K) = C(I, NCJ, K + 1)
    ! WRITE(*, *) K, ',', I+NB, ',', C(I + NB, 1, K)
    END DO
END DO

END SUBROUTINE BKSUB
END MODULE STEPS

!*****
!*****

MODULE EQUATIONS
USE KINDS
USE PARAMETER
IMPLICIT NONE
CONTAINS
SUBROUTINE DIFEQ(K, KAPPA)
! This subroutine is used to enter S matrix (boundary conditions and Jacobian

```


! matrix). It calculates the elements of S matrix at each mesh point.

```
REAL(KIND = DBL) :: KAPPA
```

```
INTEGER(LONG) :: K
```

```
IF(K == 1) THEN
```

```
    S(2, 3) = 1.0_DBL
```

```
    S(2, 4) = 0.0_DBL
```

```
    S(2, NSJ) = Y(1, 1)
```

```
ELSE IF(K == M + 1) THEN
```

```
    S(1, 3) = 1.0_DBL
```

```
    S(1, 4) = 0.0_DBL
```

```
    S(1, NSJ) = Y(1, M) - 1.0_DBL
```

```
ELSE
```

```
    S(1,1) = -1.0_DBL
```

```
        S(1,2) = -0.5_DBL * (X(K) - X(K - 1))
```

```
    S(1,3) = 1.0_DBL
```

```
        S(1,4) = -0.5_DBL * (X(K) - X(K - 1))
```

```
    S(2, 1) = (X(K) - X(K - 1)) * (-3.0_DBL/8.0_DBL) * (KAPPA**2) * &
```

```
& ((Y(1, K) + Y(1, K - 1))**2) + 0.5_DBL * (KAPPA**2) &
```

```
& - (2.0_DBL/((X(K) + X(K - 1))**2))
```

```
        S(2, 2) = -1.0_DBL + (X(K) - X(K - 1))/(X(K) + X(K - 1))
```

```
    S(2, 3) = S(2, 1)
```

```
    S(2, 4) = 1.0_DBL + (X(K) - X(K - 1))/(X(K) + X(K - 1))
```

```
S(1, NSJ) = Y(1, K) - Y(1, K-1) - 0.5_DBL*(X(K) - &
```

```
& X(K - 1))*(Y(2, K) + Y(2, K-1))
```

```
        S(2, NSJ) = Y(2, K) - Y(2, K-1) - (X(K) - X(K - 1)) * &
```

```
& (-((Y(2, K) + Y(2, K - 1))/(X(K) + X(K - 1))) + &
```

```
& ((2.0_DBL*(Y(1, K) + Y(1, K - 1))/(X(K) + X(K - 1))**2)) - &
```

```
& 0.5_DBL*(KAPPA**2)*(Y(1, K) + Y(1, K - 1)) * &
```

```
& (1.0_DBL - 0.25_DBL * ((Y(1, K) + Y(1, K - 1))**2))
```

```
END IF
```

```
END SUBROUTINE DIFEQ
```

```
END MODULE EQUATIONS
```

```
!*****
```

```

!*****
MODULE SOLVE
USE KINDS
USE PARAMETER
USE STEPS
USE EQUATIONS
IMPLICIT NONE
INTEGER(LONG) :: IT, JV, KM
REAL(DBL) :: SLOWC, ERROR, ERRJ, FAC, VMAX, VZ, NVAR
REAL(DBL), DIMENSION(NE) :: ERMAX, KMAX, SCALV
PRIVATE :: IT, JV, KM, SLOWC, ERROR, ERRJ, FAC, VMAX, VZ, NVAR,&
&          ERMAX, KMAX
CONTAINS
SUBROUTINE SOLVDE(KAPPA)
REAL(KIND = DBL) :: KAPPA
INTEGER(LONG) :: K, J          ! K defined here is local to this subroutine.
SLOWC = 1.0_DBL
NVAR = NE*M
DO IT = 1, ITMAX
!      WRITE(*, *) IT
      DO K = 1, M + 1
          CALL DIFEQ(K, KAPPA)
          CALL RED (K)
          CALL PINVS(K)
      END DO
      CALL BKSUB()          ! BKSUB is called only once during an iteration.
      ERROR = 0.0_DBL
      DO J = 1, NE
! Variables in this Do loop to be adjusted according to the problem
! being solved.
          JV = J
          ERRJ = 0.0_DBL
          KM = 0

```

```

      VMAX = 0.0_DBL
      DO K = 1, M
          VZ = ABS(C(JV, 1, K))
          IF (VZ .GT. VMAX) THEN
              VMAX = VZ
!VMAX is the maximum absolute value of the calculated corrections
              KM = K
! KM is the mesh point where VMAX is found.
          END IF
          ERRJ = ERRJ + VZ
      END DO
      ERROR = ERROR + ERRJ/SCALV(J)
! Absolute value of each correction is scaled and all of them are added
! together.
      ERMAX(J) = C(JV, 1, KM)/SCALV(J)
      KMAX(J) = KM
  END DO
  ERROR = ERROR/NVARS          ! Average correction is calculated.
  FAC = SLOWC/(MAX(SLOWC, ERROR))
! FAC is the fraction which is multiplied to the corrections before adding to
! previous values of order parameter and its derivative.
  DO J = 1, NE
      JV = J
      DO K = 1, M
          Y(J, K) = Y(J, K) - FAC * C(JV, 1, K)
! The corrections are being subtracted because the Right hand side of the
! matrix equation or the last column of each S matrix must have had an explicit
! -ve sign.
      END DO
  END DO
  WRITE(*, *) IT, ERROR, FAC
! This is what printed in the terminal. The result for order parameter is
! directed to a file.

```

```

!           IF (IT == 1) THEN
!
!               DO K = 1, M
!
!                   WRITE(*, *) K, ' ', C(2, 1, K), ' ', Y(2, K)
!
!               END DO
!
!           END IF
!
!           IF (ERROR .LT. CONV) RETURN
!
!       END DO
!
!       WRITE(*, *) 'ITMAX EXCEEDED IN SOLVDE for KAPPA =', KAPPA ! CONVERGENCE FAILED
!
!   END SUBROUTINE SOLVDE
!
! END MODULE SOLVE
!
!*****
!*****
PROGRAM SINGLE_VORTEX_f
USE KINDS
USE PARAMETER
USE STEPS
USE SOLVE
USE EQUATIONS
IMPLICIT NONE
INTEGER(LONG) :: K, KK, N
REAL(KIND = DBL) :: KAPMIN, KAPMAX, KAPSTEP, KAPPA !KAPPA IS G-L PARMETER
OPEN(UNIT = 1, FILE = 'init.dat', STATUS = 'REPLACE', ACTION = &
&      'WRITE') ! initial guess is written to this file
OPEN(UNIT = 2, FILE = 'order.dat', STATUS = 'REPLACE', ACTION = &
&      'WRITE') ! result is written in this file
OPEN(UNIT = 3, FILE = 'f.dat', STATUS = 'REPLACE', ACTION = &
&      'WRITE')
OPEN(UNIT = 4, FILE = 'dfdx.dat', STATUS = 'REPLACE', ACTION = &
&      'WRITE')
WRITE(*, *) 'Enter KAPPA MINIMUM'
READ(*, *) KAPMIN
WRITE(*, *) 'Enter KAPPA MAXIMUM'
READ(*, *) KAPMAX

```

```

WRITE(*, *) 'Enter KAPPA STEP (NON ZERO POSITIVE #)'
READ(*, *) KAPSTEP
! KAPMIN = 8.0_DBL
! KAPMAX = 16.0_DBL
! KAPSTEP = 2.0_DBL
KAPPA = KAPMIN
! INITIAL GUESS
DO K = 1, M
! In this Do loop mesh points are designated.
      X(K) = XLEFT + (K - 1)*H
      Y(1, K) = TANH(KAPPA*X(K))          ! initial Guess for order parameter
      Y(2, K) = KAPPA*(1 - (Y(1, K))**2)
! initial guess for the derivative of order parameter
      WRITE(1, *) X(K), Y(1, K), Y(2, K)
END DO
! SCALING
SCALV(1) = 1.0_DBL
SCALV(2) = MAX(1.0_DBL, Y(2, M))
! This scaling is defined w.r.t. the derivative Y(2, M).

N = 0
WRITE(2, *)"# The first column is spatial coordinate, second ", &
&          "column contains order parameter and"
WRITE(2, *)"# third column contains the spatial derivative of ",&
&          "order parameter."
DO
      IF (KAPPA .GT. KAPMAX) EXIT
      CALL SOLVDE (KAPPA)
      N = N + 1
      WRITE(2, *) "# G-L PARAMETER KAPPA =", KAPPA
      DO K = 1, M
            WRITE(2, *) X(K), Y(1, K), Y(2, K)
            WRITE(3, *) Y(1, K)

```

```
        WRITE(4, *) Y(2, K)
    END DO
    WRITE(2, *) "#*****", &
&          "*****"
    WRITE(2, *) " "
    WRITE(2, *) " "
    WRITE(3, *) " "
    WRITE(3, *) " "
    WRITE(4, *) " "
    WRITE(4, *) " "
    KAPPA = KAPPA + KAPSTEP
END DO
WRITE(*, *) "NUMBER OF KAPPA VALUES SOLVED FOR IS ", N
END PROGRAM SINGLE_VORTEX_f
```

Appendix C

Tetragonal PDW pairing at high symmetry points

C.1 Tetragonal symmetry ($\delta K_y = 0$)

When $\delta \mathbf{K}_y = 0$ in Fig. 4.2, the momenta \mathbf{K}_i , about which PDW cooper pairs are formed, move to high symmetry points on the Brillouin zone boundary, as shown in Fig. C.1. The analysis for this configuration is the same as in Ref. [106]. The corresponding mean-field ground states are listed in Table C.1.

It is clear from Table C.1 that the only ground state that contains both CDW and loop current order is $(\Delta_{\mathbf{Q}_1}, \Delta_{\mathbf{Q}_2}, \Delta_{-\mathbf{Q}_1}, \Delta_{-\mathbf{Q}_2}) = (1, 1, 0, 0)$, which has four fold discrete degeneracy i.e $(1, 1, 0, 0) \equiv (0, 0, 1, 1) \equiv (1, 0, 0, 1) \equiv (0, 1, 1, 0)$. However, the charge order $\rho_{\mathbf{Q}_1-\mathbf{Q}_2}$ in this state is not at the observed wave vector, so it cannot be a pseudogap order parameter.

The ground state considered in Ref. [102] is $(\Delta_{\mathbf{Q}_1}, \Delta_{\mathbf{Q}_2}, \Delta_{-\mathbf{Q}_1}, \Delta_{-\mathbf{Q}_2}) = (1, 1, 1, 1)$. This state lacks loop current order and hence cannot account for observed signatures of translational invariant broken time-reversal symmetry even though it reproduces the ARPES spectra and accounts for the anomalous qp properties observed.

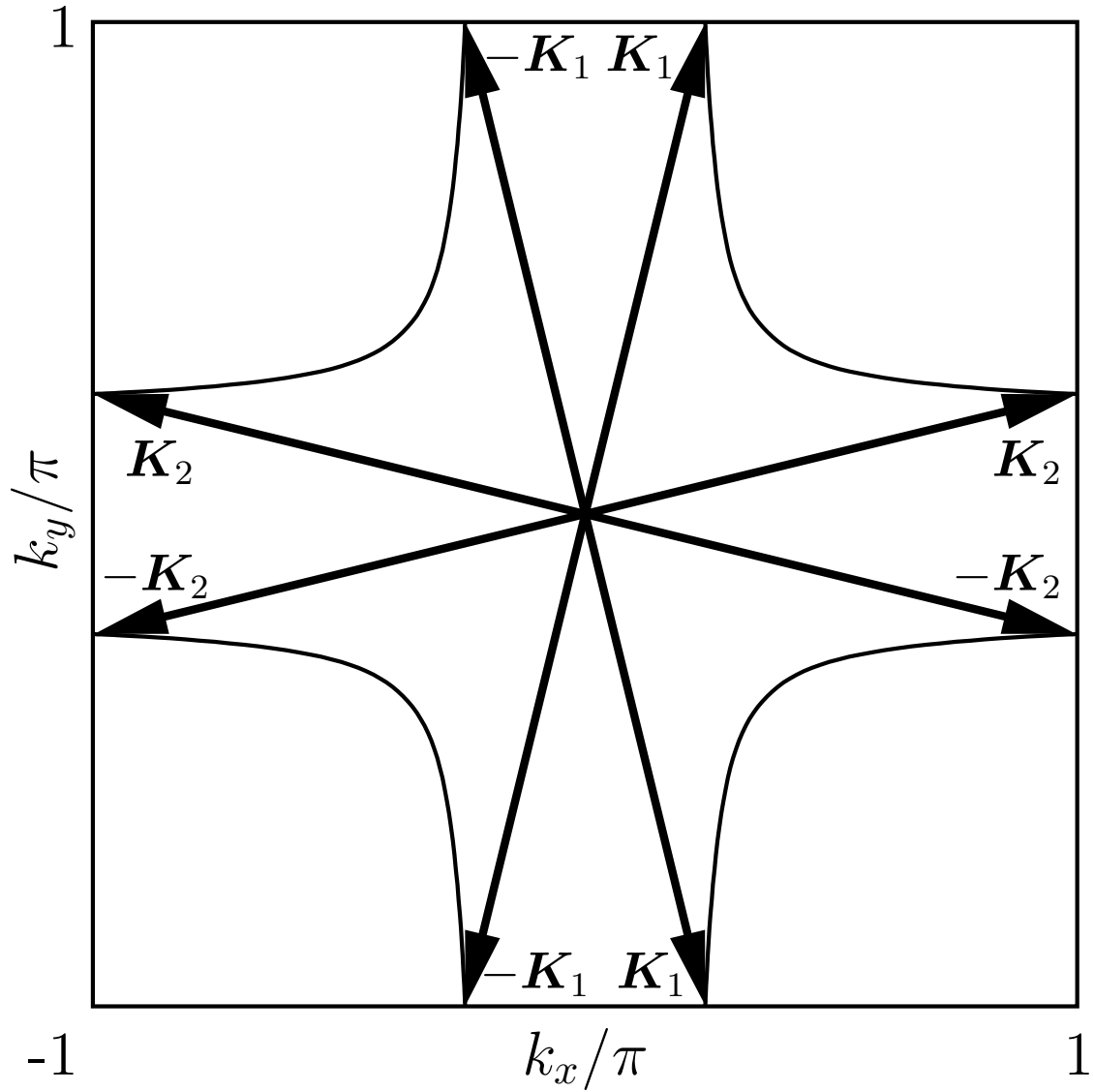


Figure C.1: The positions of the momenta K_i about which PDW Cooper pairs are formed. The corresponding four PDW order parameter components Δ_{Q_i} have momenta $Q_i = 2K_i$. Here $\delta K_y = 0$ see Fig 4.2. This reproduces the theory of Ref. [102].

Table C.1: Properties of PDW Ground States for tetragonal symmetry in Fig. C.1. All possible PDW ground states and accompanying CDW and ODW order. The second column shows the parameter regions for which these phases are stable. In the third and fourth columns: $2\mathbf{Q}_x = (2Q, 0)$, $2\mathbf{Q}_y = (0, 2Q)$, other modes can be found by using the relationships $\rho_{\mathbf{Q}} = (\rho_{-\mathbf{Q}})^*$ and $L_{\mathbf{Q}}^z = (L_{-\mathbf{Q}}^z)^*$. The fifth column gives all translational invariant order parameters with $l_x \propto |\Delta_{\mathbf{Q}_2}|^2 - |\Delta_{-\mathbf{Q}_2}|^2$, $l_y \propto |\Delta_{\mathbf{Q}_1}|^2 - |\Delta_{-\mathbf{Q}_1}|^2$, $\Delta_{4e,s} \propto \Delta_{\mathbf{Q}_1}\Delta_{-\mathbf{Q}_1} + \Delta_{\mathbf{Q}_2}\Delta_{-\mathbf{Q}_2}$, $\Delta_{4e,d} \propto \Delta_{\mathbf{Q}_1}\Delta_{-\mathbf{Q}_1} - \Delta_{\mathbf{Q}_2}\Delta_{-\mathbf{Q}_2}$, and $\epsilon_{xx} - \epsilon_{yy} \propto |\Delta_{\mathbf{Q}_2}|^2 + |\Delta_{-\mathbf{Q}_2}|^2 - |\Delta_{\mathbf{Q}_1}|^2 - |\Delta_{-\mathbf{Q}_1}|^2$. The sixth column gives the degeneracy of the ground state.

$(\Delta_{\mathbf{Q}_1}, \Delta_{\mathbf{Q}_2}, \Delta_{-\mathbf{Q}_1}, \Delta_{-\mathbf{Q}_2})$	Stability	CDW modes	ODW modes	Q=0 Order	Degeneracy Manifold
(1, 0, 0, 0)	$\beta_2 + \beta_3 < 0, \beta_3 < 0$	none	none	l_y	$U(1) \times Z_2 \times Z_2$
	$\beta_2 + 2\beta_3 < - \beta_5 /4$			$\epsilon_{xx} - \epsilon_{yy}$	
(1, 1, 0, 0)	$\beta_2 + \beta_3 > 0$	$\rho_{\mathbf{Q}_1 - \mathbf{Q}_2}$	$L_{\mathbf{Q}_1 - \mathbf{Q}_2}^z$	$l_x = l_y$	$U(1) \times U(1) \times Z_4$
	$\beta_3 < - \beta_5 /4$				
(1, 0, 1, 0)	$\beta_3 > 0$	$\rho_{2\mathbf{Q}_x}$	none	$\Delta_{4e,s}, \Delta_{4e,d}$	$U(1) \times U(1) \times Z_2$
	$\beta_2 < - \beta_5 /4$			$\epsilon_{xx} - \epsilon_{yy}$	
(1, 1, 1, 1)	$\beta_5 < 0, \beta_5 < 4\beta_2$	$\rho_{2\mathbf{Q}_x}, \rho_{2\mathbf{Q}_y}$ $\rho_{\mathbf{Q}_1 - \mathbf{Q}_2}, \rho_{\mathbf{Q}_1 + \mathbf{Q}_2}$	none	$\Delta_{4e,s}$	$U(1) \times U(1) \times U(1)$
	$\beta_5 < 4\beta_3$				
	$\beta_5/4 < \beta_2 + 2\beta_3$				
(1, i , 1, i)	$\beta_5 > 0, -\beta_5 < 4\beta_2$	$\rho_{2\mathbf{Q}_x}, \rho_{2\mathbf{Q}_y}$	$L_{\mathbf{Q}_1 - \mathbf{Q}_2}^z$ $L_{\mathbf{Q}_1 + \mathbf{Q}_2}^z$	$\Delta_{4e,d}$	$U(1) \times U(1) \times U(1)$
	$-\beta_5 < 4\beta_3$				
	$-\beta_5/4 < \beta_2 + 2\beta_3$				

CURRICULUM VITAE

Manoj K. Kashyap

Place of Birth: New Delhi, India

Education

BSc, Deen Dayal Upadhyaya College, University of Delhi, India, May 2000
Physics, Chemistry, Mathematics

MSc, Devi Ahilya Vishwavidyalaya, Indore, MP, India, June 2005
Major: Physics

Pre-Doctoral Diploma in Physics, Institute of Physics, India, June 2008

PhD in Physics, University of Wisconsin-Milwaukee, WI, USA, August 2015

Dissertation Title: Theoretical study of Magnetoelectric effects in Noncentrosymmetric and Cuprate Superconductors

Publications

Vortices in Noncentrosymmetric Superconductors. M. K. Kashyap, and D. F. Agterberg, *Phys. Rev. B*, **88**, 104515 (2013).

Emergent loop current order from pair density wave superconductivity. D. F. Agterberg, Drew S. Melchert, and M. K. Kashyap, *Phys. Rev. B*, **91**, 054502 (2015).